Winter 12-15-2018

Linking Structure and Dynamics in Metallic Liquids: A Combined Experimental and Molecular Dynamics Approach

Robert Ashcraft
Washington University in St. Louis

WASHINGTON UNIVERSITY IN ST. LOUIS
Department of Physics

Dissertation Examination Committee:
Kenneth F. Kelton, Chair
Rohan Mishra
Zohar Nussinov
James S. Schilling
Li Yang

Linking Structure and Dynamics in Metallic Liquids: A Combined Experimental and Molecular Dynamics Approach

by

Robert Alden Ashcraft

A dissertation presented to
The Graduate School
of Washington University in
partial fulfillment of the
requirements for the degree
of Doctor of Philosophy

December, 2018
St. Louis, Missouri

Contents

List of Figures

List of Tables

List of Abbreviations

ACF autocorrelation function.
ANL Argonne National Laboratory.
APS Advanced Photon Source.
ARCS Wide Angular-Range Chopper Spectrometer.
ARCS2015 Experiments performed on ARCS during 2015.
ARCS2016 Experiments performed on ARCS during 2016.
ARCS2017 Experiments performed on ARCS during 2017.
BESL Beamline Electrostatic Levitator.
BESL2007 X-ray scattering experiments performed during 2007.
BESL2010 X-ray scattering experiments performed during 2010.
BESL2013 X-ray scattering experiments performed during 2013.
BESL2016 X-ray scattering experiments performed during 2016.
CNCS Cold Neutron Chopper Spectrometer.
DGS direct-geometry spectrometer.
DPPCF Dynamic Partial Pair Correlation Function.
DTA Differential Thermal Analysis.
EAM Embedded Atom Method.
EML Electromagnetic Levitation.
ESL Electrostatic Levitation.
EXAFS Extended X-ray Absorption Fine Structure.
FLD frustration limited domain.
FLDT Frustration Limited Domain theory.
HPC high-performance computing.
INS inelastic neutron scattering.
ISO icosahedral short range order.
KWW Kohlrausch-Williams-Watts.
LAMMPS Large-scale Atomic/Molecular Massively Parallel Simulator.
LCE local configuration excitation.
LPS locally preferred structure.
LRO Long range order.
mcRMC minimally constrained reverse Monte Carlo.
MD Molecular Dynamics.

MRO Medium range order.
MSD Mean Square Displacement.
NESL Neutron Electrostatic Levitator.
NOMAD Nanoscale-Ordered Materials Diffractometer.
ORNL Oak Ridge National Laboratory.
PEL Potential Energy Landscape.
PPCF Partial Pair Correlation Function.
PSDs position sensitive detectors.
PSF Partial Structure Factor.
RMC Reverse Monte Carlo.
SACF Stress Autocorrelation Function.
SISF Self Intermediate Scattering Function.
SNS Spallation Neutron Source.
SRO Short range order.
TPCF Total Pair Correlation Function.
TSF Total Structure Factor.
VFT Vogel-Fulcher-Tammann.
VI Voronoi Index.
VP Voronoi Polyhedron.
VUV Vacuum ultraviolet.
WASHU Washington University in Saint Louis.
WAXS Wide-angle x-ray diffraction.
WU-BESL Washington University Beamline Electrostatic Levitator.

Acknowledgements

I would like to thank my advisor, Prof. Ken Kelton, for his guidance and patience. Ken allowed me the independence to follow my own research interests while also making sure that I produced results. Though Ken is almost always close to some looming deadline, he still manages to make time to check on research progress and have chats about politics or the news. His optimism in light of failing equipment and problematic experiments was contagious and helped me through some of the more difficult times (the beginning of the BESL2016 run comes to mind). I look forward to continued collaboration on many projects in the years to come.

Within the Kelton group, I would like to thank Dr. Anup Gangopadhay for his insight and help. He is a great scientist with an outstanding knowledge of metallic glasses and liquids. I thank current members of the group: Rongrong Dai, Mark Sellers, Daniel Van Hoesen, and Xinsheng Xia for their help and camaraderie. Rongrong in particular provided a lot of advice and help over the years. I also thank past members of the group Drs.Chris Pueblo, Mark Johnson, and Matt Blodgett for their guidance, friendship, and work. In particular, Dr. Chris Pueblo for our many useful conversations and company on our many scattering experiments. Without Chris the work in this dissertation would not have been possible. Dr. Mark Johnson for allowing me to pester him with nonstop questions early in my Ph.D. program and for finding ways to pass the time on the night shift. Both Mark and Chris managed to make extremely stressful and tiresome scattering experiments bearable and sometimes even fun.

Within the physics department I would like to thank the people in the machine shop: Tony Biondo, Denny Huelsman, Nathan Lundak, and Todd Hardt for their help, experience, and stories. Sai Iyer has provided invaluable support and assistance in setting up, maintaining, and general troubleshooting of software on the HPC without which I would not have been able to finish this work. I would like to thank Dr. Ryan Soklaski for his always enlightening conversations and help with learning how to perform and analyze the molecular dynamics

simulations. Augusto Medeiros da Rosa has been a great friend, an exceptional physicist, and given me a lot of advice.

The staff at Oak Ridge National Laboratory has given their support and guidance on the many neutron scattering experiments. In particular, Doug Abernathy at ARCS was an invaluable resource on scattering and the analysis presented in this dissertation. Drs. Adam Vogt and Dante Quirinale have made the neutron scattering experiments possible and provided an incredible amount of support. I would also like to thank the staff at Argonne National Laboratory for their support. Doug Robinson at sector 6 was instrumental for making BESL2016 a success.

I would like to acknowledge my funding sources. My research was primarily funded through NSF grant DMR-12-06707 and the NASA grant NNX10AU19G. A portion of this research used resources at the Spallation Neutron Source, a DOE Office of Science User Facility operated by the Oak Ridge National Laboratory. Use of the Advanced Photon Source was supported by the U. S. Department of Energy, Office of Science, Office of Basic Energy Sciences, under Contract No. DE-AC02-06CH11357.

I would like to thank my family. You have all been there for me since the very beginning giving me love, support, and frequent requests for math and physics tutoring. Finally, I would like to thank my wife, Salina. You have been with me through everything: hearing my complaints, dealing with the cats while I was away on experiments, and traveling much less than you wanted just so I could continue working. Your encouragement and support (not to mention proofreading) has made this possible. Thank you for everything.

Robert Ashcraft

Washington University in St. Louis

December, 2018

ABSTRACT OF THE DISSERTATION

Linking Structure and Dynamics in Metallic Liquids: A Combined Experimental and Molecular Dynamics Approach

by

Robert Alden Ashcraft

Doctor of Philosophy in Physics

Washington University in St.Louis, 2018

Professor Kenneth F. Kelton (Chair)

A major outstanding problem in condensed matter physics is the nature of the glass transition, in which a rapidly cooled liquid can bypass the transition into a crystalline state and the liquid structure is "frozen-in" due to kinetic arrest. To characterize the fundamental features behind this transition the liquid, both in the high temperature (equilibrium) and supercooled state, needs to be better understood. By examining the relationship between structure and dynamics a better characterization of the liquid state and a determination of the mechanisms that are ultimately important for the formation of the glass can be gained. In this dissertation, elastic X-ray and inelastic neutron diffraction measurements (made using the electrostatic levitation technique), coupled with both reverse Monte Carlo (RMC) and molecular dynamics (MD) simulations are presented. These studies detail important connections between the structure and dynamics that may aid in the understanding of the glass transition. The RMC technique, which is a common method for obtaining plausible atomic configurations from diffraction data, is examined to determine the properties that are reliable when using few diffraction measurements as constraints. The liquid bond length, obtained from X-ray diffraction measurements and associated RMC simulations, is examined using the nearest-neighbor distance distribution. These studies demonstrate that the local structure is related to the liquid fragility, a measure of temperature dependence of viscosity,

through the thermal expansion coefficient. An analysis of the X-ray diffraction data also demonstrates that a crossover from Arrhenius to super-Arrhenius temperature dependence of the viscosity at a temperature (T_A) can be related to the onset of an accelerated development of a well-defined next-nearest neighbor length scale. Finally, new measurements of the dynamic pair correlation function obtained from inelastic neutron scattering studies of a $Pt - Zr$ metallic liquid, combined with molecular dynamics simulations, show that above T_A the viscosity is controlled by atoms leaving or joining a local cluster. Taken together, these three results give a coherent picture that relates structure and dynamics in equilibrium supercooled liquids.

Chapter 1: Introduction

The fact that some liquids form glasses more easily upon cooling than others remains a fundamental question in condensed matter physics. Metallic glasses, and other amorphous solids in general, have many superior properties over those of crystalline systems, such as high corrosion resistance, strength, and hardness [1]. Because of this, metallic glasses have many promising uses, including some biomedical applications [2]. This dissertation will contribute to the understanding of metallic liquids and their transition to glasses, by examining the link between structure and dynamics in the equilibrium and supercooled liquid. However, to accomplish this it is necessary to first review the relevant literature on metallic liquids, glasses, and the glass transition. The remaining sections of this chapter will give a general overview of the structure of liquids and glasses, explore the dynamics of the equilibrium and supercooled liquid, discuss fragility as a link between structure and dynamics, and finally discuss the use of containerless processing for studying supercooled liquids.

1.1 Overview of Glass and Liquid Structure

Structurally, liquids and glasses are extremely similar [3], especially when compared to the large differences with gas or crystalline systems. Crystalline systems exhibit a characteristic atomic Long range order (LRO) where a unit cell is repeated across some periodic lattice. Figure 1.1 gives a schematic comparison of atomic positions in a hexagonal close packed crystalline system and a metallic glass (bonds are indicated by overlapping grey circles). The difference between the two systems is quite clear. Though glasses do not exhibit the LRO typical of crystalline systems they do exhibit marked Short range order (SRO) (typically icosahedral short range order (ISO) in metallic liquids and glasses [4]). The schematic diagram shows some SRO since each atom on average has $\sim$ 6 nearest neighbors. Some

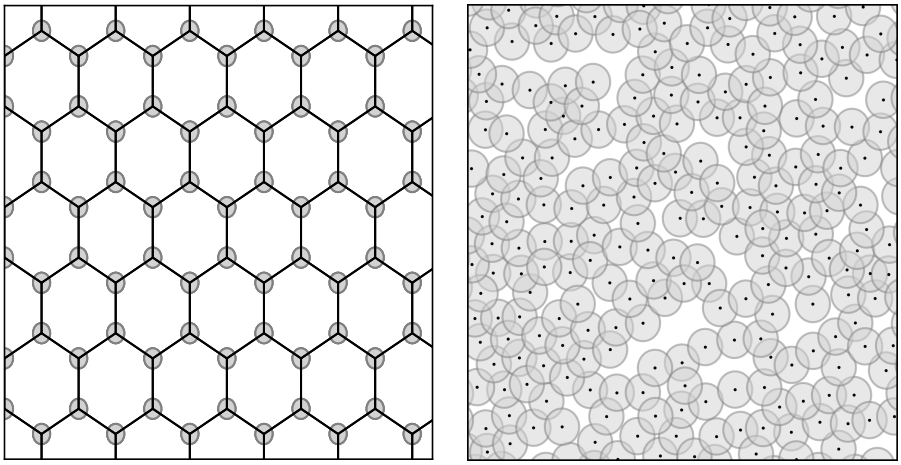

Figure 1.1: Schematic two-dimensional representation of the order in crystal and glass systems. The left shows a crystalline system with a hexagonal lattice. The right shows a glassy system.

clusters even exhibit Medium range order (MRO). If Fig 1.1 were to include a panel for the liquid system it would be, for all intents and purposes, indistinguishable from the glass.

A common way to examine the structure from scattering experiments and simulations is to use the pair correlation function $g(r)$, defined as

$$g(r) = \frac{1}{4\pi N \rho_0 r^2} \sum_i \sum_{j \neq i} \delta(r - r_{ij}) \ , \tag{1.1}$$

where N is the number of atoms, ρ_0 is the number density, $r_{ij} \equiv |\mathbf{r}_i - \mathbf{r}_j|$ is the magnitude of the distance from atom i to atom j and δ is the Dirac delta function. By definition this function gives the likelihood for finding atoms at a given distance from each other. The likelihood is exhibited by peaks and valleys where a more intense peak signals a larger likelihood of finding atoms at that distance. The function is normalized so that there is no correlation for $g(r) = 1$. From this we would expect to find sharp intense peaks in the crystalline systems, while both the liquid and glass should show more diffuse peaks and, likely, be rather similar (Figure 1.2). The Fourier transform of $g(r)$ called the static structure

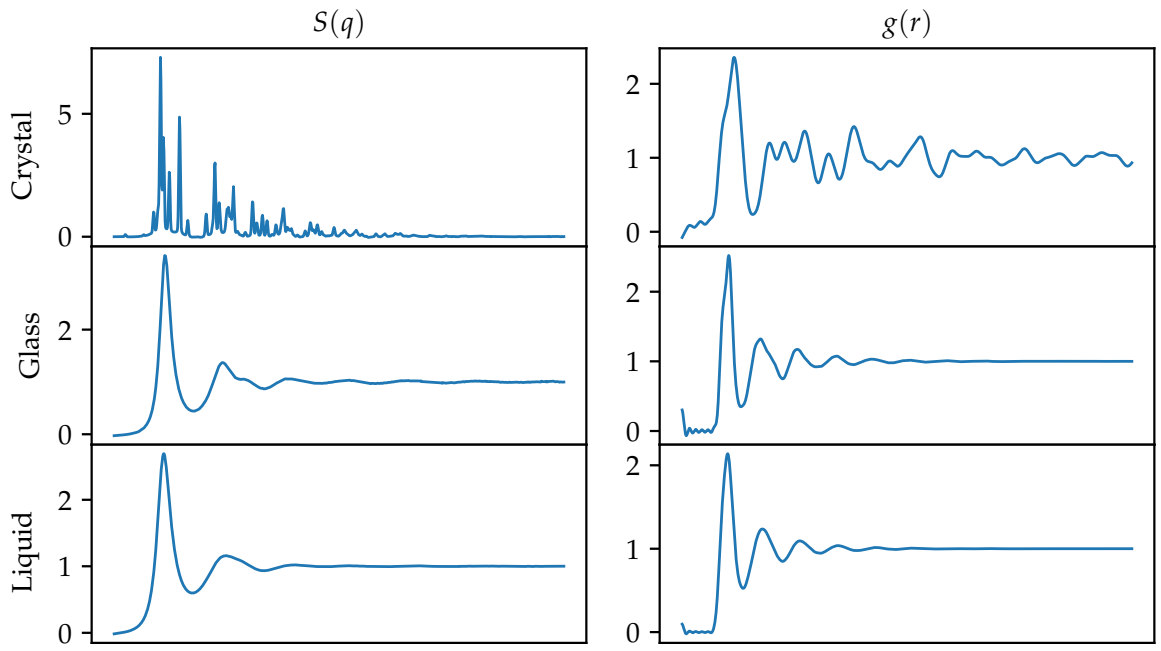

Figure 1.2: Example plots of crystal, amorphous, and liquid pair distribution functions and corresponding static structure factors.

factor, $S(q)$,

$$S(q) = 4\pi\rho_0 \int (g(r) - 1) \frac{\sin(qr)}{qr} r^2 \mathrm{d}r \ , \tag{1.2}$$

which contains complementary information in the inverse space. The structure factor is proportional to the intensity measured in diffraction experiments. As the temperature of the liquid is lowered the peaks, in both $g(r)$ and $S(q)$, sharpen and intensify, indicating that the glass (which can in terms of the structure be thought of as a low temperature liquid) is more ordered than the corresponding liquid. Also, the second peak of $S(q)$ begins to develop a shoulder in the high temperature liquid, which becomes exaggerated in the glass (this has been linked to ISO [5, 6] and is discussed in more in Chapter 5).

Icosahedral short range order was first suggested by Frank [7] to explain the ability to supercool metallic liquids. He hypothesized that the icosahedron was the energetically preferred local structure in metallic liquids and essentially poisoned the formation of a local order that is compatible with a crystal structure. While many studies have confirmed the

presence of ISO in many metallic liquids [5, 8], not all metallic liquids prefer this ordering [9]. Since icosahedra have 5-fold rotational symmetry they are unable to tile three-dimensional space, precluding the possibility of LRO. Due to the inability to tile the entire space with the energetically preferred structure the system exhibits frustrated behavior (which is discussed in the next section).

1.2 Supercooled Liquids

As a liquid is cooled atoms become less mobile and the viscosity, η, increases by over 12 to 15 orders of magnitude as the glass transition temperature, T_g, is approached. The glass transition temperature is defined as the temperature at which the viscosity reaches 10^{12} Pa s. This definition, while convenient, is functional and does not coincide with a phase transition in the supercooled liquid [3, 10]. Rather it coincides, roughly, to the point at which the dynamics become slow enough that the atomic reconfigurations necessary to maintain equilibrium (i.e. dissipate shear stress) upon further cooling, cannot keep up and ergodicity, on say the laboratory time scale, is broken.

In light of this extreme change, in viscosity, it is informative to examine the dynamic correlation functions of the supercooled liquid. The mean square displacement trajectories, $\langle \delta r^2(t) \rangle$, obtained from Molecular Dynamics (MD) simulations are shown in Fig. 1.3 for temperatures spanning the high temperature liquid down into the supercooled regime. At first atoms exhibit a simple ballistic motion at short times (<100 fs) which changes to diffusive motion in the long-time limit. However, as the liquid is cooled atoms tend to become stuck after the ballistic regime, i.e. after collisions, without appreciable motion. This caging effect, where multiple collisions keep the atoms contained, acts to delay the onset of diffusive motion. As the liquid is cooled further diffusive motion is delayed even longer until diffusion no longer occurs on simulation timescales. A similar type of decay (initial ballistic decay, β relaxation, followed by a plateau and a final decay,α-relaxation) is exhibited in other dynamic

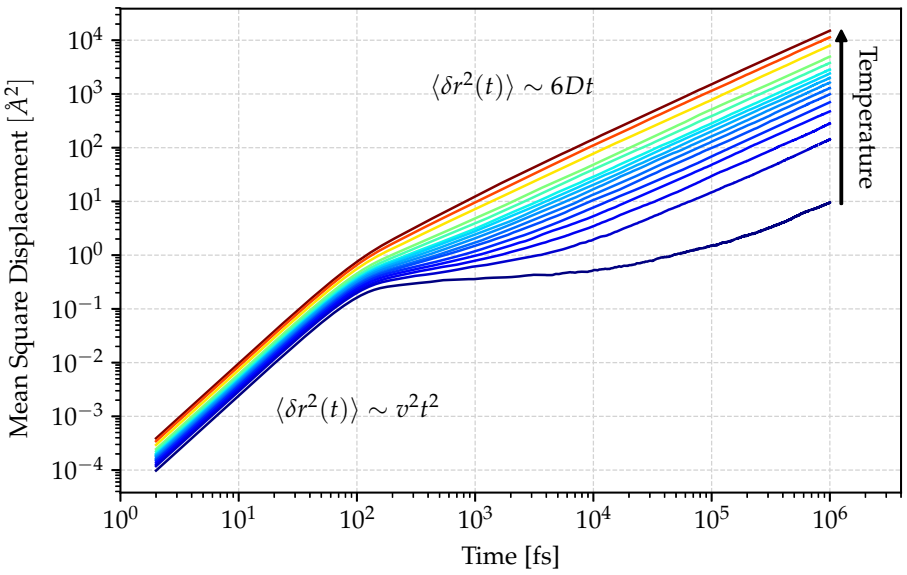

Figure 1.3: Example log-log plot of the mean square displacement, $\langle \delta r^2(t) \rangle$, of an atom in a liquid spanning the high temperature regime and the supercooled liquid. The mean square displacement shows caging effects, i.e. plateauing, characteristic of the impending glass transition.

correlation functions and is a signature of glassy behavior [3].

Many theories attempting to explain the glass transition exist (i.e. mode coupling, p-spin, Adam-Gibbs Di Marzio etc.); these are discussed in Cavagna's review article [3]. We will focus here instead on only the Frustration Limited Domain theory (FLDT)[11, 12], since it produces a useful [13, 14] relation for the viscosity and it uses the earlier idea of metallic liquids being frustrated systems. In FLDT it is assumed that the liquid has a locally preferred structure (LPS), different from that of the crystal, and that the system would crystallize at a second order critical point at T_A (T^* in the original work [11]). The crystallization is, however, prevented due to frustration coming from the incompatibility of the LPS with LRO. Though the frustration kills the phase transition at T_A, it is assumed that it still controls much of the physics for the system. Since the LPS is energetically favorable small domains will try to maintain this order while the system forces breaks in the ordering, of size $\xi(T)$, to relieve the system frustration. Above T_A the system exists freely in the disordered liquid, while as the temperature is lowered below T_A the size of the domains $\xi(T)$ grows and

causes the rapid slowdown in the system dynamics. The temperature T_A then denotes the change from Arrhenius to super-Arrhenius behavior in dynamical properties like viscosity. FLDT predicts the following form for the viscosity:

$$\eta(t) = \eta_0 \exp\left(\frac{E_\infty}{k_B T} + \frac{T_A}{T}\left(1 - \frac{T}{T_A}\right)^z \Theta(T_A - T)\right) \tag{1.3}$$

where the first term $\frac{E_\infty}{k_B T}$ gives the Arrhenius contribution and the second the super-Arrhenius modification. In FLDT theory the fast β relaxation is associated with relaxations within a FLD while α relaxation is associated restructuring of the FLD. This indicates that cooperation over longer length scales becomes necessary to relax the liquid, starting at the crossover T_A.

A schematic representation of the viscosity (using Eq. 1.3 as a basis) and the large variability of behaviors it exhibits for different liquids upon cooling is shown in Fig. 1.4. This type of plot, showing $\log_{10}(\eta)$ as a function of T_g/T is called an Angell plot [15]. The Angell plot naturally introduces the property of fragility, which is a measure of the deviation from the constant activation energy or Arrhenius behavior when cooling the liquid. This property will be discussed more thoroughly in the next section.

1.3 Linking Structure and Dynamics

As mentioned previously, fragility is the deviation of viscosity from Arrhenius behavior. Liquids with small deviations are considered strong while systems showing a super Arrhenius behavior are fragile. Figure 1.4 shows a schematic representation of two extreme cases for strong and fragile liquids, as well as an intermediate regime where metallic liquids are found. The fragility can be quantified by the slope of the viscosity curve on an Angell plot at T_g:

$$m = \left.\frac{\mathrm{d}\log_{10}(\eta)}{\mathrm{d}(T_g/T)}\right|_{T=T_g}. \tag{1.4}$$

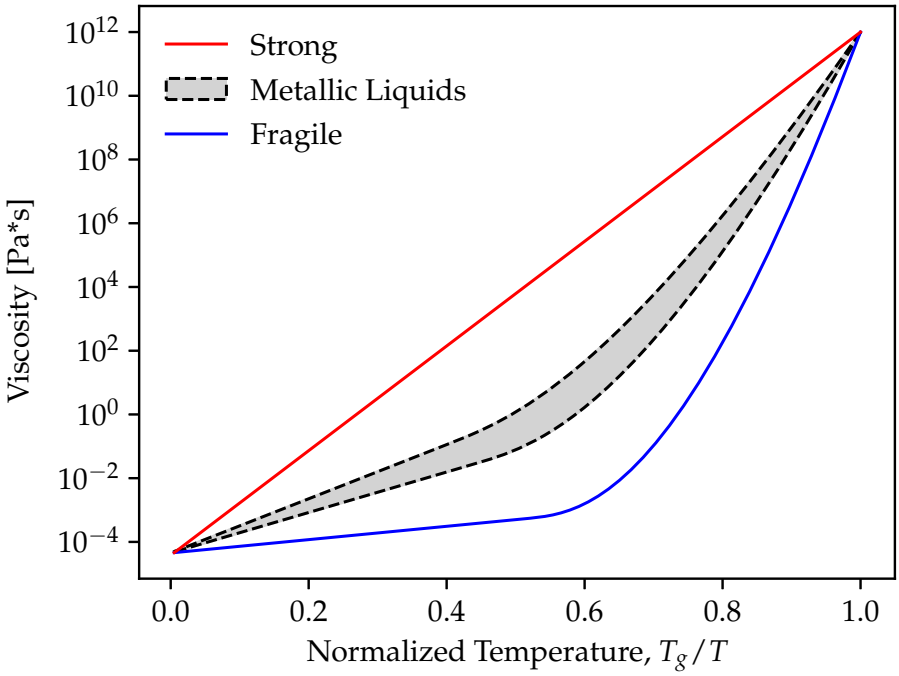

Figure 1.4: Schematic Angell plot for viscosity, η, on a log scale versus inverse temperature normalized to the glass transition temperature, T_g. By convention $\eta(T_g) = 10^{12}$ Pa s. Metallic liquids are typically in the intermediate range.

This has long been the most common method for determining liquid fragility, but is not applicable to systems that are unable to form a glass. Further, since this dissertation focuses on the liquid it is also not applicable. A popular (but unfortunate) choice that is also used for fragility comes from the Vogel-Fulcher-Tammann (VFT) fit equation

$$\eta = \eta_0 e^{\frac{D^* T_0}{T - T_0}} \tag{1.5}$$

where η_0 is the high temperature limit of viscosity, T_0 is the temperature where the viscosity diverges, and D^* is the fragility parameter. The use of the VFT equation is unfortunate, since the choice of T_0 and the range which is chosen greatly affects the fragility parameter and can give incorrect values. Several other fragility parameters exist, all based on intersecting the Angell plot of viscosity with a line and using the scaled temperature at the intersection to construct the fragility parameter [16–18].

Another connection between structure and dynamics comes from recent MD calculations that have examined the fundamental excitation of the atomic cluster [19–21]. A central atom and all of its neighbors, all atoms within a radial distance d of the central atom, are tracked as a function of time. A local configuration excitation (LCE) occurs when an atom crosses the cutoff distance, either leaving or joining the cluster (Fig. 1.5). The average time for such an excitation to occur is called the local configuration time, τ_{LC}. These studies show that $\tau_{LC} \approx \tau_M$ for $T > T_A$ where τ_M, the Maxwell time, is the shear stress decorrelation time and T_A is the Arrhenius crossover temperature defined previously. The authors argue that the LCEs then are the fundamental excitation controlling the relaxation time of dynamics (i.e. viscosity). In the previous section FLDT predicted that cooperative motion occurs above the crossover temperature T_A which appears to be corroborated by the studies presented here. A combined experimental and MD examination of this study is presented in Chapter 6.

The last structure-dynamics relation discussed here is through the Adam-Gibbs rela-

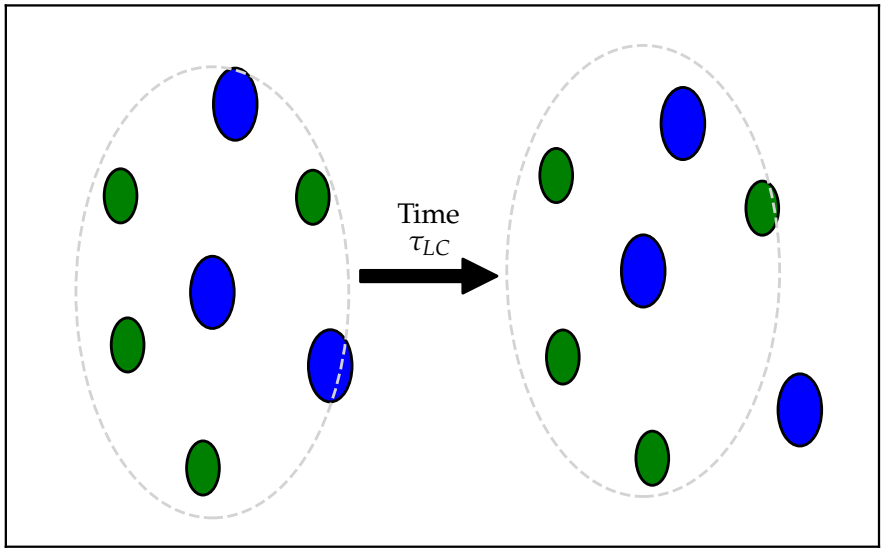

Figure 1.5: Two-dimensional illustration of a local configuration excitation. The configuration on the left show a central atom and its nearest-neighbors all located within some distance cutoff of the central atom. After a time interval τ_{LC} has passed one of the local atoms has passed the cutoff distance and is not considered part of the cluster anymore.

tion [22]

$$\eta = \eta_0 \exp\left(\frac{B}{TS_c(t)}\right) \ , \tag{1.6}$$

where B is a constant and $S_c(t)$ is the temperature-dependent configurational entropy. Comparing this relation with the VFT relation (Eq. 1.5), we see that $D^* \sim 1/S_c$ indicating an inverse relationship between fragility and configurational entropy. This is a simple structure-dynamics connection implying that strong liquids are better ordered [23].

It is also informative to compare the configurational entropy to Eq. 1.3 from FLDT, which builds on the well-known Potential Energy Landscape (PEL) [24] (Fig. 1.6). Using the Adam-Gibbs relation and FLDT the configurational entropy decreases linearly in the high temperature liquid, above the landscape's many peaks and valleys, but begins to rapidly decrease as T decreases below T_A. At T_A the system starts to appreciably interact with the PEL by choosing a basin. This corresponds to the FLD growing and the number of configurations being reduced, indicating that correlations are being maintained within the domains (β relaxation). To switch basins (i.e. α relaxation) a reorientation of the FLDs is

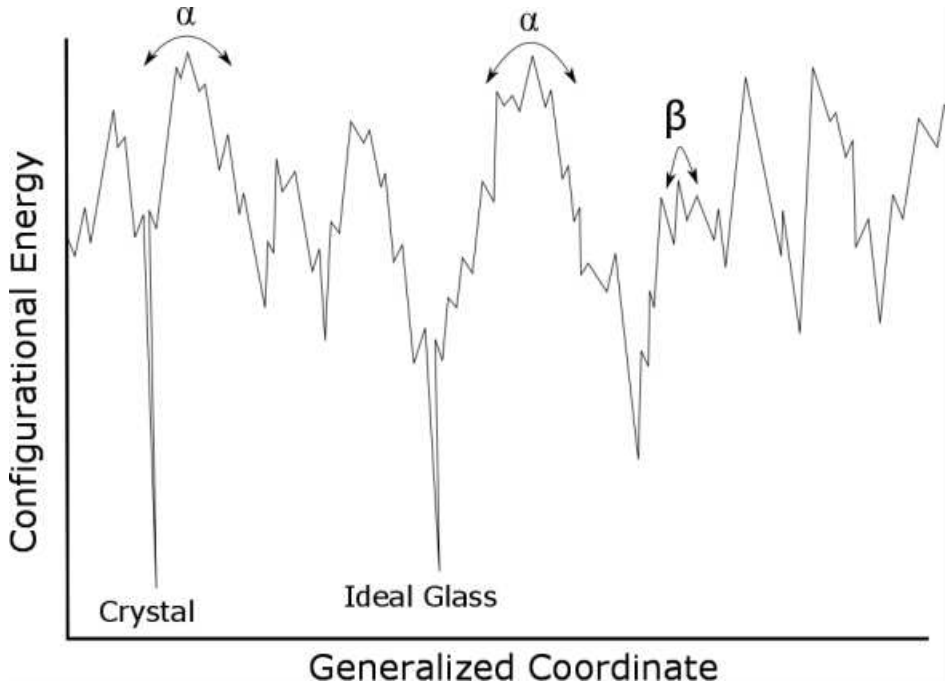

Figure 1.6: Schematic diagram of the potential energy landscape for a fragile glass forming liquid. Energy barriers for the fast β transition and slow α transition are shown. Figure reprinted with permission from [25]

needed. This shows the freezing out occurring in the glass transition corresponding to the reduction of the number of FLDs and the increasing of size of the remaining domains

1.4 Containerless Processing

As previously mentioned the supercooled liquid is accessible only if heterogeneous nucleation sites are removed. It should be noted that homogeneous nucleation, which is due to thermal density fluctuations, will still lead to crystallization, but typically at a deep supercooling. The reactivity of metallic liquids is another source of concern when studying them. If a container is used to hold the liquid it is likely that it will act as a heterogeneous nucleation site and/or alloy with the liquid of interest. To circumvent these issues the sample container can be removed entirely and the sample is levitated. This has the added benefit of reducing the background signal, if there is clear line-of-sight to the sample, for diffraction measurements.

Through the years several levitation techniques have been introduced and used to study liquids; these methods are briefly mentioned here but-in depth comparisons can be found elsewhere [26–28]. Acoustic levitation [29] uses focused sound waves to levitate samples in a three-dimensional potential well. This method typically is only used on lower density samples, since the pressure needed to levitate dense samples is likely to deform and fragment the liquid droplet. Aerodynamic levitation [30] uses a jet of gas to counteract gravity and levitate the sample, which can then be heated using high-powered lasers. This method has two major drawbacks: the sample typically does not float very far above the gas nozzle limiting the scattering window and the flow of gas can cause large temperature gradients. A combination of these two techniques however (aero-acoustic levitation [31]) shows considerable improvement on the limitations of each method. Electromagnetic Levitation (EML) [32] uses radio-frequency electromagnetic fields for levitation. Since levitation is coupled to heating, the eddy (Foucault) currents that heat the sample also levitate it via Lenz's law, the temperatures that can be examined are limited. Furthermore, since the coils must surround the sample the available scattering window for diffraction measurements is reduced.

The technique used in this dissertation is Electrostatic Levitation (ESL) [33] (discussed in more detail in Chapter 2), which uses a pair of electrodes with a large negative potential difference to induce a positive surface charge on the sample surface causing levitation via coulomb attraction. Compared to the techniques previously mentioned ESL has a smaller scattering background than EML and aerodynamic levitation. The temperature, which is controlled via heating lasers, has a larger range than for EML and a smaller temperature gradient than for aerodynamic levitation. While EML can only be used on metallic systems, ESL can be used on any material that can sustain a surface charge. From this list it would seem that either ESL or aero-acoustic levitation are the best options, but both suffer from an increased complexity that can make levitation difficult. For instance, upon heating in ESL surface charge can be carried off by the evaporation of contaminants, which destabilizes levitation. This can be countered, however, by recharging the sample via the photoelectric

effect using a Vacuum ultraviolet (VUV) source. This method has been used successfully for many X-ray and neutron diffraction studies [5, 34–36] and thermophysical measurements [37–40] (to list a few).

1.5 Summary

This chapter covered the background needed for the following chapters and framed this work in the context of a larger recent push to understand the relation between structure and dynamics in metallic liquids. Descriptions of experimental and simulation techniques and the analysis of the obtained data obtained in this dissertation are discussed in Chapter 2. Molecular dynamics calculations are presented in Chapter 3 to examine the reliability of Reverse Monte Carlo simulations, which are frequently used to determine the atomic structure from diffraction measurements. Chapter 4 uses both molecular dynamics and X-ray diffraction measurements to show that the thermal expansion coefficient in metallic liquids is determined from the expansion of nearest neighbor atoms, in contrast with recent claims. X-ray diffraction measurements are presented in Chapter 5, which demonstrate that the dynamic crossover temperature, T_A, is related to an acceleration of the growth of a length scale that is on the order of next-nearest-neighbors. Chapter 6 presents equilibrium and supercooled INS and viscosity measurements for $Zr_{80}Pt_{20}$ and shows that at high temperatures the Maxwell relaxation time equals the local configuration time, providing experimental confirmation of recent MD predictions experimentally concerning the origin of the high temperature viscosity.

1.6 References

[1] A. Inoue and A. Takeuchi. Recent Progress in Bulk Glassy Alloys. *Materials Transactions* **43**,8 (2002). DOI: 10.2320/matertrans.43.1892.

[2] S. L. Zhu et al. A new Ti-based bulk glassy alloy with potential for biomedical application. *Materials Science and Engineering A* **459**,1-2 (2007). DOI: 10.1016/j.msea.2007.01.044.

[3] A. Cavagna. Supercooled liquids for pedestrians. *Physics Reports* **476**, (2009). DOI: 10.1016/j.physrep.2009.03.003. arXiv: 0903.4264.

[4] Y. Q. Cheng and E. Ma. Atomic-level structure and structure-property relationship in metallic glasses. *Progress in Materials Science* **56**,December 2010 (2011). DOI: 10.1016/j.pmatsci.2010.12.002.

[5] K. F. Kelton et al. First X-Ray Scattering Studies on Electrostatically Levitated Metallic Liquids: Demonstrated Influence of Local Icosahedral Order on the Nucleation Barrier. *Physical Review Letters* **90**,19 (2003). DOI: 10.1103/PhysRevLett.90.195504.

[6] G. W. Lee et al. Local structure of equilibrium and supercooled Ti-Zr-Ni liquids. *Physical Review B - Condensed Matter and Materials Physics* **77**,18 (2008). DOI: 10.1103/PhysRevB.77.184102.

[7] F. Frank. Supercooling of Liquids. *Proceedings of the Royal Society of London* **215**,1120 (1952). DOI: 10.1038/143722a0.

[8] T. Schenk et al. Icosahedral short-range order in deeply undercooled metallic melts. *Physical Review Letters* **89**,7 (2002). DOI: 10.1103/PhysRevLett.89.075507.

[9] F. Demmel and C. Morkel. No evidence for ideal icosahedrons in liquid rubidium. *Physics and Chemistry of Liquids* **50**,1 (2012). DOI: 10.1080/00319104.2011.590989.

[10] J. P. Sethna. Statistical Mechanics: Entropy, Order Parameters, and Complexity. In: *Oxford Master Series in Statistical, Computational, and Theoretical Physics*. University Press, 2012.

[11] D. Kivelson et al. A thermodynamic theory of supercooled liquids. *Physica A: Statistical Mechanics and its Applications* **219**,1-2 (1995). DOI: 10.1016/0378-4371(95)00140-3.

[12] G. Tarjus et al. The frustration-based approach of supercooled liquids and the glass transition: a review and critical assessment. **1143**, (2005). DOI: 10.1088/0953-8984/17/50/R01. arXiv: 0509127 [cond-mat].

[13] M. E. Blodgett et al. Proposal for universality in the viscosity of metallic liquids. *Scientific Reports* **5**, (2015). DOI: 10.1038/srep13837.

[14] C. E. Pueblo, M. Sun, and K. F. Kelton. Strength of the repulsive part of the interatomic potential determines fragility in metallic liquids. *Nature Materials* **16**,8 (2017). DOI: 10.1038/nmat4935.

[15] C. Angell. Relaxation in liquids, polymers and plastic crystals - strong/fragile patterns and problems. *Journal of Non-Crystalline Solids* **131-133**, (1991). DOI: 10.1016/0022-3093(91)90266-9.

[16] K. Ito, C. T. Moynihan, and C. A. Angell. Thermodynamic determination of fragility in liquids and a fragile-to-strong liquid transition in water. *Nature* **398**,April (1999). DOI: 10.1038/19042.

[17] A. K. Gangopadhyay et al. Correlation of the fragility of metallic liquids with the high temperature structure, volume, and cohesive energy. *Journal of Chemical Physics* **146**,15 (2017). DOI: 10.1063/1.4981011.

[18] A. Jaiswal et al. Correlation between Fragility and the Arrhenius Crossover Phenomenon in Metallic, Molecular, and Network Liquids. *Physical Review Letters* **117**,20 (2016). DOI: 10.1103/PhysRevLett.117.205701. arXiv: 1604.08920.

[19] T. Iwashita, D. M. Nicholson, and T. Egami. Elementary Excitations and Crossover Phenomenon in Liquids. *Physical Review Letters* **110**,20 (2013). DOI: 10.1103/PhysRevLett.110.205504.

[20] T. Iwashita and T. Egami. Local energy landscape in a simple liquid. *Physical Review E* **90**,5 (2014). DOI: 10.1103/PhysRevE.90.052307.

[21] R. Soklaski et al. A locally preferred structure characterises all dynamical regimes of a supercooled liquid. *Philosophical Magazine* **96**,12 (2016). DOI: 10.1080/14786435.2016.1158427. arXiv: 1502.01739.

[22] G. Adam and J. H. Gibbs. On the Temperature Dependence of Cooperative Relaxation Properties in Glass Forming Liquids. *The Journal of Chemical Physics* **43**,1 (1965). DOI: 10.1063/1.1696442. arXiv: arXiv:1011.1669v3.

[23] S. Wei et al. The impact of fragility on the calorimetric glass transition in bulk metallic glasses. *Intermetallics* **55**, (2014). DOI: 10.1016/j.intermet.2014.07.018.

[24] P. Debenedetti and F. Stillinger. Supercooled liquids and the glass transition. *Nature* **410**,6825 (2001). DOI: 10.1038/35065704. arXiv: 9911023v1 [arXiv:cond-mat].

[25] C. E. Pueblo. Ground and Flight Based Studies of Nucleation and Thermophysical Properties in Metallic Glass Forming Systems. PhD thesis. Washington University in St. Louis, 2016. DOI: 10.7936/K7PN942Z.

[26] G. J. Cuello et al. Neutron scattering at high temperature and levitation techniques. *Journal of Physics: Conference Series* **549**, (2014). DOI: 10.1088/1742-6596/549/1/012002.

[27] P. C. Nordine, J. K. R. Weber, and J. G. Abadie. Properties of high-temperature melts using levitation. *Pure and Applied Chemistry* **72**,11 (2000). DOI: 10.1351/pac200072112127.

[28] K. F. Kelton and A. L. Greer. *Nucleation in Condensed Matter*. Pergamon, 2010.

[29] E. H. Trinh and K. Ohsaka. Measurement of Density , Sound Velocity , Surface Tension , and Viscosity of Freely Suspended Supercooled Liquids. *International Journal of Thermophysics* **16**,2 (1995).

[30] L. Hennet et al. Structure and dynamics of levitated liquid aluminates. *Journal of Non-Crystalline Solids* **353**,18-21 (2007). DOI: 10.1016/j.jnoncrysol.2007.01.040.

[31] J. K. R. Weber et al. Aero-acoustic levitation: A method for containerless liquid-phase processing at high temperatures. *Review of Scientific Instruments* **65**,2 (1994). DOI: 10.1063/1.1145157.

[32] D. Holland-Moritz et al. Electromagnetic levitation apparatus for diffraction investigations on the short-range order of undercooled metallic melts. *Measurement Science and Technology* **16**,2 (2005). DOI: 10.1088/0957-0233/16/2/007.

[33] W. K. Rhim et al. Development of an electrostatic positioner for space material processing. *Review of Scientific Instruments* **56**,2 (1985). DOI: 10.1063/1.1138349.

[34] T. Kordel et al. Neutron scattering experiments on liquid droplets using electrostatic levitation. *Physical Review B* **83**, (2011). DOI: 10.1103/PhysRevB.83.104205.

[35] M. L. Johnson et al. Structural evolution and thermophysical properties of ZrxNi100-x metallic liquids and glasses. *Journal of Non-Crystalline Solids* **405**, (2014). DOI: 10.1016/j.jnoncrysol.2014.10.026.

[36] M. L. Johnson et al. Measurements of structural and chemical order in Zr80Pt20 and Zr77Rh23 liquids. *Physical Review B* **93**,5 (2016). DOI: 10.1103/PhysRevB.93.054203.

[37] W.-k. Rhim et al. An electrostatic levitator for high-temperature containerless materials processing 1-g. *Review of Scientific Instruments* **64**,10 (1993).

[38] S. Klein, D. Holland-Moritz, and D. M. Herlach. Crystal nucleation in undercooled liquid zirconium. *Physical Review B - Condensed Matter and Materials Physics* **80**,21 (2009). DOI: 10.1103/PhysRevB.80.212202.

[39] S. Jeon et al. Effect of atomic size on undercoolability of binary solid solution alloy liquids with Zr, Ti, and Hf using electrostatic levitation. *The Journal of Chemical Physics* **145**,17 (2016). DOI: 10.1063/1.4966649.

[40] L. H. Li et al. Thermodynamic properties and solidification kinetics of intermetallic Ni7Zr2 alloy investigated by electrostatic levitation technique and theoretical calculations. *Journal of Applied Physics* **119**,3 (2016). DOI: 10.1063/1.4940243.

Chapter 2: Experimental, Simulation, and Analysis Methods

The large scale of the experiments presented in this thesis made it necessary for many group members and collaborators to be involved in the data acquisition, analysis, and preparation of samples. This included: A. K. Gangopadhyay, A. J. Vogt, C. E. Pueblo, M. L. Johnson, M. Sellers, R. Dai, D. Quirinale (Iowa State University/Oak Ridge National Laboratory), D. Van Hoesen, and Z. Wang (University of Tennessee Knoxville). The following sections describe the methods for sample preparation (Sec. 2.1), the setup of both the BESL and NESL (Sec. 2.2), thermophysical properties characterization (Sec.2.3), neutron and X-ray diffraction theory, analysis, and experiments (Sec. 2.4), and simulation details and analysis (Sec. 2.5).

2.1 Sample Preparation

Master ingots (1-2.5 g) were prepared from high purity elemental source material (typically obtained from Alfa Aesar, now Fischer Scientific). The source material, to prevent surface oxidation, was stored in a glove box filled with 99.998% argon atmosphere and were only retrieved prior to weighing and arc-melting. The necessary mass of source material for element i, m_i, is given by

$$m_i = \frac{x_i M_i}{\sum_j^N x_j M_j} m_I \tag{2.1}$$

where x_i and M_i are the atomic percent and molar mass, respectively, of the i-th element, N is the number of elements and m_I is the total mass of the master ingot. The source material was weighed using a Mettler Toledo AB54/FACT mass balance, which has a precision of ± 0.1 mg or nominally, for a 1 g ingot, 0.009-0.05 atomic percent (see Fig 2.1b).

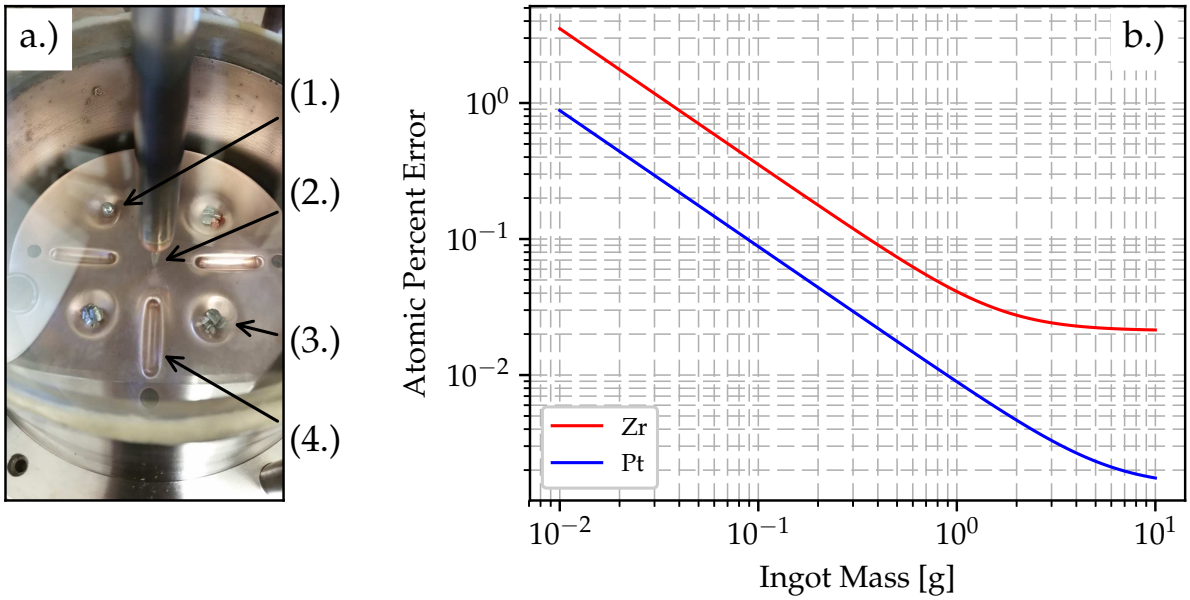

Figure 2.1: a.) Photograph of the arc-melter: (1.) is the $Ti_{50}Zr_{50}$ getter, (2.) is the tungsten tip attached to the vacuum feedthrough, (3.) a $Zr_{70}Ni_{20}Al_{10}$ ingot material prior to arc-melting, and (4.) a trough for holding the sample material. b.) A plot of the nominal error in the atomic percent as a function of ingot mass due to the error of the mass balance for $Zr_{80}Pt_{20}$.

The measured material was placed on a water-cooled copper hearth with the highest melting temperature element or the largest piece of material (if the highest melting temperature element is considerably smaller) placed on top (nearest to the tungsten tip from which the arc is struck) as shown in Fig. 2.1a. The arc-melting chamber was then evacuated to 5.0×10^{-6}-5.0×10^{-5} Torr(typically 15-30 min) and back-filled with high purity (99.999%) Ar. This pump and refill cycle was repeated three times to further reduce the oxygen content prior to arc-melting. After the final cycle the chamber was back-filled with Ar to approximately 600 Torr.

The arc, powered by a Miller Synchrowave 250DX arc-welding power source connected to the tungsten tip through a vacuum feedthrough, was initially struck over the copper hearth before melting a $Ti_{50}Zr_{50}$ ((1.) in Fig. 2.1a) getter, which was held molten for approximately 60 sec to further reduce the oxygen concentration. The material for each ingot was then melted by holding the arc over it and circling (to increase mixing) for 30-60 sec. After all ingots had been melted, the arc was extinguished and the tungsten tip was used to flip the ingots. After flipping the sample the arc was struck again, the $Ti_{50}Zr_{50}$ getter was melted, and each ingot re-melted. This flipping and re-melting procedure, which also increases mixing of the material, was repeated 2-3 times. The mass of the final ingot was then measured to assess the mass loss of the ingot and its possible compositional shift. If the shift in the atomic composition, determined by assuming the mass loss was due to a single element, was more than 0.05 atomic percent the ingot was rejected. More information about the arc-melter setup and procedure can be found in earlier publications [1, 2].

The ingots were subsequently crushed and portions were used to create samples for the Washington University Beamline Electrostatic Levitator (WU-BESL) measurements of viscosity, density and X-ray diffraction, as well as for Neutron Electrostatic Levitator (NESL) neutron diffraction experiments. The BESL samples are typically 30-90 mg while the NESL samples are 300-400 mg. The samples made from this method were re-melted by arc-melting following the previously outlined procedure, except the samples are melted a single time for

fractions of a second to produce more spherical samples. If the required samples are large enough, as with neutron scattering experiments, the sample can be made directly without the need for making and crushing the master ingot. This alternative method gives a better control on the sample composition since mixing of the ingot is no longer a concern (if it is indeed an issue). However, only larger samples should be made this way since, as seen in Fig. 2.1b, the nominal error in the atomic percent is increased as "ingot" mass decreases. Where "ingot" mass is a stand-in for the total sample mass. Even smaller pieces of the crushed ingot, 10-30 mg, were used for Differential Thermal Analysis (DTA) experiments.

2.2 Setup of Electrostatic Levitators

Since the liquid's structure and thermophysical properties are the main interest of this dissertation the Electrostatic Levitation (ESL) technique [3] is used to examine the high temperature and supercooled liquid by non-contact measurements. The Washington University Beamline Electrostatic Levitator (WU-BESL) was used to obtain viscosity, density, thermal expansion coefficient, and X-ray diffraction data while the Neutron Electrostatic Levitator (NESL) was used for inelastic, quasielastic, and elastic neutron diffraction. This section describes the setup of each of these facilities for the experiments mentioned in Sec. 2.4.

2.2.1 WU-BESL Setup

The Washington University Beamline Electrostatic Levitator (WU-BESL) facility uses six electrodes (two pairs of lateral and one pair of vertical electrodes) to levitate and position the samples in a high-vacuum (10^{-7} Torr) chamber. This pressure is obtained using a Pfeiffer Vacuum turbo pump for the Vacuum ultraviolet (VUV) lamp and an Osaka Vacuum turbo pump for the main chamber, each backed with a scroll pump. The lateral electrodes, which are made of stainless steel, are used to maintain a stable levitation position and are attached via a vacuum feedthrough to amplifiers that are able vary the potential difference between

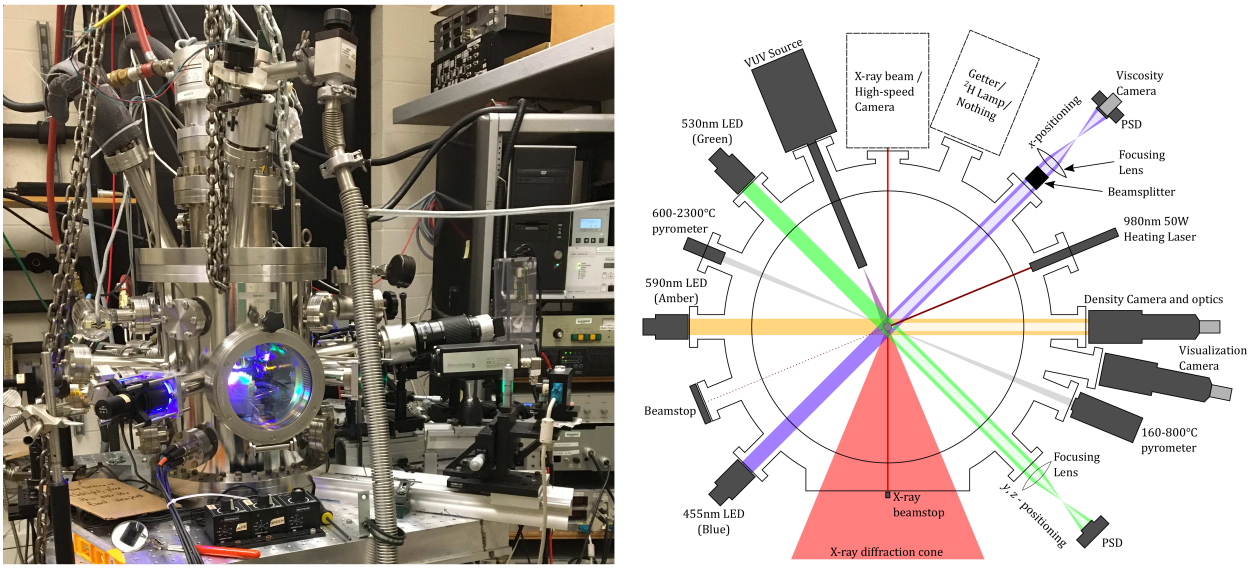

Figure 2.2: (Left) Current (September 2018) setup of the Washington University Beamline Electrostatic Levitator (WU-BESL). Photograph courtesy of Mark Sellers. (Right) Schematic diagram of the WU-BESL setup for the layout of instruments and optics used for noncontact measurements and levitation as of September 2018. Updated from the diagram in [4].

the pairs by $\pm 3\,\mathrm{kV}$. The vertical electrode pair, which are made from copper, consists of a grounded bottom electrode and a negatively charged curved top electrode powered by a high-voltage amplifier that is able to vary the potential difference between 0-$-20\,\mathrm{kV}$. The curvature of the top electrode was designed to give increased stability in the lateral direction without sacrificing significant vertical stability. These competing effects and the design of the electrodes are discussed in [4, 5].

The position of the levitated sample is tracked by examining the shadow of the sample cast onto two orthogonal position sensitive detectors (PSDs). The PSDs and sample are illuminated with two high-intensity LEDs (455 nm in the x-direction and 530 nm in the y and z-direction see Fig. 2.2). The signal from the PSDs, which contains positional information, is passed to a target computer that determines the movement of the sample and adjusts the voltages on the electrodes, via the amplifiers, to adjust the sample position and stabilize it using a feedback algorithm [6]. The position of the sample can be adjusted to a minimum of $10\,\mu\mathrm{m}$ with the current setup.

Samples are heated with a fiber-coupled diode laser (980nm, 50W continuous maximum power output); there are plans to upgrade to a 100W laser in the future. As the samples are heated surface contaminants and impurities trapped in grain boundaries are evaporated, which decrease the surface charge. Instability and even loss of the sample can occur due to large discharges. The high-intensity VUV lamp is used to maintain the charge on the sample and is necessary for the initial heating and melting. At high enough temperatures thermionic emission is typically sufficient to recharge the samples, which allows the VUV source to be shuttered off. This also helps extend the life of the VUV source as it prevents the deposition of evaporated metals, which could contaminate the source.

Temperatures were recorded via two pyrometers: a Process Sensors Metis MI18 MB8 single color pyrometer with a range of 160-800 °C operating at a 1.89 µm wavelength, and a Process Sensors Metis MQ22 two color ratio pyrometer with a range of 600-2300 °C, operating at 1.4 µm and 1.64 µm wavelengths. For the ratio pyrometer, which was of primary interest for these studies, an initial value for the emissivity was set to approximate the sample temperature. The value of the ratio of the emissivity for each wavelength was then calibrated in post-processing by matching a known thermal signature. Typically the solidus temperature, T_s, was chosen because samples exhibited long isothermal plateaus. More information about this setup and the correction can be found elsewhere [7, 8].

The WU-BESL was designed to be transportable for X-ray diffraction experiments. In these instances, the levitator and its components are packed into wooden crates and transported to the Advanced Photon Source (APS) located at Argonne National Laboratory (ANL) to be installed, for the experiments considered in this thesis, on beamline 6-ID-D, which provides a large flux of high-energy X-rays. Upon arrival the front plate and the window where the high-speed camera is usually mounted (see Fig. 2.2) are replaced with thin Beryllium windows, which has a smaller scattering cross section than the typical viewports, giving a smaller background in the X-ray diffraction data. On the X-ray beam entry port, inside the chamber, a small tungsten collimator is placed to further reduce background

scattering.

A beam stop, supplied by the beamline scientist, is placed directly in front of the beryllium window, which most recently consisted of a plastic with a steel screw in the location of the beam. Ideally the detector, typically an amorphous Si flat-panel GE Revolution 41-RT detector, would be placed level with the chamber but this is not always the case. To correct for the tilt of the detector and obtain the detector distance polycrystalline Si standards are routinely scanned and the well-known Si diffraction rings are fit.

2.2.2 NESL Setup

The Neutron Electrostatic Levitator (NESL) facility [9] is a high vacuum environment optimized for simultaneous temperature and time-of-flight neutron diffraction measurements on levitated samples, which are typically metallic liquids. The NESL was designed to be integrated on to the Nanoscale-Ordered Materials Diffractometer (NOMAD), the Wide Angular-Range Chopper Spectrometer (ARCS), and the Cold Neutron Chopper Spectrometer (CNCS) beamlines at the Spallation Neutron Source (SNS) located at Oak Ridge National Laboratory (ORNL), for elastic, inelastic, and quasielastic neutron diffraction measurements, respectively. Due to the geometry of each beamline and the desire to optimize the unobstructed scattering window available the optical signals required for processing and levitation were mounted vertically on a keystone, which sits above the detector well (Fig. 2.3). Due to this mounting all signals are bounced off of silvered mirrors to reach the sample position (Fig. 2.4).

Sample levitation and processing in the NESL is very similar to that in the WU-BESL. The NESL uses six electrodes (three pairs of electrodes) to levitate and position samples in a high vacuum environment 10^{-7} Torr, measured by a Pfeiffer PKR261 cold cathode vacuum gauge mounted on the keystone. This pressure was attainable using a Pfeiffer HiPace 700 turbomolecular pump on the main chamber and a Pfeiffer HiPace 80 turbomolecular pump on the VUV system each backed by a rough pump. All electrodes in the NESL are made of

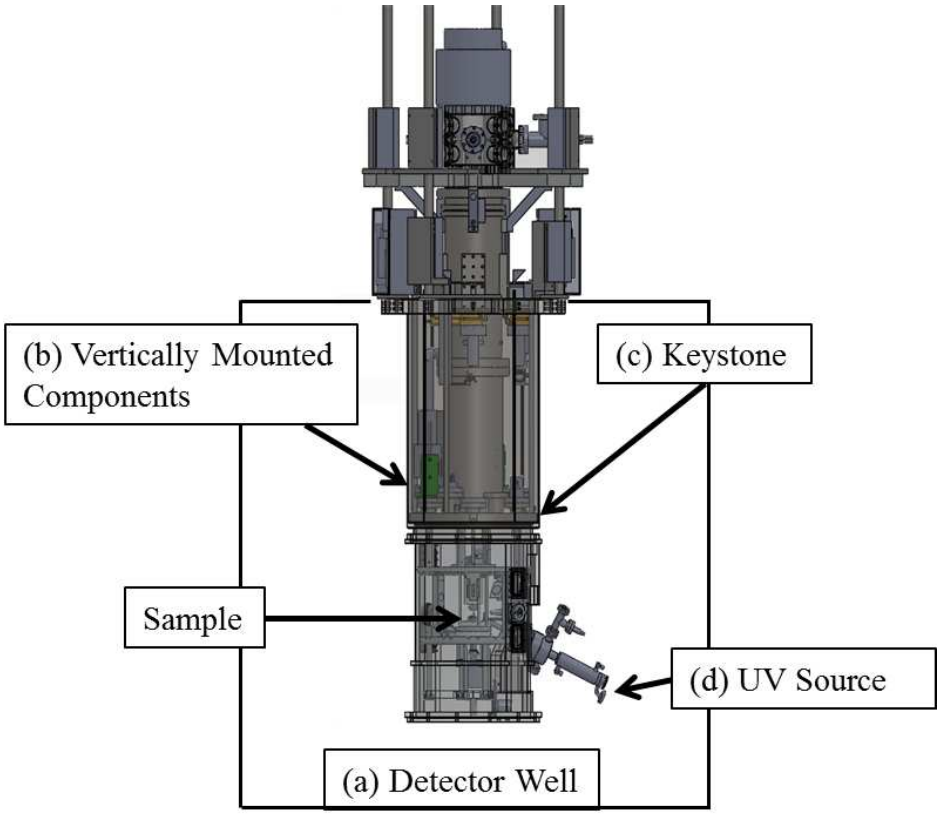

Figure 2.3: Rendering of the Neutron Electrostatic Levitator (NESL) showing how the NESL is mounted at the SNS. Since the components are mounted on the keystone to reach the sample signals must be bounced off of mirrors. Image from [2]

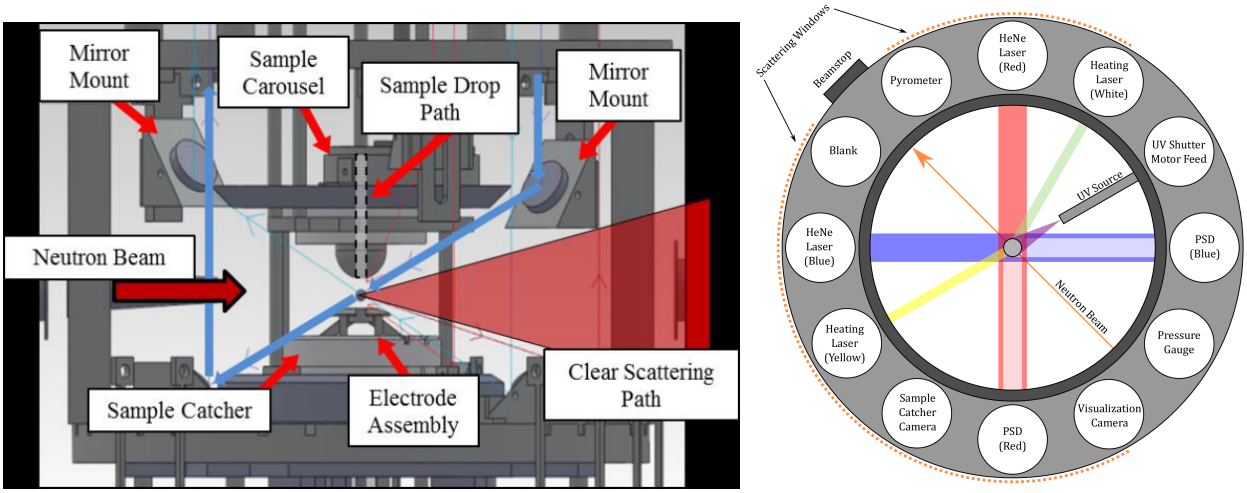

Figure 2.4: (Left) Schematic diagram showing the electrode assembly, sample catcher, and mirror platforms. The scattering path and neutron beam are shown for comparison. [Reprinted with permission from [2]].(Right) Top-view of the NESL components vertically mounted to the keystone with the incident neutron beam and scattering windows. For clarity lasers are colored while in reality they are all red or outside the visible spectrum.

aluminum (gadolinium is also available) rather than stainless steel to reduce any scattering signal from the electrodes. The lateral electrodes are attached via a vacuum feedthrough to amplifiers able to vary the potential difference, between the pairs, by $\pm 5\,\mathrm{kV}$. The vertical electrode pair consists of a grounded bottom electrode and a negatively charged curved top electrode powered via a high-voltage amplifier that is able generate a potential difference as high as $-30\,\mathrm{kV}$.

The position of the levitated sample was tracked using a pair of Helium-Neon (HeNe) positioning lasers, which are arbitrarily denoted as red and blue (see Fig. 2.4), rather than high-intensity LEDs. This is because the LEDs will diverge along the long path from the keystone to the sample. The laser beams are passed through fiber-coupled beam expanders to reduce the power and allow the beam to completely eclipse the sample. The position of the sample can then be tracked and adjusted using a similar feedback control algorithm as for the BESL (mentioned previously).

Samples are heated via two fiber-coupled diode lasers (980 nm, 110 W continuous maximum power output) denoted (again arbitrarily) as yellow and white (Fig. 2.4). The lasers

aimed at opposite sides of the sample to more evenly heat it, reducing the uncertainty in the temperature measurements. A single Process Sensors Metis MQ22 two-color ratio pyrometer (500-2000 °C) was used to measure the temperature. Although the same correction for temperature measurements mentioned for the WU-BESL is used to correct these temperature measurements, it was noticed that over the longer acquisition times necessary for the neutron diffraction that the temperature would drift. This drift was caused by a shifting of the sample position relative to the pyrometer and could be corrected for by measuring the melt plateau both before and after the isothermal hold.

2.3 Thermophysical Property Characterization

2.3.1 Density and Thermal Expansivity

The density of the liquid samples was measured using the shadow method [10]. The shadow of the sample was cast using the high-intensity amber LED and was recorded using a Pixelink PLB74IG CMOS camera, as shown in Fig.2.2. An edge detection algorithm was used to determine the radius of the sample and, assuming the samples were spherically symmetric, the volume was calculated. Grade 3 tungsten carbide spheres ($3/32 \pm 2 \times 10^{-5}$ inches diameter) were used to calibrate the pixel to volume conversion. The density was then obtained by dividing the calculated volume by the measured mass. By collecting video data during free cooling cycles, where the heating laser is off, density data can be obtained continuously from the high temperature liquid until the sample recalescences (the rise in the sample temperature during crystallization) in the supercooled liquid. The thermal expansivity (or similarly the linear expansivity, $\beta = \alpha/3$) was obtained from

$$\alpha = \frac{1}{V}\frac{\mathrm{d}V}{\mathrm{d}T} \tag{2.2}$$

where V is the sample volume. The details of this procedure and analysis can be found elsewhere [4, 8, 11].

2.3.2 Viscosity

The viscosity was measured using the oscillating drop technique [12, 13], where a sinusoidal perturbing voltage was applied to the top and bottom electrodes. This signal forced oscillations in the sample which, were recorded with a Pixelink PL-B74IG CMOS camera (1500fps). The decay time for the oscillations, once the perturbing signal is removed, is related to the viscosity. More detail can be found elsewhere [4, 8, 11].

2.4 Diffraction Experiments

This section gives details on the diffraction experiments that are presented in this dissertation for both INS and X-ray diffraction. The methods for analysis are also detailed in the corresponding sections.

2.4.1 Inelastic Neutron Scattering Experiments

Analysis and Corrections

The main goal of the INS experiments is to obtain the Van Hove correlation function, $G(r,t)$, which describes the decay of the real space correlations of atoms with time. To do this, the scattering intensity $I(q,E)$ must be related to the dynamic structure factor $S(q,E)$, which is the Fourier transform of $G(r,t)$. The relation between the partial differential cross section, $\frac{\mathrm{d}^2\sigma}{\Omega\omega}$, which is the ideal scattering intensity, and $S(q,E)$ can be derived using Fermi's golden rule and the Fermi pseudo-potential [14–17] giving:

$$\frac{\mathrm{d}^2\sigma}{\mathrm{d}\Omega\mathrm{d}\omega} = Nb^2\frac{k_2}{k_1}S(q,\omega) \tag{2.3}$$

where k_2 is the magnitude of the scattered wave vector, k_1 is the magnitude of the incident wave vector, N is the number of scattering particles, and b is the neutron scattering length. From this relation we can immediately see that a measurement of the scattering intensity, in principal, is a measurement of the Van Hove correlation function.

It still remains to reduce our scattering intensity to the partial differential cross section. A standard reduction is provided by the beamline scientist for ARCS, which effectively converts the measured intensity data to the partial differential cross section. This analysis is done using the MANTID[18] software where an xml file is created to give commands for the reduction process. An example of an xml reduction file is shown in Appendix A. MANTID needs two source beam parameters, the incident energy E_i and the time it takes the peak in the neutron pulse to leave the moderator t_0, which are usually obtained during the experiment. However, since the NESL has an internal beam stop these values must be obtained from the beamline scientist. After the standard MANTID reduction the data is normalized by the proton charge, corrected for detector efficiency, multiplied by k_i/k_f, and converted to the differential cross section.

To convert the obtained partial differential cross section to $S(q, E)$ a normalization factor is needed. One method for doing this is to scan a vanadium sample at the same incident energy, reduce the scattering data to the partial differential cross section, and integrate along the energy to obtain a scale factor. This method can be followed to normalize the data within approximately 30%. Our method is instead to normalize the static structure factor $S(q)$ obtained from

$$S(q) \equiv F(q, 0) = \int S(q, E)\mathrm{d}E \ , \tag{2.4}$$

where $F(q, t)$ is the time Fourier transform of $S(q, E)$, so that $\lim_{q\to\infty} S(q) \to 1$.

Due to the momentum/energy relation for neutrons the range of energy transfer is limited for each momentum transfer value. To obtain enough data to perform the Fourier transforms for $G(r, t)$ then becomes a contest of whether the resolution needs to be high or the region of integration needs to be larger. Figure 2.5 shows the kinematically allowed region for various

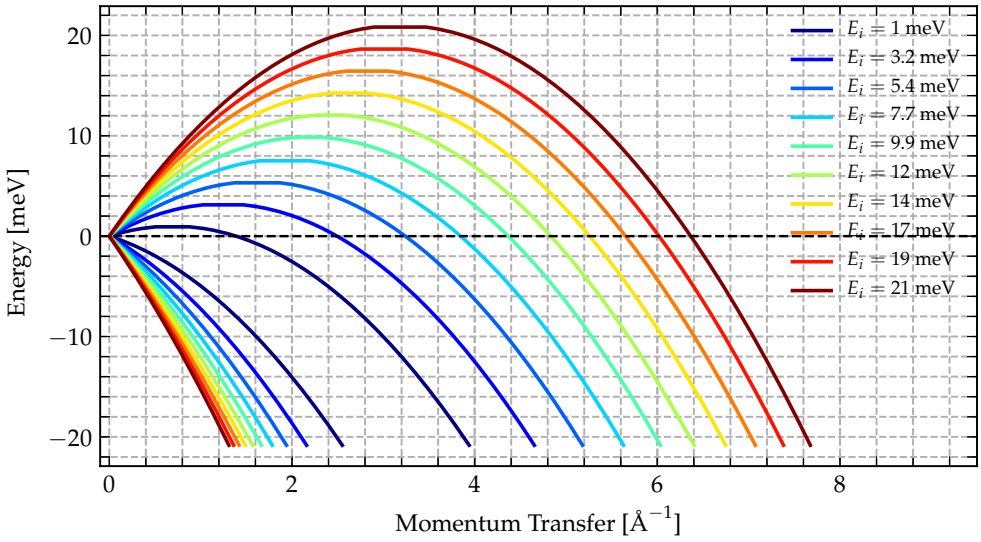

Figure 2.5: The restriction of the q, E-space where points enclosed by the curves are attainable for some choice of scattering angle. This is a result of $k_i^2 \propto E$ where k_i is the magnitude of the incident wave vector and E is the energy.

incident energies that are typical ranges for inelastic and quasielastic scattering studies.

Experiments

The Wide Angular-Range Chopper Spectrometer (ARCS) beamline [19, 20], which is a time-of-flight Fermi chopper spectrometer located at the Spallation Neutron Source (SNS) at Oak Ridge National Laboratory (ORNL), is designed to provide high neutron flux for inelastic neutron scattering (INS) experiments. The incident energy (E_i = 20-1500 meV) of the neutron beam is selected by delaying two upstream Fermi choppers, high speed rotating neutron-absorbing slats, with respect to the neutron pulse. A massive array of ^{3}He linear position sensitive detectors line the sample chamber providing -28-135° of coverage and recording both the energy of the incoming neutron and the time-of-flight. The energy resolution of the INS measurements at the elastic line is $3-5\%$ of the incident energy. A T_0 chopper is designed to block the prompt radiation pulse of neutrons from the target, but by dephasing this chopper with respect to the pulse the spectrometer can be operated in "white beam" mode where the full spectrum of neutrons are available. This mode is used to collect

vanadium scattering data, which is used to correct for detector efficiency.

To obtain the INS data the NESL samples (300-400 mg) are levitated and melted. Several free cooling cycles are done to clean up the sample and give a thermal signature for correcting the pyrometer reading, as mentioned previously. The sample is then heated to the desired temperature and scanned. At 20 meV this takes approximately 2 h, though the amount of time necessary will vary with the incident energy. Scans of the empty chamber scan and of solid vanadium are performed at the same incident energy to remove the chamber profile and perform a normalization to real units, respectively.

The experiments performed for this dissertation at ARCS are summarized in Table 2.1. The first experiment ARCS2015 was the commissioning run for the NESL at the ARCS beamline. The data presented in this dissertation, however, is only from the final scattering experiment ARCS2017. Through the course of these experiments it was determined that a higher energy resolution ($\geq$0.5 meV) was necessary to resolve the first peak in $S(q, E)$ for the analysis in Chapter 6. The remaining data could be used to increase the q, E-range, which would increase the reliability of the Fourier transforms to obtain $G(r, t)$. However, care would need to be taken to better understand the resolution function of the spectrometer. This analysis was performed in the ipython notebook *INS_Analysis.ipynb*, which is discussed in Appendix A.

Experiment	Dates	Samples	Incident Energy meV	Temperature Range K
ARCS2015	2015/10/09 - 2015/10/16	$Cu_{50}Zr_{50}$	50, 80, 120, 150	$-100 \leq \Delta T \leq 150$
ARCS2016	2016/03/08 - 2016/03/15	$Zr_{80}Pt_{20}$	50, 120, 200	$-150 \leq \Delta T \leq 300$
		Vit106	50	$50 \leq \Delta T \leq 150$
		$Zr_{64}Ni_{36}$	50, 120	$-50 \leq \Delta T \leq 200$
ARCS2017	2017/05/02 - 2017/05/09	$Zr_{80}Pt_{20}$	20, 50	$-150 \leq \Delta T \leq 350$
		$Cu_{50}Zr_{50}$	20, 50	$-150 \leq \Delta T \leq 150$

Table 2.1: Summary of inelastic neutron scattering (INS) experiments at the Wide Angular-Range Chopper Spectrometer (ARCS) beamline. $\Delta T = T - T_m$ where T_m is the melting temperature.

2.4.2 Wide Angle X-ray Diffraction Measurements

Analysis and Corrections

To obtain the static structure factor, $S(q)$, and the pair-distribution function, $g(r)$, from the measured diffraction data many standard corrections were required. The analysis of all WAXS data was done using an in-house LabVIEW software written by James Bendert [4, 21] and later modified by Mark Johnson [2]. As mentioned previously, the tilt and position of the detector was determined and corrected for by fitting to the diffraction rings of a levitated polycrystalline silicon standard. The liquid diffraction data exhibit the same isotropic rings, but are more diffuse than the polycrystalline samples(Fig.2.6).

Due to the isotropic and homogenous nature of the studied liquids the diffraction patterns are azimuthally symmetric (Fig. 2.6). To reduce the error in the diffraction measurements an average can be taken over the azimuthal angle, ϕ. The angular averaged intensity is then converted to momentum transfer

$$q = \frac{4\pi \sin(\theta)}{\lambda} \ , \tag{2.5}$$

where λ is the incident X-ray wavelength and θ is the scattered angle.

The measured scattering intensity, I_{raw}, recorded for a sample is corrected for artifacts, dark current, and pixel efficiency using

$$I_{\text{corrected}} = \Gamma \left(I_{\text{raw}} - I_{\text{dark}} - (I_{\text{empty}} - I_{\text{emptydark}}) \right) \tag{2.6}$$

where I_{dark} is the intensity recorded with the secondary shutter closed, I_{empty} is the intensity recorded with no sample in the beam path, $I_{\text{emptydark}}$ is the intensity with no sample and the secondary shutter closed, and Γ is the detector gain map. This corrected intensity is used

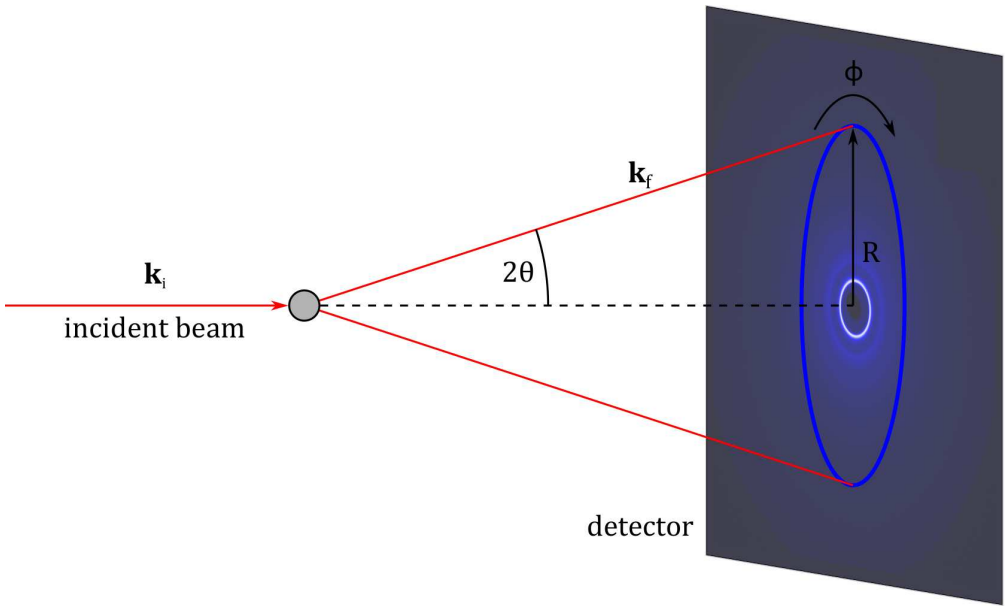

Figure 2.6: Schematic diagram of diffraction in a transmission geometry on an area detector. The data shows an exaggerated scattering angle for clarity and is overlaid on BESL2016 data for $Zr_{80}Pt_{20}$ at 1227 °C.

to obtain the coherent scattering cross section via

$$\frac{\mathrm{d}\sigma_c}{\mathrm{d}\Omega} = N \oint \mathrm{d}\phi \frac{\Gamma\left(\mathrm{d}A/\mathrm{d}\Omega\right) I_{\text{corrected}}}{\left(V'/V\right) OP \left(1 + I_2/I_1\right)} - n^{\text{inc}} - F \tag{2.7}$$

where F is the fluorescence, $\mathrm{d}A/\mathrm{d}\Omega$ accounts for the difference in intensity between detector coordinates and solid angle coordinates, n^{inc} accounts for Compton scattering, V'/V corrects for self-absorption, I_2/I_1 accounts for multiple-scattering, O is oblique incidence, P is the polarization, and N converts from pixel units to electron units. These corrections are discussed in detail elsewhere [2, 4, 22].

For the purpose of this analysis all of these corrections are performed using the in-house analysis software previously mentioned. The structure factor, $S(q)$, is then obtained from the coherent scattering cross section via

$$S(q) = \frac{\frac{\mathrm{d}\sigma}{\mathrm{d}\Omega} + \langle f(q)\rangle^2 - \langle f(q)^2\rangle}{\langle f(q)\rangle^2} \tag{2.8}$$

where $f(q)$ is the atomic form factor and $\langle \ldots \rangle$ denotes an average over the atomic species. The atomic form factors, which are strongly q-dependent, can be calculated from the fitting parameters listed in [23]. After obtaining the static total structure factor the pair distribution function can be obtained by a Fourier transform:

$$g(r) = 1 + \frac{1}{2\pi^2 r \rho_0} \int_0^\infty q(S(q) - 1) \sin(qr) \mathrm{d}q \tag{2.9}$$

Another correction is performed in the calculation of $g(r)$, which removes excess curvature in $S(q)$ and places the data on an absolute scale. This correction is performed using an in-house LabView program written by Mark Johnson and is discussed elsewhere [2].

The following subsections give specific details about the experiments that have been analyzed for and used in this dissertation. Table 2.2 gives a quick summary of important parameters for each BESL experiment that follows. More information on most of these experiments can be found elsewhere [2].

Experiment	Energy [keV]	Beam Size [mm]	Number of Pixels	Pixel Size [µm]	Nominal Working Distance [mm]
BESL2007	129.3	0.7×0.7	1024×1024	400×400	793
BESL2010	129.69	0.7×0.7	1024×1024	400×400	912
BESL2013	129.34	0.7×0.7	2048×2048	200×200	565
BESL2016	131.737	0.7×0.7	2048×2048	200×200	565

Table 2.2: Summary of X-ray diffraction experiment parameters for experiments performed at the Advanced Photon Source (APS) located at Argonne National Laboratory (ANL).

BESL2007

Though denoted as a BESL run, this experiment was actually performed using the NASA/Marshall Space Flight Center ESL. Here samples were processed in a similar manner as described previously with a diode laser in a vacuum chamber (10^{-7} Torr). The temperature was measured with two optical pyrometers with a 0.676 µm (Si) or 1.2-1.4 µm ($\mathrm{In-Ga-As}$) wavelength range. The scattering data was collected using a MAR3450 image plate. For

more information on this experiment see [24].

BESL2010

During August 2010 the WU-BESL was used on station 6-ID-D at the APS for scattering studies on metallic liquids. High energy X-rays (E =129.69 keV, λ =0.095 604 Å) were scattered from the levitated samples in the transmission geometry with a beam size of 0.7 mm × 0.7 mm. Much of the temperature data from this experiment ($\sim$ 43%), however, is contaminated by cross talk from the heating laser and pyrometer, causing a depressed temperature reading while the laser was on and a spike in temperature when the laser was turned off as shown in Fig 2.7. Correcting the temperature data is therefore extremely difficult. If the sample recalesces to the melting temperature (i.e. it does not crystallize to a metastable phase or hypercool) the temperature may be matched to that value and the data could be salvaged. However, it is difficult to know when this is the case *a priori*. It is estimated that this issue affected $\sim$ 43% of the temperature data with the spikes ranging from 5-50 K.

BESL2013

For three weeks in June 2013 the WU-BESL was installed at station 6-ID-D at the APS for scattering studies on metallic liquids and amorphous ribbons. For the liquid samples, the high energy X-ray (E =129.34 keV, λ =0.095 86 Å) beam (size 0.7 mm × 0.7 mm) was scattered from the levitated samples in the transmission geometry. An amorphous Si flat-panel GE Revolution 41-RT detector was used to measure the scattered X-rays with a nominal sampling time of 1-8 Hz. The detector size was set to 2048 pixels × 2048 pixels, where each pixel was 200 µm × 200 µm. The sample-to-detector distance, nominally 565 mm, was regularly calibrated using levitated polycrystalline Si standards and found to be $\sim$551 mm.

Dark measurements were obtained, by closing the secondary shutter, for 5 sec immediately preceding and proceeding the data acquisition from the sample. Between samples an

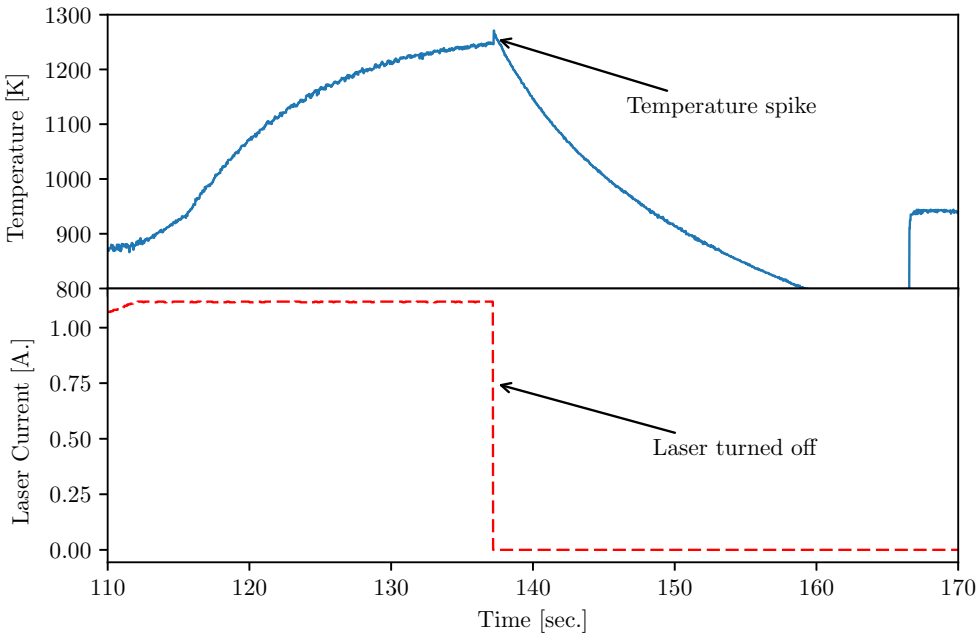

Figure 2.7: An example temperature profile spike that occurs after the heating laser is turned off. This indicates that the laser is feeding into the pyrometer and corrupting the temperature reading.

empty chamber was taken for 20 sec. Each liquid sample was scanned for 10-20 sec for each isothermal hold.

BESL2016

Between 06/13/2016 and 07/05/2016 the WU-BESL was installed at station 6-ID-D at the APS for scattering studies on metallic liquids and bulk cast metallic glasses. The available beamtime for this experiment was divided between three groups from Washington University in Saint Louis, Iowa State University and Seoul National University. The following details represent the conditions during the WASHU portion of the beamtime. High energy X-rays (E =131.737 keV, λ =0.094 114 9 Å) were scattered from the levitated samples in the transmission geometry with a beam size of 0.7 mm × 0.7 mm. An amorphous Si flat-panel GE Revolution 41-RT detector was used to measure the scattered X-rays with a nominal sampling time of 1-2 Hz. The detector size was set to 2048 pixels × 2048 pixels, where each pixel was 200 µm × 200 µm. The sample-to-detector distance, nominally 565 mm, was

regularly calibrated using levitated polycrystalline Si standards and found to be ∼551 mm.

Three sets of data were obtained for each liquid sample: step hold, free cool, and slow cool. For step hold data, the samples were held at a target temperature and scanned for ∼20 s at 1 Hz. The secondary shutter was kept closed for the first 10 s of the scan to provide dark measurements for the sample. For free cool acquisitions the sample was scanned at 2 Hz while cooling with the laser off. Acquisition was continued past recalescence of the sample to obtain crystalline data as well. For slow cool acquisitions the sample was scanned at 1 Hz while cooling was controlled by lowering the laser power incrementally.

Care must be taken when correcting the data from this experiment due to some noticeable artifacts. First the beam stop was slightly misaligned with the incoming beam. While still eliminating most of the signal from the transmitted beam there is an asymmetric increase in intensity. Currently the bad pixel map applied to the image is able to eliminate effects arising from this artifact, which is also at very low q. The other main artifact comes from the misalignment with the tungsten collimator, which produces very faint asymmetric diffraction rings. These rings, though typically occurring near the peak in the structure factor, are able to be mostly subtracted out by the empty chamber correction.

2.5 Simulations and Analysis

Diffraction experiments provide useful, but angular averaged, information about the atomic positions making interpretations about the local topology and atomic dynamics difficult to obtain. Two forms of simulations were performed to obtain a better understanding of the underlying system: classical Molecular Dynamics (MD) and Reverse Monte Carlo (RMC) simulations. Both of these methods will be discussed further in this section.

2.5.1 Classical Molecular Dynamics Simulations

Classical MD simulations generate particle positions and velocities by solving Hamilton's equations of motion. The system Hamiltonian is determined from a semi-empirical interatomic potential, which is typically constructed to reproduce some experimental properties (see [25] for example). It is assumed then that with a reliable semi-empirical potential the microscopic details from the simulated system will reflect the microscopic interactions of the actual system. All MD simulations in this dissertation used Embedded Atom Method (EAM) [26–28] potentials, which approximate many-body effects with an effective charge density. Due to the complexity of the potentials it is not possible to solve Hamilton's equations analytically, so a numerical integrator is needed to determine atomic positions and velocities. The velocity Verlet integrator algorithm [15], which solves Hamilton's equations using a finite difference approach, is used for all simulations in this dissertation. Furthermore, each simulation used isothermal-isobaric ensembles (NPT, $P = 0$) with periodic boundary conditions where the temperature is set to desired values and controlled via the Nosé-Hoover thermostat [29, 30].

All classical Molecular Dynamics (MD) simulations for this dissertation were performed using the Large-scale Atomic/Molecular Massively Parallel Simulator (LAMMPS) [31] software on a high-performance computing cluster located in the physics department at Washington University in St. Louis. Appendix **??** gives a list of the samples simulated for this dissertation. Appendix B gives a short guide with example code for running simulations. The following subsections detail the quantities calculated from the MD simulations.

Calculating Viscosity and Maxwell Time

The viscosity of a simulated liquid can be calculated in several ways (see the LAMMPS manual for examples). Either a non-equilibrium approach is followed, where typically the fluid is intentionally sheared and the velocity is tracked, or an equilibrium approach is used,

which is explained here (this section follows the method outlined by R. Soklaski [32]). In the latter method η is related to the atomic stress tensor through the Green-Kubo [15] formula. This formula is shown below using the extension of this method derived by Daivis and Evans [33], which allows the use of the off-diagonal elements of the stress tensor leading to increased statistics:

$$\eta = \frac{V}{10k_BT}\int \sum_{i,j} \langle P_{ij}(t)P_{ij}(0)\rangle \, \mathrm{d}t \ . \tag{2.10}$$

Here V is the volume, T is the temperature, $\langle \ldots \rangle$ denotes the autocorrelation function (ACF), and P_{ij} is a combination of atomic level stresses given by

$$P_{ij} = \frac{\sigma_{ij} + \sigma_{ji}}{2} - \frac{\delta_{ij}}{3}\sum_k \sigma_{kk} \ , \tag{2.11}$$

where σ_{ij} is the ij-th element of the atomic stress tensor and ij spans all values of the tensor rather than just the off-diagonal elements. The stress tensor is calculated by summing the atomic quantities:

$$\sigma_{ij} = \frac{1}{V}\sum_\alpha \left[m^\alpha \mathbf{v}_i^\alpha \mathbf{v}_j^\alpha + \sum_{\beta>\alpha} \mathbf{F}_i^{\alpha\beta}\left(\mathbf{r}^\alpha - \mathbf{r}^\beta\right)_j \right] \ , \tag{2.12}$$

where m^α is the mass, $\mathbf{v}^\alpha$ is the velocity, $\mathbf{r}^\alpha$ is the position of atom α. $\mathbf{F}_i^{\alpha\beta}$ is the force atom α exerts on atom β in the $i-$th Cartesian coordinate direction. The ACF for P_{ij} was computed using fast Fourier transforms according to the Weiner-Khinchin theorem:

$$\langle P_{ij}(t)P_{ij}(0)\rangle = \mathrm{IFFT}\left[\mathrm{FFT}\left[P_{ij}\right]\mathrm{FFT}\left[P_{ij}\right]^*\right] \ , \tag{2.13}$$

where IFFT and FFT are the inverse and forward fast Fourier transforms and * indicates complex conjugation. The Maxwell time, τ_M, was then computed from the viscosity using $\tau_M = \eta/G_\infty$ where G_∞ is the infinite frequency shear modulus given by

$$G_\infty = \frac{V}{k_bT}\left\langle P_{ij}^2(0)\right\rangle \ . \tag{2.14}$$

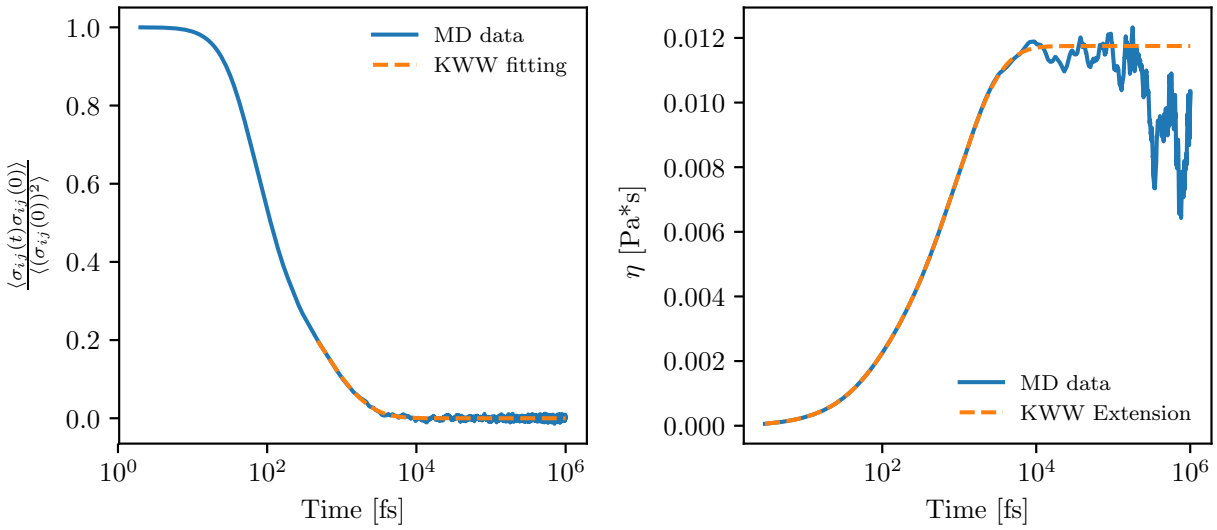

Figure 2.8: The normalized stress ACF (left) as a function of time for $Zr_{80}Pt_{20}$ at 1500 K. The KWW fit function (dashed line) is shown and fit to the region where $\frac{\langle\sigma_{ij}(t)\sigma_{ij}(0)\rangle}{\langle(\sigma_{ij}(0))^2\rangle} < 0.2$. The viscosity (right) obtained from the stress ACF and from replacing the data where $\frac{\langle\sigma_{ij}(t)\sigma_{ij}(0)\rangle}{\langle(\sigma_{ij}(0))^2\rangle} < 0.05$ with the KWW fit values (dashed line) as a function of time.

The time integral in Eq.2.10 is strongly affected by noise [34] in the long time limit, which typically means one must pick a finite time plateau value for the viscosity, making it fairly arbitrary. To better approximate the value of η the long time tail of the normalized stress ACF (where $\frac{\langle\sigma_{ij}(t)\sigma_{ij}(0)\rangle}{\langle(\sigma_{ij}(0))^2\rangle} < 0.2$) is fit with the Kohlrausch-Williams-Watts (KWW) stretched exponential function as previously suggested [35]. This fit value is then used instead of the stress ACF for a smaller region ($\frac{\langle\sigma_{ij}(t)\sigma_{ij}(0)\rangle}{\langle(\sigma_{ij}(0))^2\rangle} < 0.05$) to reduce this noise. This analysis for both the normalized stress ACF and viscosity is shown in Fig. 2.8.

The viscosity data in Chapter 6 and Chapter 4 (not shown) is calculated using this method. The analysis was done in the Jupyter notebooks *Viscosity_Computation.ipynb* and *Viscosity_Plotting_PostProcessing.ipynb* that were written and maintained by Robert Ashcraft.

Calculating Static and Dynamic Pair Correlation Functions

The distinct, $G_d(r,t)$, and self, $G_s(r,t)$, Van Hove correlation functions are calculated from

$$G_s(r,t) = \frac{1}{N}\left\langle \sum_{i=1}^{N} \delta(\mathbf{r} - \mathbf{r}_i(t) + \mathbf{r}_i(0)) \right\rangle \tag{2.15}$$

$$G_d(r,t) = \frac{1}{N}\left\langle \sum_{i=1}^{N}\sum_{i\neq j}^{N} \delta(\mathbf{r} - \mathbf{r}_i(t) + \mathbf{r}_j(0) \right\rangle \tag{2.16}$$

where $\mathbf{r}_i(t)$ is the position of atom i at time t. A schematic representation of the calculation of $G_d(r,t)$ and $G_s(r,t)$ and the resulting curves are shown in Fig. 2.9. Only atoms that are within a cutoff of half the box length were used. To increase statistics a moving windowed average over 1000 to 10000 configurations and window size of 1000 to 2000 was used. $G_d(r,t)$ and $G_s(r,t)$ were calculated between each distinct atomic type using a parallel python script on the physics department high-performance computing cluster. Due to the larger computational requirement for the dynamic pair correlations the number of configurations averaged over is smaller than for the static pair correlation function ($\sim$ 20000 configurations). However, comparing the $t = 0$ dynamic value to the static function still gives good agreement.

2.5.2 Reverse Monte Carlo Simulations

The Reverse Monte Carlo [36] (RMC) method is one of several techniques used to determine the 3D atomic structure from 1D diffraction data. In this method an initial configuration of atoms is generated and atom positions are adjusted until agreement with the input constraint data is reached. The input constraint data typically consists of one or more TSFs, PSFs, TPCFs, PPCFs, Extended X-ray Absorption Fine Structure (EXAFS) measurements or even traditional MD simulations [37, 38]. The χ^2 is calculated to measure the agreement

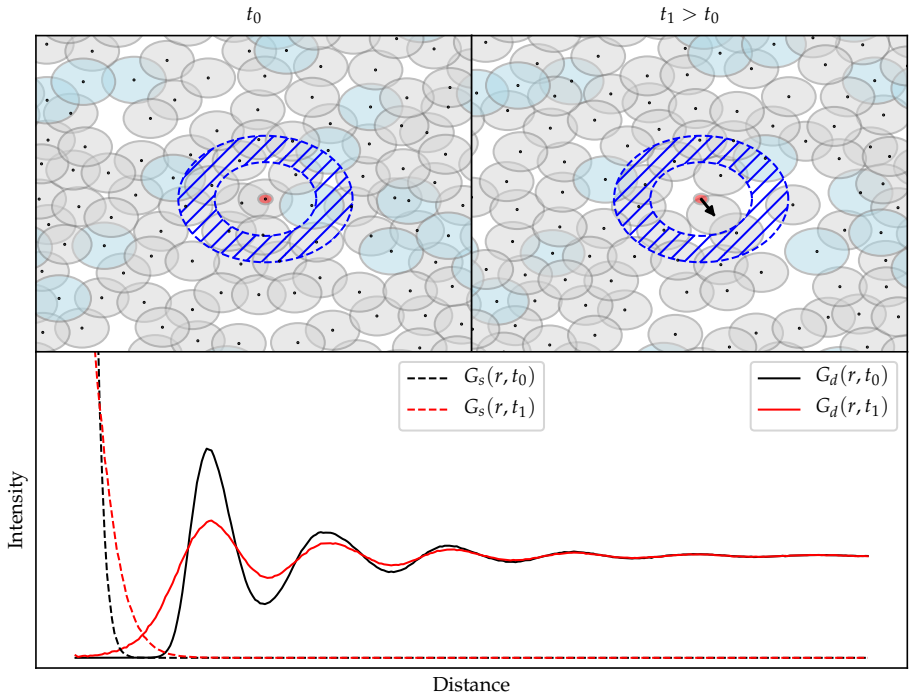

Figure 2.9: A schematic diagram of the calculation of the distinct, $G_d(r,t)$, and self, $G_s(r,t)$, Van Hove correlation functions at two times t_0 and t_1 ($t_1 > t_0$) for a liquid with two atomic types represented by the shaded hard sphere radius region around each atom. The atom enclosed in the small red region is the central atom for the calculations. The blue hatched region shows a distance that would be used for the pair, distinct, distance calculations. The arrow indicates the motion of the central atom between t_0 and t_1. The lower figure shows the self (dashed) and the distinct (solid) correlation functions for the two times t_0(black) and t_1 (red).

between the constraints and the atomic configuration. This is given by

$$\chi_i^2 = \sum_k \frac{\left(X_i'(k) - X_i^0(k)\right)^2}{\sigma_i^2(k)} \,, \tag{2.17}$$

where $X_i^0(k)$ represents the i-th constraint at location k (in general either momentum transfer or position), $X_i'(k)$ is the RMC calculated value corresponding to the i-th constraint, and $\sigma_i^2(k)$ is the reliability of the i-th constraint at location k. To minimize the χ^2 a random atom is moved, according to some user defined distance cutoff, in a random direction. The χ^2 is then computed for this new configuration,χ^2_{New} , and compared to the χ^2 for the old configuration, χ^2_{Old}. If $\chi^2_{\text{New}} < \chi^2_{\text{Old}}$ the move is accepted. If $\chi^2_{\text{New}} > \chi^2_{\text{Old}}$ the move is accepted with a Boltzmann probability. Given enough time the atomic configuration will converge to a structure consistent with all input constraints.

The number of constraints input into an RMC simulation will determine the reliability of the output atomic configuration. For instance to fully describe a system with n elements $n(n+1)$ constraints are needed to obtain elementally resolved information. In general fewer constraints used in an RMC simulation will give less reliable configurations. The reliability of minimally constrained reverse Monte Carlo (mcRMC) simulations, where only the TPCF is used, is discussed in Chapter 3.

The RMCs in Chapters 3 and 4 were performed using the RMC++ [39] software. Atoms were randomly generated using a python script *Random.py* written and maintained by Robert Ashcraft. The number density was used to determine the size of the simulation cell. Each simulation was run in parallel for a total of approximately 30-120 computational hours. Minimum elemental cutoff distances, which are approximated from the low-r side of $g(r)$, and swapping of elements (typically 10% of the generated moves) was used to decrease the convergence time. The convergence of a simulation is assumed when both the χ^2 and its change with time are suitably small, as shown in Fig. 2.10. Since RMC simulations are not unique, as many configurations can generate indistinguishable structure factors. Multiple

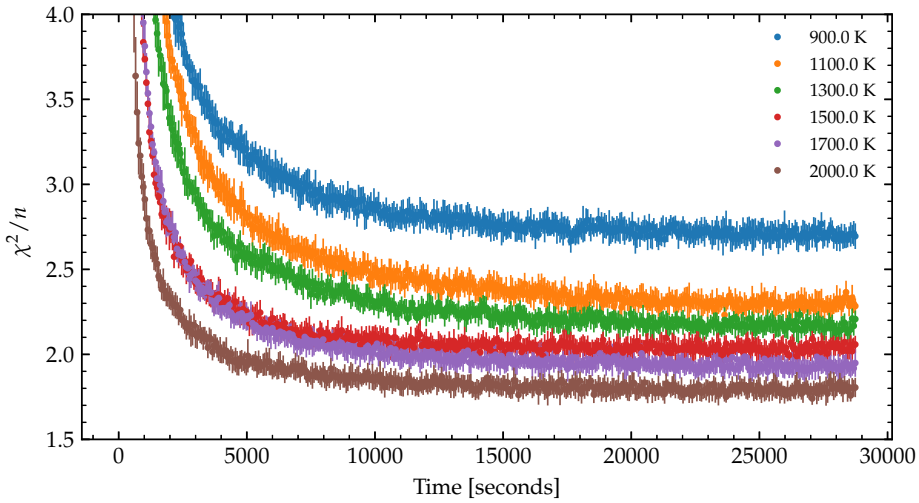

Figure 2.10: Example plot of the χ^2 divided by the number of data points, n, from RMC for MD simulated $Cu_{50}Zr_{45}Al_5$ liquid. Error bars are calculated from averaging over the different RMC simulations.

simulations were therefore run for each composition to generate statistical ensembles. An example input file for an RMC simulation is given in Appendix C. A list of all the systems that have been simulated using RMC for this dissertation can be found in Appendix **??**.

2.5.3 Voronoi Analysis

Voronoi tessellation analysis [40] is a method of characterizing the local topography around an atom by enclosing each atom in a three-dimensional polyhedron. An atoms Voronoi Polyhedron (VP) is constructed by extending line segments from this atom to all the surrounding atoms within some cutoff distance, which is typically larger than the next-nearest-neighbor distance. Normal bisecting planes are placed equidistant from each atom and extended in space. The intersection of all these planes then forms the central atom's VP. This is the same procedure used in crystalline systems to obtain the Wigner-Seitz cell [41]. Due to the difficulty in visualizing a three-dimensional Voronoi tessellation a two-dimensional case is shown in Fig. 2.11.

For dense systems with atoms of differing sizes the above procedure can cause the bisecting plane to intersect the larger atom rather than being placed between the atoms [42]

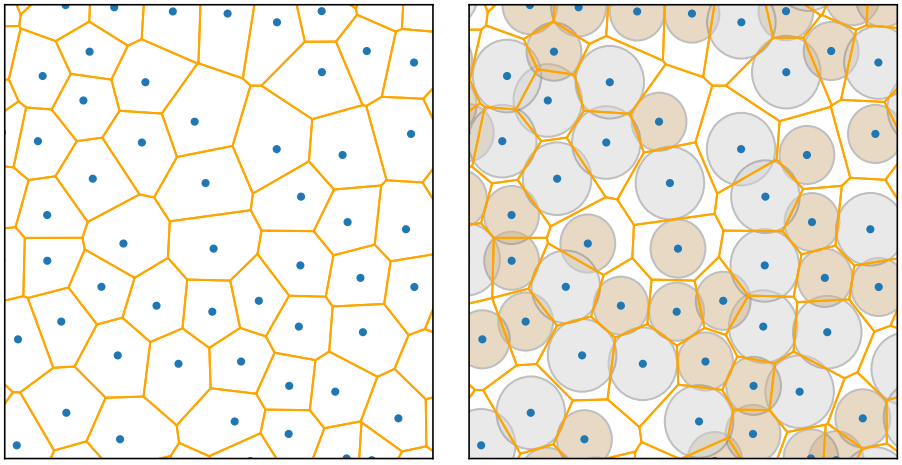

Figure 2.11: (Left) An example Voronoi tessellation. Each blue point represents an atom while the orange lines are the associated Voronoi polygon. (Right) The sample Voronoi tessellation with the atomic radii shown as well.

(Fig. 2.11). To fix this common error radical Voronoi tessellation [43, 44] was developed in which the placement of the bisecting plane is weighted by the size of each atom. This forces the bisecting plane farther from the larger atom but the tessellation is no longer guaranteed to fill the space.

The VP produced from this procedure can be described via the Voronoi Index (VI) which is a list of the number of faces with a given number of edges typically of the form $\langle n_3 n_4 \dots n_i \dots \rangle$ where n_i is the number of faces with i number of edges. Since Voronoi tessellation characterizes the entire space many other interesting quantities can be computed from the procedure, such as the polyhedron volume (V), the surface area (SA), asphericity ($S^3/(36\pi V^2)$), coordination number, and nearest-neighbor distance.

In this dissertation, the python library pyvoro which is a python entry point to the Voro++ library was used to perform the Voronoi tessellations on both RMC and MD atomic configurations in Chapters 3 and 4. To perform the radical Voronoi tessellation the elemental Goldschmitt radii [45] were used. Custom python code was developed to process the tessellated data to remove small faces as discussed in Chapter 4.

2.6 References

[1] M. E. Blodgett. Thermophysical Properties and Structural Evolution of Supercooled Metallic Liquids. PhD thesis. Washington University in St. Louis, 2015.

[2] M. Johnson. Structural Evolution, Chemical Order, and Crystallization of Metallic Liquids and Glasses. PhD thesis. Washington University in St. Louis, 2015. DOI: 10.7936/K79W0CRD.

[3] W.-k. Rhim et al. An electrostatic levitator for high-temperature containerless materials processing 1-g. *Review of Scientific Instruments* **64**,10 (1993).

[4] J. C. Bendert. Thermophysical and Structural Measurements of Liquid Metallic Alloys Using Electrostatic Levitation. PhD thesis. Washington University in St. Louis, 2013.

[5] N. A. Mauro. Structural and Thermophysical Property Studies of Metallic Liquids and Glasses using the Beamline Electrostatic Levitation Technique. PhD thesis. Washington University in St. Louis, 2011.

[6] T. Meister et al. Gain-scheduled control of an electrostatic levitator. *Control Engineering Practice* **11**,2 (2003). DOI: 10.1016/S0967-0661(02)00102-8.

[7] J. C. Bendert et al. Temperature Calibration for Optical Pyrometry in Containerless Systems Using Differential Scanning Calorimetry: Application to $Cu_{100-x}Zr_x$ $x = 45 - 50$). *International Journal of Thermophysics* **35**,9-10 (2014). DOI: 10.1007/s10765-014-1660-y.

[8] C. E. Pueblo. Ground and Flight Based Studies of Nucleation and Thermophysical Properties in Metallic Glass Forming Systems. PhD thesis. Washington University in St. Louis, 2016. DOI: 10.7936/K7PN942Z.

[9] N. A. Mauro et al. Electrostatic levitation facility optimized for neutron diffraction studies of high temperature liquids at a spallation neutron source. *Review of Scientific Instruments* **87**,1 (2016). DOI: 10.1063/1.4939194.

[10] S. K. Chung, D. B. Thiessen, and W.-K. Rhim. A noncontact measurement technique for the density and thermal expansion coefficient of solid and liquid materials. *Review of Scientific Instruments* **67**,9 (1996). DOI: 10.1063/1.1147584.

[11] J. C. Bendert and K. F. Kelton. Containerless Measurements of Density and Viscosity for a Cu $$_{48}$$ 48 Zr $$_{52}$$ 52 Liquid. *International Journal of Thermophysics* **35**,9-10 (2014). DOI: 10.1007/s10765-014-1664-7.

[12] W.-K. Rhim et al. Noncontact technique for measuring surface tension and viscosity of molten materials using high temperature electrostatic levitation. *Review of Scientific Instruments* **70**,6 (1999). DOI: 10.1063/1.1149797.

[13] A. K. Gangopadhyay et al. Correlation of the fragility of metallic liquids with the high temperature structure, volume, and cohesive energy. *Journal of Chemical Physics* **146**,15 (2017). DOI: 10.1063/1.4981011.

[14] L. Van Hove. Correlations in space and time and born approximation scattering in systems of interacting particles. *Physical Review* **95**,1 (1954). DOI: 10.1103/PhysRev.95.249.

[15] J.-P. Hansen and I. R. McDonald. *Theory of Simple Liquids: with Applications to Soft Matter*. Fourth. Amsterdam: Elsevier/AP, 2013.

[16] N. H. March and M. P. Tosi. *Atomic Dynamis in Liquids*. New York: Halsted Press, 1976.

[17] W. Marshall and S. W. Lovesey. *Theory of thermal neutron scattering: the use of neutrons for the investigation of condensed matter*. Oxford: Clarendon Press, 1971.

[18] O. Arnold et al. Mantid - Data analysis and visualization package for neutron scattering and μ SR experiments. *Nuclear Instruments and Methods in Physics Research, Section A: Accelerators, Spectrometers, Detectors and Associated Equipment* **764**, (2014). DOI: 10.1016/j.nima.2014.07.029. arXiv: 1407.5860.

[19] D. L. Abernathy. ARCS: a wide Angular-Range Chopper Spectrometer at the SNS. *Notiziario Neutroni E Luce di Sincrotrone* **13**,1 (2008).

[20] D. L. Abernathy et al. Design and operation of the wide angular-range chopper spectrometer ARCS at the Spallation Neutron Source. *Review of Scientific Instruments* **83**,1 (2012). DOI: 10.1063/1.3680104.

[21] J. C. Bendert, N. A. Mauro, and K. F. Kelton. Pair distribution function analysis of X-ray diffraction from amorphous spheres in an asymmetric transmission geometry: Application to a Zr 58.5Cu15.6Ni12.8Al10.3Nb 2.8 glass. *Journal of Applied Crystallography* **46**,4 (2013). DOI: 10.1107/S0021889813013162.

[22] T. Egami and S. J. L. Billinge. *Underneath the Bragg Peaks*. Vol. 6. 2003, p. 57. DOI: 10.1016/S1369-7021(03)00635-7.

[23] D. Waasmaier and A. Kirfel. New Analystical Scattering-Factor Functions for Free Atoms and Ions. *Acta Crystallographica Section A* **51**,3 (1995). DOI: 10.1107/S0108767394013292.

[24] K. F. Kelton et al. A case for local icosahedral order in undercooled metallic liquids and the influence on the nucleation barrier. *Journal of Non-Crystalline Solids* **352**,50-51 (2006). DOI: 10.1016/j.jnoncrysol.2006.08.009.

[25] M. I. Mendelev et al. Development of interatomic potentials appropriate for simulation of liquid and glass properties of nizr2 alloy. *Philosophical Magazine* **92**,35 (2012). DOI: 10.1080/14786435.2012.712220.

[26] M. S. Daw and M. I. Baskes. Embedded-atom method: Derivation and application to impurities, surfaces, and other defects in metals. *Physical Review B* **29**,12 (1984). DOI: 10.1103/PhysRevB.29.6443.

[27] M. S. Daw and M. I. Baskes. Semiempirical, quantum mechanical calculation of hydrogen embrittlement in metals. *Physical Review Letters* **50**,17 (1983). DOI: 10.1103/PhysRevLett.50.1285.

[28] Y. Q. Cheng and E. Ma. Atomic-level structure and structure-property relationship in metallic glasses. *Progress in Materials Science* **56**,December 2010 (2011). DOI: 10.1016/j.pmatsci.2010.12.002.

[29] S. Nosé. A unified formulation of the constant temperature molecular dynamics methods. *The Journal of Chemical Physics* **81**,1 (1984). DOI: 10.1063/1.447334.

[30] W. G. Hoover. Canonical dynamics: Equilibrium phase-space distributions. *Physical Review A* **31**,3 (1985). DOI: 10.1103/PhysRevA.31.1695.

[31] S. Plimpton. Fast Parallel Algorithms for Short-Range Molecular Dynamics. *Journal of Computational Physics* **117**,1 (1995). DOI: 10.1006/jcph.1995.1039. arXiv: nag.2347 [10.1002].

[32] R. Soklaski. A Molecular Dynamics Study of the Structure-Dynamics Relationships of Supercooled Liquids and Glasses. PhD thesis. Washington University in St. Louis, 2015. DOI: 10.7936/K7V69GSK.

[33] P. J. Daivis and D. J. Evans. Comparison of constant pressure and constant volume nonequilibrium simulations of sheared model decane. *The Journal of Chemical Physics* **100**,1 (1994). DOI: 10.1063/1.466970.

[34] Y. Zhang, A. Otani, and E. J. Maginn. Reliable Viscosity Calculation from Equilibrium Molecular Dynamics Simulations: A Time Decomposition Method. *Journal of Chemical Theory and Computation* **11**,8 (2015). DOI: 10.1021/acs.jctc.5b00351.

[35] G.-J. GUO et al. Viscosity and stress autocorrelation function in supercooled water: a molecular dynamics study. *Molecular Physics* **100**,16 (2002). DOI: 10.1080/00268970210133477.

[36] R. L. McGreevy and L. Pusztai. Reverse Monte Carlo Simulation: A New Technique for the Determination of Disordered Structures. *Molecular Simulation* **1**,6 (1988). DOI: 10.1080/08927028808080958.

[37] R. L. McGreevy. Reverse Monte Carlo modelling. *Journal of Physics: Condensed Matter* **13**,46 (2001). DOI: 10.1088/0953-8984/13/46/201.

[38] O. Gereben et al. A new version of the RMC++ Reverse Monte Carlo programme, aimed at investigating the structure of covalent glasses. *Journal of Optoelectronics and Advanced Materials* **9**,10 (2007).

[39] O. Gereben, L. Pusztai, and R. L. McGreevy. Development of the time-dependent reverse Monte Carlo simulation, RMCt. *Journal of physics. Condensed matter* **19**,33 (2007). DOI: 10.1088/0953-8984/19/33/335223.

[40] G. Voronoi. Nouvelles applications des paramètres continus à la théorie des formes quadratiques. Deuxième mémoire. Recherches sur les parallélloèdres primitifs. *Journal für die reine und angewandte Mathematik (Crelle's Journal)* **1908**,134 (1908). DOI: 10.1515/crll.1908.134.198.

[41] N. W. Ashcroft and N. Mermin. *Solid State Physics*. 1976.

[42] J. Park and Y. Shibutani. Common errors of applying the Voronoi tessellation technique to metallic glasses. *Intermetallics* **23**, (2012). DOI: 10.1016/j.intermet.2011.12.019.

[43] B. J. Gellatly and J. L. Finney. Calculation of protein volumes: An alternative to the Voronoi procedure. *Journal of Molecular Biology* **161**,2 (1982). DOI: 10.1016/0022-2836(82)90155-3.

[44] M. Gerstein, J. Tsai, and M. Levitt. The volume of atoms on the protein surface: Calculated from simulation, using Voronoi polyhedra. *Journal of Molecular Biology* **249**,5 (1995). DOI: 10.1006/jmbi.1995.0351.

[45] W. F. Gale and T. C. Totemeier, eds. *Smithells Metals Reference Book*. 8th. Oxford: Butterworth-Heinemann, 2004.

Chapter 3: Assessing the Reliability of Minimally Constrained Reverse Monte Carlo Simulations for Model Metallic Liquids

This chapter has been published on the arXiv [1] in collaboration with K. F. Kelton and is awaiting submission to a peer-reviewed journal. It has been adapted to be consistent with the formatting in this dissertation. The author's contributions include performing the Molecular Dynamics (MD) and Reverse Monte Carlo (RMC) simulations, analyzing the resulting data, and writing the manuscript. All authors contributed in drafting the results.

3.1 Introduction

The Reverse Monte Carlo (RMC) method [2, 3] is a common technique used to obtain 3D atomic structures for liquids and glasses using data obtained from X-ray diffraction or neutron scattering measurements. In this method, atom positions in an atomic ensemble are adjusted using a Monte Carlo algorithm to give the best match to the total structure factor (TSF) or total pair correlation function (TPCF) derived from the scattering data. For an alloy containing n elements, the typical number of structural constraints necessary is $n(n+1)/2$. In practice, however, it is generally difficult to experimentally measure these, particularly for samples containing more than two elements. Instead the information is frequently obtained from *ab. initio* [4] or molecular dynamics (MD) simulations and is typically in the form of partial pair correlation functions (PPCFs) [5]. Attempts have also been made for a combined procedure, simulating the system using MD then performing RMC with experimental data, or incorporating the interatomic potential functions in the RMC

code [6]. Often, however, RMC fits are made to only the TSF or TPCF. These fits will give the most random structure consistent with the experimental scattering data and will lack elementally resolved information. The validity of this approach is therefore questionable.

Previous studies have examined the reliability of the RMC method for MD-generated structures for elemental [7, 8] and binary [9–11] systems, typically constraining the fit with all the measured PPCFs. The results of these studies typically suggest that the RMC method can accurately recreate the atomic structure of the system. This is based on an examination of the RMC structure using metrics including Voronoi tessellation [12, 13](the most common), bond angle distribution [14], and Honeycutt-Anderson analysis[15]. However, in at least one study it is found that the RMC generated structure can be considerably more disordered than the MD-generate one.

Here, the case most often used for the analysis of experimental data will be considered, i.e. where the RMC is constrained with only the TPCF, termed hear as a minimally constrained reverse Monte Carlo (mcRMC) simulation. The reliability of the atomic structures generated by these mcRMC simulations and how that reliability depends on the temperature and the number of elements are examined. To examine the latter, three systems (Zr, $Cu_{50}Zr_{50}$, and $Cu_{50}Zr_{45}Al_5$) are simulated at several temperatures using classical MD. The TPCF is calculated from each simulation and used as input to mcRMC simulations. The atomic configurations from both the mcRMC and MD simulations are then compared using Voronoi tessellation.

3.2 Simulations and Analysis Methods

3.2.1 Molecular Dynamics Simulations

The TPCFs were obtained from MD simulations using the LAMMPS [16] software employing embedded atom method [14] (EAM) potentials for Zr [17], $Cu_{50}Zr_{50}$ [18], and $Cu_{50}Zr_{45}Al_5$ [19]. All compositions were simulated with 15,000 atoms under the NPT

($P = 0$) ensemble with periodic boundary conditions. The Nosé -Hoover thermostat [20, 21] was used to equilibrate each system at each target temperature before data collection. The atomic configuration for each system was randomly initialized and evolved in the high temperature liquid before cooling ($3 - 8 \times 10^9$K/s) to each target temperature. To reach equilibrium the system was evolved for $5 - 15$ns.(3,000,000 MD time steps), depending on the values of the temperature and composition. Each PPCF, $g_{\alpha\beta}(r)$, was then calculated by averaging over 15,000 snapshots of the system using (see [14])

$$g_{\alpha\beta}(r) = \frac{N}{4\pi r^2 \rho N_\alpha N_\beta} \sum_{i,j=1}^{N_\alpha, N_\beta} \delta(r - |\vec{r}_{ij}|) \tag{3.1}$$

where N is the number of atoms, ρ is the number density, $\vec{r_{ij}}$ is the distance from atom i to atom j, and N_α and N_β are the number of α and β atoms, respectively. The TPCF was calculated within the Faber-Ziman [22] formalism

$$g(r) = \sum_\alpha \sum_\beta \frac{c_\alpha c_\beta b_\alpha b_\beta}{\langle b \rangle^2} g_{\alpha\beta}(r) \tag{3.2}$$

where c_α is the atomic concentration and b_α is the neutron scattering length for element α and $g_{\alpha\beta}$ is the PPCF between elements α and β. While the case of neutron scattering is assumed for the analysis presented here, the approach could be directly extended to X-ray scattering if q-dependent atomic scattering factors were used

The viscosity of each liquid was calculated using the Green-Kubo formula [23]. The viscosity exhibits a crossover from near-Arrhenius to super-Arrhenius temperature behavior at the temperature T_A. Since it is difficult to calculate the melting temperature from MD simulations, T_A was used as the scaling temperature, because it is readily computed

3.2.2 Reverse Monte Carlo Simulations

As discussed, minimally constrained reverse Monte Carlo simulations are carried out by taking an input configuration of atoms and input TPCF, changing the input configuration

by randomly moving an atom in a random direction and then computing the mcRMC values of the TPCF for this new configuration. This is then compared with the MD-generated TPCF using the χ^2 as a measure of the goodness of fit,

$$\chi^2 = \sum_i \frac{\left[g^{\mathrm{RMC}}(r_i) - g(r_i)\right]^2}{\sigma^2} \tag{3.3}$$

σ is the reliability of the data set. The random move is accepted if the χ^2 is reduced and is accepted with a Boltzmann probability if the χ^2 is increased. This procedure is repeated until the χ^2 is minimized.

The mcRMC simulations were run using the RMC++ [24] software. Each mcRMC simulation started with a random configuration of 10,000 atoms confined to a cubic box with periodic boundary conditions, with the box dimensions consistent with the number density predicted from the MD results. The Hard-sphere cutoff distances were determined from the value of r where each respective PPCF trended to 0 on the low-r side of the main peak. Ten separate simulations were run at each temperature to generate more reliable distributions from the Voronoi tessellation. Each simulation was run in parallel for 30-45 computational hours depending on the resulting χ^2. Convergence of the mcRMC was assumed when both the value and the change with time of the χ^2 was suitably small ($\chi^2 < 10$).

3.2.3 Voronoi Tessellation

The Voronoi tessellation divides the atomic configuration into Voronoi polyhedral (VP) cells, each consisting of a central atom and the space closer to this atom than any other. The VP is constructed as the collection of perpendicular bisecting planes between the central atom and all neighboring atoms; the planes form the faces of the VP. It has been shown [25] that for atoms of different radii the standard Voronoi tessellation technique can lead to significant errors. The radical Voronoi tessellation [26, 27] was therefore used for the $Cu_{50}Zr_{50}$ and $Cu_{50}Zr_{45}Al_5$ simulations. This technique weights the placement of the bisecting planes by the

radii of the central and neighbor atoms. Another potential error that is common in Voronoi tessellation is the occurrence of exceptionally small faces and edges, which arise from more distant atoms [28]. The effect of removing these faces and edges is not currently investigated but may lead to broader distributions for nearest-neighbor distance and coordination number in both the MD and mcRMC.

The Voronoi tessellation was carried out using a Python extension of the VORO++[29, 30] code. The Goldschmidt radii [31] were used for the radical Voronoi tessellation. The VP can be described by the Voronoi index (VI), $\langle n_3, n_4, n_5, \ldots \rangle$, where n_i is the number of i-edged faces. Both the geometric coordination number (CN), number of faces, and the nearest-neighbor distance (NND), distance between atoms that share faces, were calculated. Finally, the volume and surface area of each VP were used to calculate the asphericity parameter, $\alpha = S^3/(36\pi V^2)$, which gives a measure of how similar the VP is to a sphere ($\alpha = 1$) or a given regular polyhedron ($\alpha = 1.32503$ for a regular dodecahedron).

3.2.4 L^1 Histogram Distance

The L^1, or Taxicab/Manhattan, distance was used to compare the similarity of the distributions obtained from the Voronoi tessellation. Other metrics such as the Bhattacharyya[32] or Hellinger [33] distance give similar but systematically larger results. The L^1 distance is given by

$$L^1(\mathbf{X}, \mathbf{Y}) = \frac{1}{2} \sum_i^n |x_i - y_i| \tag{3.4}$$

where $\mathbf{X}$ and $\mathbf{Y}$ are probability vectors (i.e. $\sum x_i = 1$) and the factor of $1/2$ is included for normalization. By definition it is easy to see $L^1 = 0$ for identical distributions and $L^1 = 1$ for distributions that have no overlap. This metric, therefore, gives a unique measure on the reliability of RMC to reproduce distributions from the MD atomic structure.

3.3 Results and Discussions

The mcRMC fits (averaged over ten simulations) are compared in Fig 3.1 with the MD TPCFs for representative temperatures of each composition. The fits are extremely good, indicating that the generated structures should be a good approximations to the atomic configurations in the MD data. However, as mentioned, chemical ordering was not be reproduced well for both $Cu_{50}Zr_{50}$ and $Cu_{50}Zr_{45}Al_5$ because only a single constraint was used. Only examples at intermediate temperatures are shown since the χ^2 for each composition appears to be temperature dependent. This is likely due to the random nature of the RMC algorithm; the RMC algorithm gives the most disordered configuration consistent with the input constraints. Since the high temperature data are inherently more disordered they are easier to fit than the lower temperature data resulting in a lower χ^2, although the variation in the χ^2 with temperature is relatively small.

The L^1 distances for each of the previously discussed parameters obtained from the Voronoi tessellation procedure are shown in Fig. 3.2. These each give in a general sense a property of the VP associated with the tessellation. By comparing their values between RMC and MD, they can give an indication of reliability. The Voronoi volume gives the general size of the space that is allocated to each atom. The asphericity gives information about the general distribution of atoms about the central atom by considering its size. Both the coordination number and Voronoi index give similar information about the distribution, but irrespective of geometric size and with varying degrees of sensitivity. Lastly, the nearest-neighbor distance gives information on the distance between the polyhedra.

3.3.1 Volume

The Voronoi volume is arguably one of the most easily reproducible properties considered here since it is determined by the input number density, simulation volume, and hard sphere radii. However, because the mcRMC simulation is constrained solely with the TPCF it is

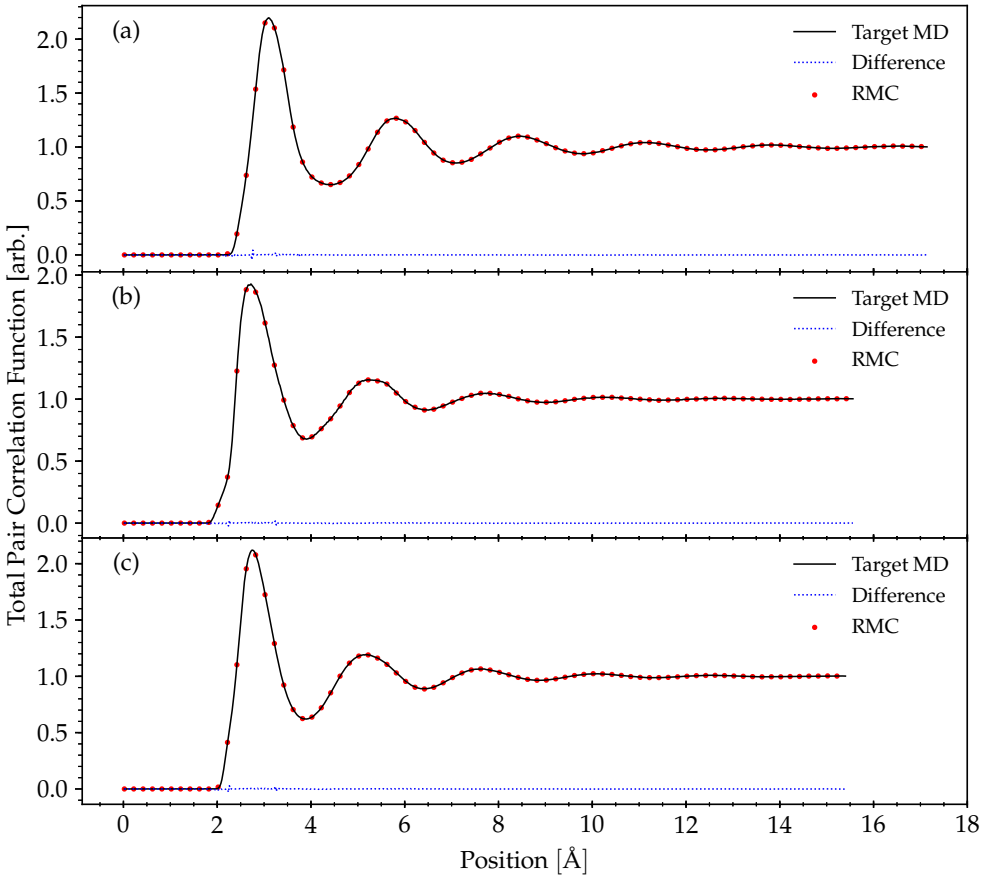

Figure 3.1: Representative plots of the RMC fit (circles) to MD data (line) for (a) Zr , (b) $Cu_{50}Zr_{50}$, and (c) $Cu_{50}Zr_{45}Al_5$ at 2500, 2000 and 1500K, respectively. The difference curve (dashed line) for each data set is also included to emphasize the level of agreement.

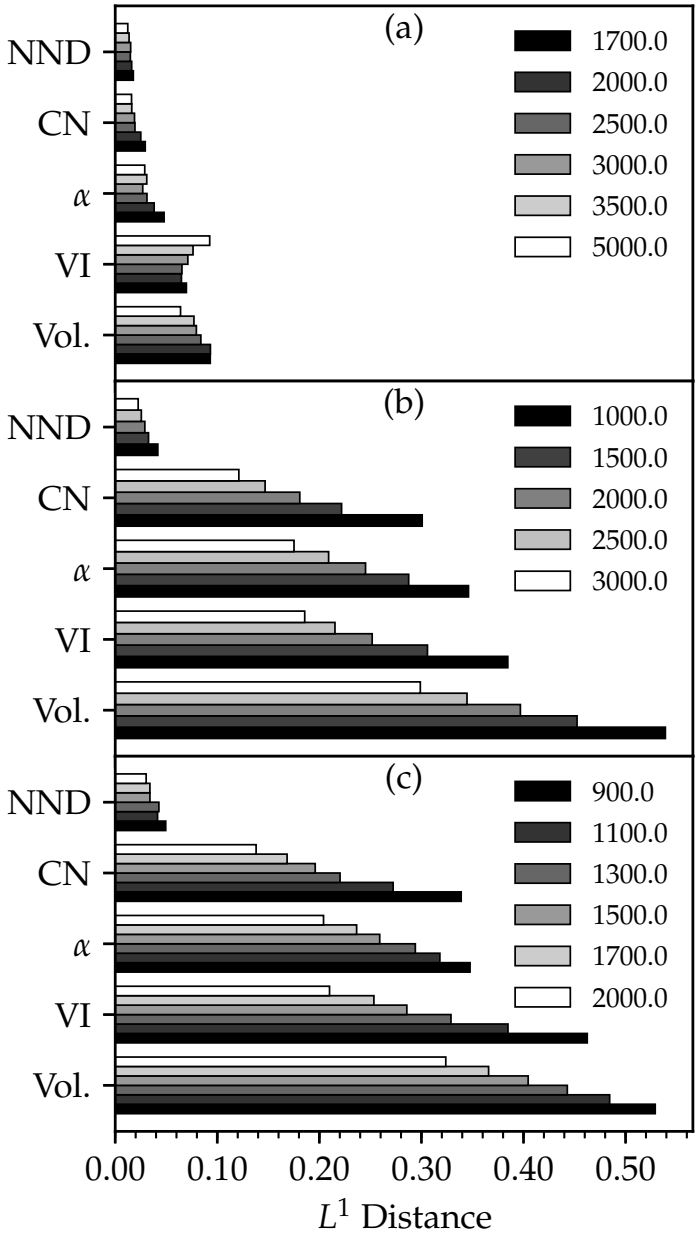

Figure 3.2: L^1 (Manhattan) distance between mcRMC and MD distributions of nearest neighbor distance (NND), coordination number(CN), asphericity parameter (ASPH), Voronoi index (VI), and volume (VOL) for (a) Zr,(b) $Cu_{50}Zr_{50}$, and (c) $Cu_{50}Zr_{45}Al_5$. The darkness of the shading indicates the temperature $[K]$ where black is low and white is high. The L^1 distance is normalized between 0 and 1 where 0 indicates two identical distributions and 1 indicates no overlap in the distributions.

unable to accurately allocate the proper volume to each element. This is shown in Fig 3.3, where the Voronoi volume distribution is shown for each composition and temperature. While the Zr liquid is reproduced well the alloy liquids are not. The $Cu_{50}Zr_{50}$ and $Cu_{50}Zr_{45}Al_5$ liquids have two and three peaks, respectively, one for each element. These peaks are distinct in the structure obtained from the MD but are broadened and overlapping for the mcRMC structure. This difference, which is directly related to the use of only the TPCF constraint, is the cause of the large L^1 distance observed in Fig. 3.2 and the unreliability of the Voronoi volume in minimally constrained systems. However, if the Voronoi tessellation fills space the average Voronoi volume should be the reciprocal of the number density indicating that the average volume should still be a reliable parameter, as shown in Fig. 3.4. While the details of the atomic distribution might be unreliable the average properties of the distribution could still be useful.

3.3.2 Asphericity

Asphericity has been used to examine the shape of the VP in liquid water, where it was noted that the volume is not correlated with α and that it approaches the value of ice upon cooling the liquid [34]. In a similar fashion asphericity is used here to see how the shape of the VPs change with cooling and how well the mcRMC recreates the shape of the VPs. As shown in Fig. 3.5 for $Cu_{50}Zr_{50}$ there are two distinct peaks in the MD (a) compared to the mcRMC (b). This is a consequence of failing to resolve the elemental differences, since the two elements have significantly different distributions, and results in the relatively large L^1 distance (Fig. 3.2). Only the data for $Cu_{50}Zr_{50}$ are shown here but similar trends are found in the other liquids. As observed in Fig. 3.5, the majority of the distribution is in the region $1.25 < \alpha < 1.75$ for both the MD and mcRMC data. This corresponds to shapes that are close to that of a regular dodecahedron ($\alpha = 1.325$) but the regular octahedron ($\alpha = 1.654$) is also present. While the mcRMC fails to recreate the elemental resolved properties, worse than for the volume distribution, it does give the correct bounds for the asphericity.

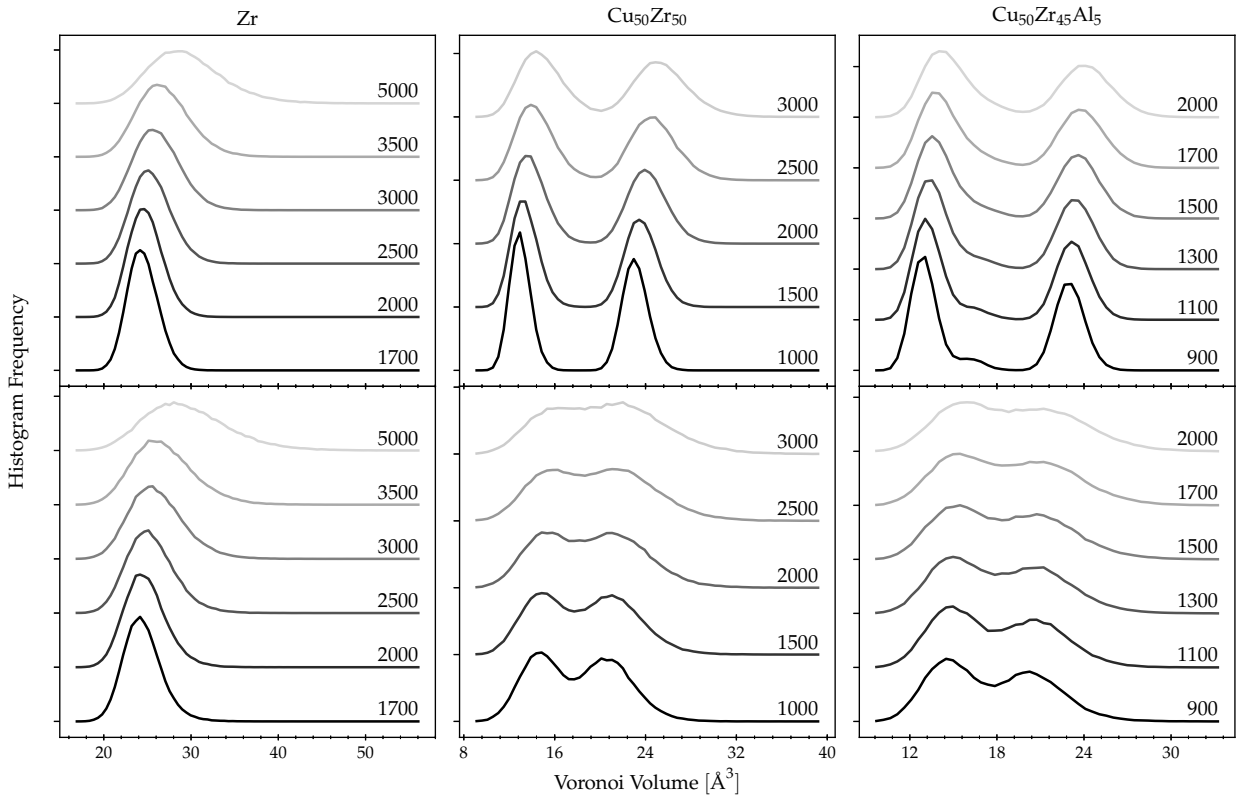

Figure 3.3: Frequency of Voronoi volume from MD (top row) and mcRMC (bottom row) for each composition. The temperatures [K] are indicated by shading (light is high and dark is low) and indicated on the right side of each curve. Each distribution is offset for clarity. Note that the distributions for mcRMC and MD match well for Zr but not for $Cu_{50}Zr_{50}$ and $Cu_{50}Zr_{45}Al_5$. Higher temperature distributions are broader for both mcRMC and MD.

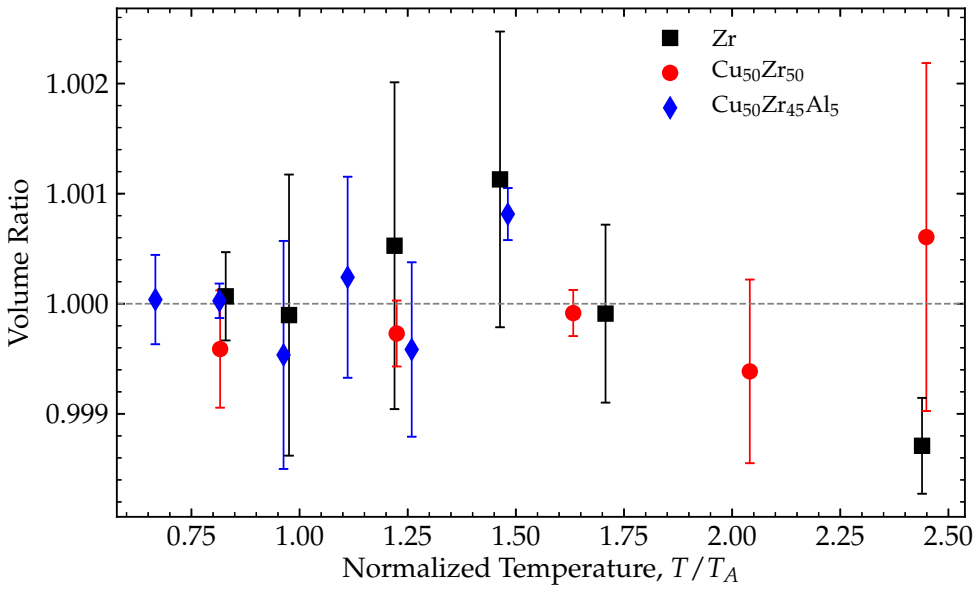

Figure 3.4: Ratio (MD/mcRMC) of average Voronoi polyhedra volume for Zr (square), $Cu_{50}Zr_{50}$ (circle), and $Cu_{50}Zr_{45}Al_5$ (diamond) versus temperature, normalized to the Arrhenius crossover temperature T_A. This ratio should be equal to one (dashed gray line).

Upon cooling the average asphericity decreases toward the value of the regular dodecahedron (among others). This is the case for all liquids studied because the magnitudes of their asphericities are similar. The ratio of the average MD to average mcRMC values (Fig.3.6) shows that the mcRMC fails to recreate the average properties of the VP shape distribution, both in magnitude and temperature dependence, except for Zr where only the magnitude is marginally different. This result for Zr is likely due to the increased disorder from the mcRMC simulation.

3.3.3 Voronoi Index and Coordination Number

The VI is perhaps the most commonly used parameter to describe the local environment from a Voronoi tessellation. It is also the least general of the parameters discussed here, since it describes average properties of groups of VPs rather than system-wide average properties. Ash shown earlier in Fig 3.2, the VI has a relatively large L^1 distance for all compositions. The Zr VI L^1 distance is, however, surprising due to the anomalous temperature dependence.

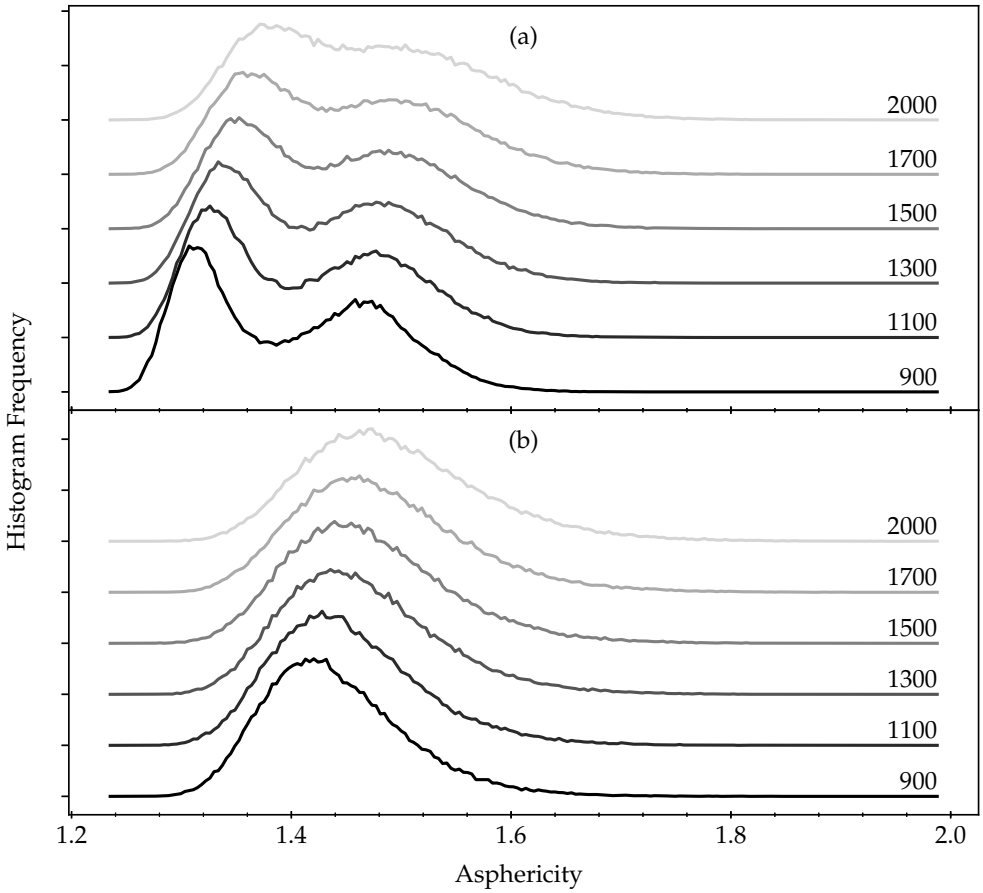

Figure 3.5: Histogram frequency for asphericity for $Cu_{50}Zr_{50}$ from (a) MD and (b) mcRMC. Each line indicates a different temperature; the curves are offset for clarity.

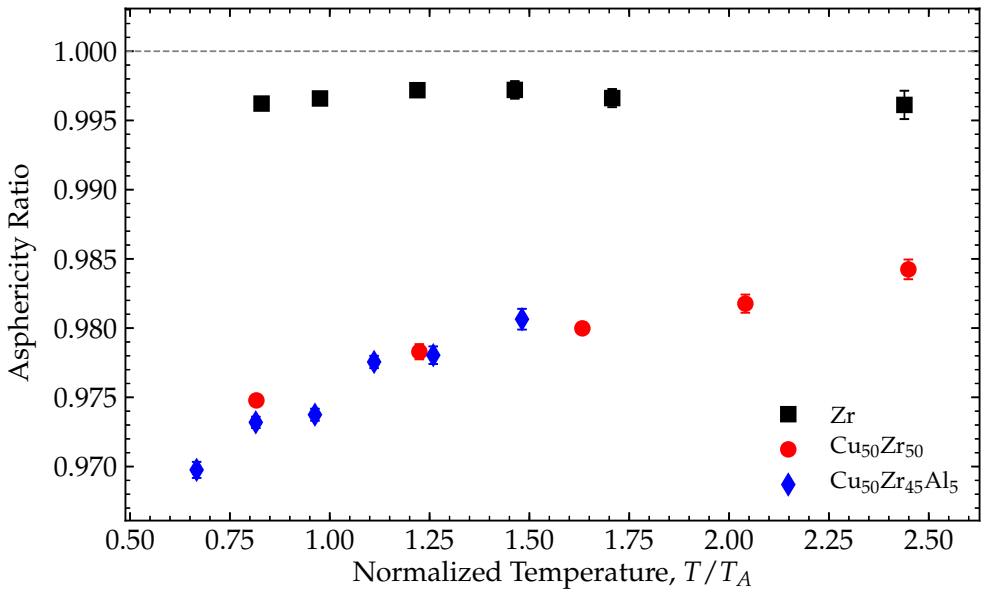

Figure 3.6: Ratio (MD/mcRMC) of the asphericity parameter for Zr (square), $Cu_{50}Zr_{50}$ (circle), and $Cu_{50}Zr_{45}Al_5$ (diamond) versus temperature normalized to the Arrhenius crossover temperature T_A. If the mcRMC analysis recreated the MD configurations perfectly the ratio should be one (dashed line).

It is also interesting to note that even for Zr the relatively large L^1 distance of the VI indicates that the population of VIs do not properly reflect that in the MD data, even with a fully constrained system. One contributing factor to this anomalous increase is the increase of VPs that are only present in either the mcRMC or the MD results, which in general increases with temperature. The total percentage attributable to these factors at high temperatures can be as large as %20 (Fig. 3.7). However, for Zr the temperature dependence of these factors is not enough to change the temperature dependence, which points to another factor. Whether this is a true effect or is an artifact is still under investigation.

The use of any single VI to determine agreement between the methods is difficult since different systems will in general prefer different structures. If the VI definition is extended to allow for fractional numbers of faces an "average" VP can be constructed for each simulation. No physical meaning is attached to the fractional numbers of faces; rather it provides another measure of mcRMC reproducibility of the atomic environment. Performing this analysis on the three compositions studied here and then comparing the average VPs from mcRMC and

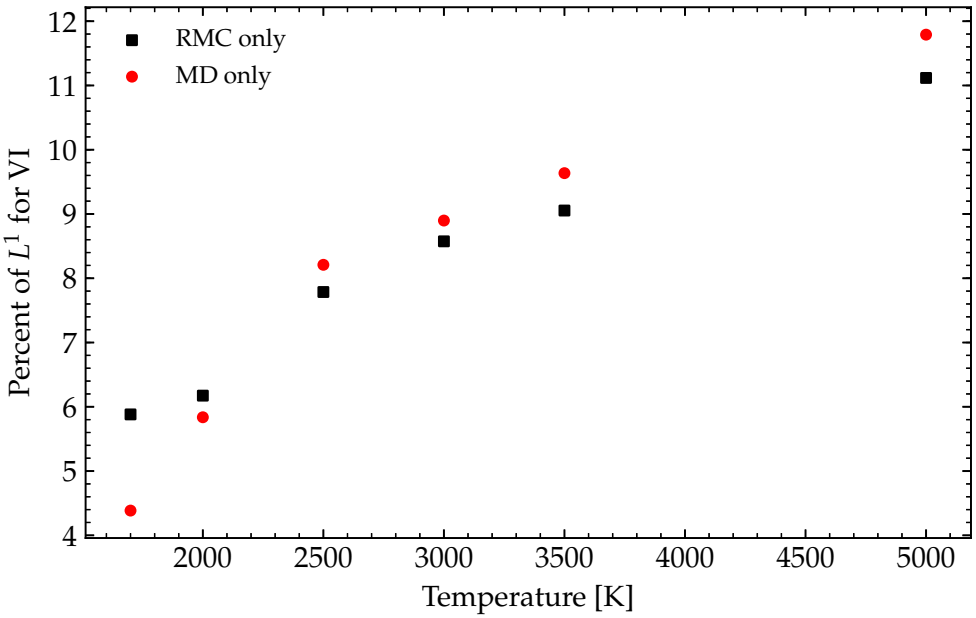

Figure 3.7: The percent of the Voronoi index L^1 distance for Zr as a function of temperature that is due to polyhedra only in RMC (square) and only in MD (circle).

MD gives extraordinarily low L^1 distances (Fig.3.8) that are in-line with the values for the NND (Fig. 3.2). In this sense the average atomic environment is reproduced quite well from mcRMC. However, a distinct dependence on the number of elements is observed, indicating that while the average atomic environment is reproduced well the addition of more types of atoms, even in small amounts, decreases the reliability of the mcRMC. This is not surprising since the amount of missing information for the mcRMC increases with the addition of more elements. To our knowledge, however, this analysis is the only one that shows such clear evidence of this effect.

The CN is included because of its strong relation to the VI. However, it suffers from the same issues as the volume and many other parameters. The mcRMC is unable to allocate the proper space for different types of atoms, causing the distribution of CNs to lie somewhere between the elemental distributions. This is also the cause of the relatively large L^1 distance as shown in Fig. 3.2.

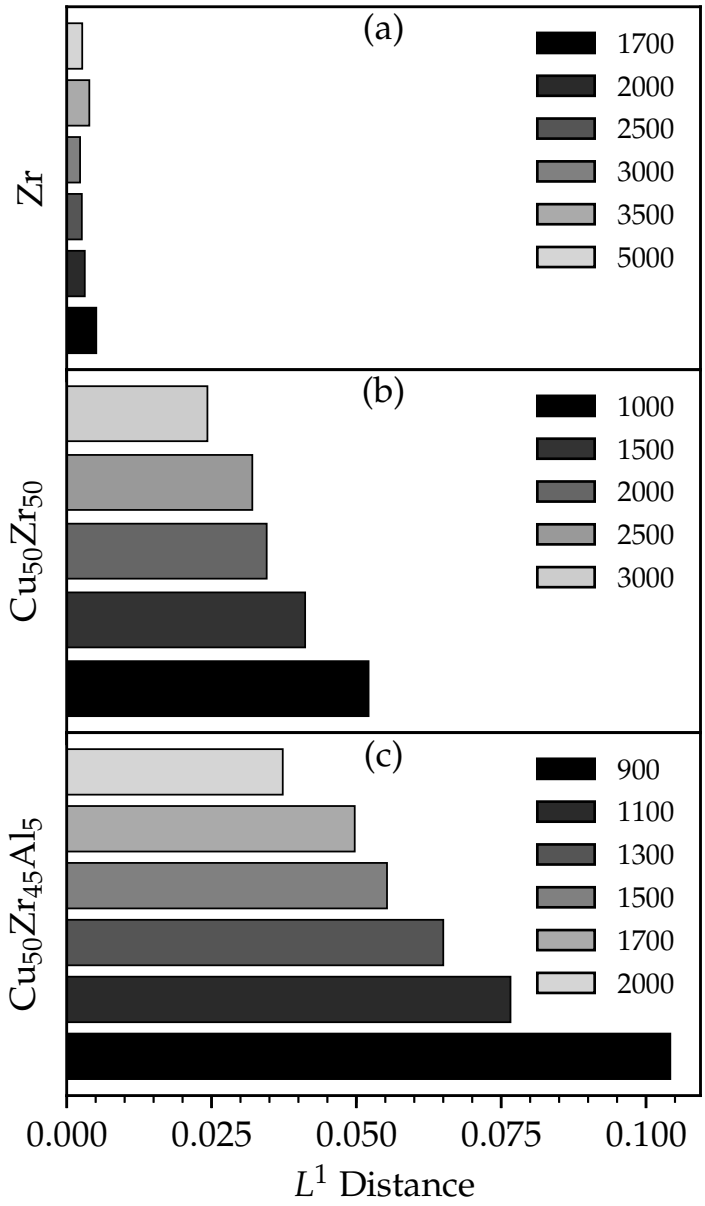

Figure 3.8: L^1 distance for the average VP of (a) Zr, (b) $Cu_{50}Zr_{50}$, and (c) $Cu_{50}Zr_{45}Al_5$. The average VP is computed by extending the typical VI definition to allow for fractional faces.

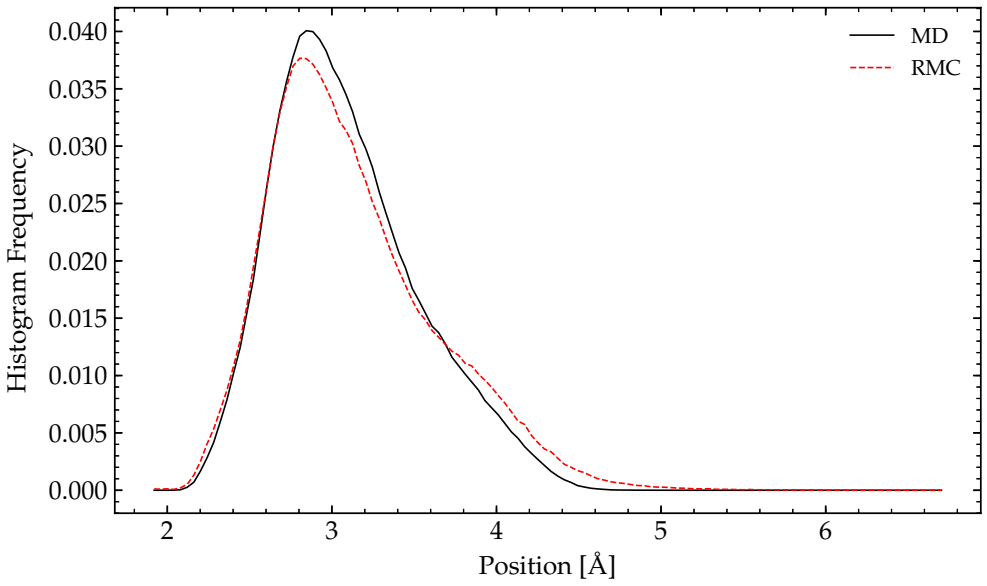

Figure 3.9: Nearest-neighbor distance histograms for both the MD (solid line) and mcRMC (dashed line) simulations of $Cu_{50}Zr_{45}Al_5$ at $T = 900$K. The histogram frequency is normalized so that it sums to one. Only the lowest temperature distribution for $Cu_{50}Zr_{45}Al_5$ is shown because it has the largest differences for all of the compositions and temperatures examined.

3.3.4 Nearest-neighbor Distance

In addition to the volume the NND is the other most easily reproducible parameter from RMC, since the input TPCF data is inherently related to this distance through the radial distribution function. Even when using the TPCF as a single constraint the RMC simulation should give a reliable distribution for the NND on average, although chemical effects and elementally resolved distances will still be absent. This reliability is reflected in the low L^1 distance shown in Fig. 3.2. The L^1 distance is the smallest of any parameter considered regardless of the number of elements or temperature. As shown in Fig. 3.9 good agreement is found between MD and mcRMC, even for the worst case examined. Reverse Monte Carlo simulations tend to place atoms at marginally larger distances compared to the MD-generated structures, which is a consequence of the lack of input elemental and chemical information. However, the increased distance is asymmetric, since the low distance side is constrained by the hard-sphere cutoffs.

Since the L^1 distance is small both the average atomic position (bond length) should be well characterized by the RMC simulation. However, due to the asymmetric change in distance the bond length will have a modified temperature dependence compared to that from the MD simulation. A possible solution to this is to instead consider the median bond length as a measure of central tendency, which is less affected by this increased asymmetry. The ratios of MD to mcRMC ratio for both the median and mean NND are shown in Fig. 3.10 for all compositions. In Fig. 3.10a the average NND for $Cu_{50}Zr_{50}$ and $Cu_{50}Zr_{45}Al_5$ shows a different temperature dependence between the mcRMC and MD results. The effect of the RMC placing atoms at larger distances at lower temperatures is to depress the actual change which can be seen in the broadening of the first peak in TPCFs from scattering studies [35]. Furthermore, the median NND (Fig. 3.10b) shows relatively no temperature dependence for all compositions and a slightly reduced amplitude in comparison to the average value. This would indicate that even with no other constraints the NND distribution and even more so its median are reliable.

3.4 Summary

In the present study atomic structures created from molecular dynamics (MD) simulations for three different liquids were used to explore how well reverse Monte Carlo (RMC) fits to the MD-generated pair correlation functions reproduce the atomic structures. The worst case (also generally the one used to fit experimental data) was examined, using only the measured total pair correlation function to constrain the RMC fits (termed here a mcRMC analysis). An in-depth analysis of the Voronoi tessellation for the structures obtained from the MD and mcRMC was made by examining the distributions and measures of central tendency of the Voronoi volume, asphericity, Voronoi index, coordination number, and nearest-neighbor distance using the L^1 distance as a metric of similarity. While the mcRMC is able to reproduce some properties of each distribution, the structures were generally not well

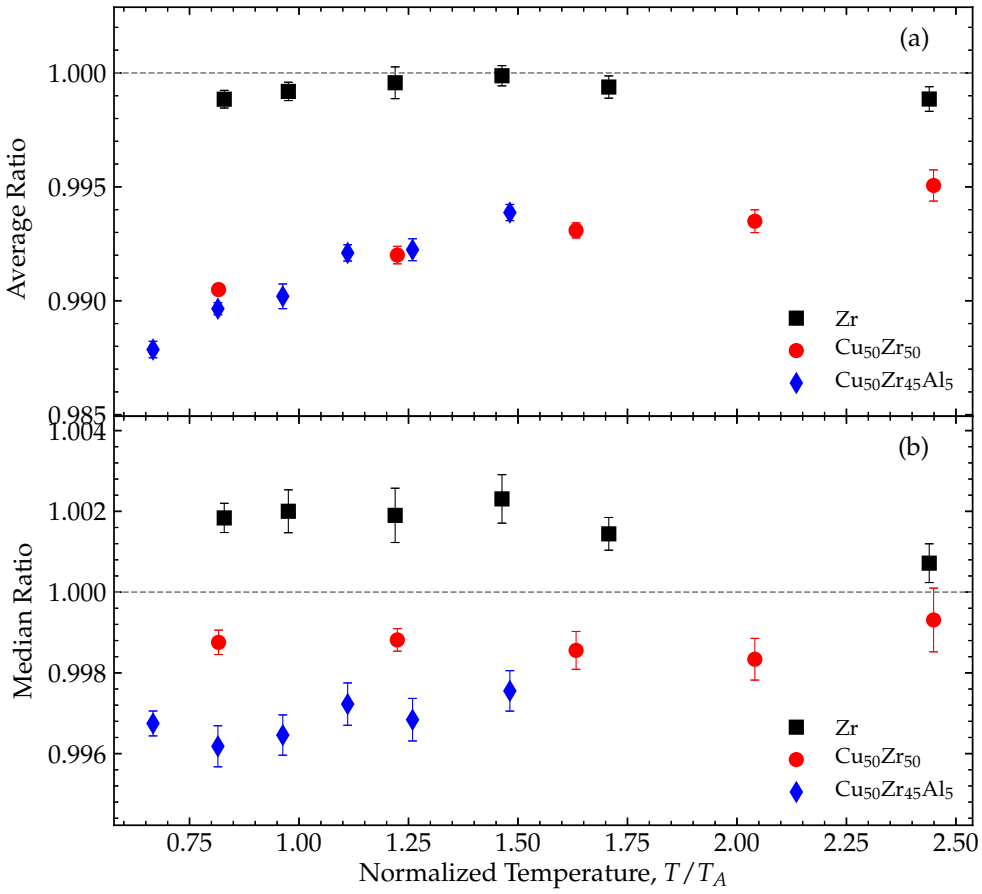

Figure 3.10: Plot of the MD to mcRMC ratio of average (a) and median (b) nearest-neighbor distances for Zr (square), $Cu_{50}Zr_{50}$ (circle), and $Cu_{50}Zr_{45}Al_5$ (diamond) versus temperature normalized to T_A, the Arrhenius crossover temperature. The ideal value of one is marked by a dashed gray line.

reproduced. That the fit properties were questionable raises doubts about the use of RMC for systems that are not fully constrained and the validity of more demanding properties of the configuration (i.e. network analysis). However, the predicted mean volume and median nearest neighbor distances were better predicted, indicating that mcRMC can be reliably used to analyze experimental data to obtain these quantities. The temperature dependence of the distribution similarities was also examined. In general even for the fully constrained Zr liquid, the L^1 distance increases as the temperature decreases, indicating that the mcRMC results become less reliable. Extending these results to multicomponent systems such as metallic glasses, which are more likely to be constraint deficient, calls into question the reliability of mcRMC results. Further the glasses are generally more ordered than the liquids. Since the structure obtained from RMC simulations are the most disordered ones consistent with the scattering data, it is not possible to obtain a clear picture of the order except for in an averaged sense.

3.5 References

[1] R. Ashcraft and K. F. Kelton. Assessing the Reliability of Minimally Constrained Reverse Monte Carlo Simulations for Model Metallic Liquids (2018). arXiv: arXiv:1810.08511v1.

[2] R. L. McGreevy and L. Pusztai. Reverse Monte Carlo Simulation: A New Technique for the Determination of Disordered Structures. *Molecular Simulation* **1**,6 (1988). DOI: 10.1080/08927028808080958.

[3] R. L. McGreevy. Reverse Monte Carlo modelling. *Journal of Physics: Condensed Matter* **13**,46 (2001). DOI: 10.1088/0953-8984/13/46/201.

[4] R. Car and M. Parrinello. Unified Approach for Molecular Dynamics and Density-Functional Theory. *Physical Review Letters* **55**,22 (1985). DOI: 10.1103/PhysRevLett.55.2471. arXiv: 0610552 [arXiv:cond-mat].

[5] S. Y. Wang et al. Short- and medium-range order in a Zr73Pt27 glass: Experimental and simulation studies. *Physical Review B - Condensed Matter and Materials Physics* **78**,18 (2008). DOI: 10.1103/PhysRevB.78.184204.

[6] O. Gereben and L. Pusztai. Understanding the structure of molecular liquids via combinations of molecular dynamics simulations and Reverse Monte Carlo modeling: Handling information deficiency. *Journal of Non-Crystalline Solids* **407**, (2015). DOI: 10.1016/j.jnoncrysol.2014.08.047.

[7] N. P. Smolin et al. The analysis of the short-range-order atomic structure of liquid metals by the Voronoi polyhedron method and a check of the adequacy of the results gained by the RMC method. *Journal of Non-Crystalline Solids* **312-314**, (2002). DOI: 10.1016/S0022-3093(02)01655-1.

[8] B. R. Gelchinski et al. Use of the Voronoi polyhedra method for analyzing short-range-order of liquid cesium and its reproducibility in reverse Monte Carlo modeling. *Journal of Non-Crystalline Solids* **250**, (1999). DOI: 10.1016/S0022-3093(99)00109-X.

[9] M. I. Mendelev and M. J. Kramer. Reliability of methods of computer simulation of structure of amorphous alloys. *Journal of Applied Physics* **107**,7 (2010). DOI: 10.1063/1.3359710.

[10] X. W. Fang et al. Structure of Cu64.5Zr35.5 metallic glass by reverse Monte Carlo simulations. *Journal of Applied Physics* **115**,5 (2014). DOI: 10.1063/1.4865164.

[11] G. A. Almyras et al. Atomic cluster arrangements in Reverse Monte Carlo and Molecular Dynamics structural models of binary Cu-Zr Metallic Glasses. *Intermetallics* **19**,5 (2011). DOI: 10.1016/j.intermet.2011.01.001.

[12] G. Voronoi. Nouvelles applications des paramètres continus à la théorie des formes quadratiques. Deuxième mémoire. Recherches sur les paralléllòèdres primitifs. *Journal für die reine und angewandte Mathematik (Crelle's Journal)* **1908**,134 (1908). DOI: 10.1515/crll.1908.134.198.

[13] J. L. Finney. Random Packings and the Structure of Simple Liquids. I. The Geometry of Random Close Packing. *Proceedings of the Royal Society A: Mathematical, Physical and Engineering Sciences* **319**,1539 (1970). DOI: 10.1098/rspa.1970.0189.

[14] Y. Q. Cheng and E. Ma. Atomic-level structure and structure-property relationship in metallic glasses. *Progress in Materials Science* **56**,December 2010 (2011). DOI: 10.1016/j.pmatsci.2010.12.002.

[15] J. D. Honeycutt and H. C. Andersen. Molecular dynamics study of melting and freezing of small Lennard-Jones clusters. *Journal of Physical Chemistry* **91**,19 (1987). DOI: 10.1021/j100303a014.

[16] S. Plimpton. Fast Parallel Algorithms for Short-Range Molecular Dynamics. *Journal of Computational Physics* **117**,1 (1995). DOI: 10.1006/jcph.1995.1039. arXiv: nag.2347 [10.1002].

[17] M. I. Mendelev and G. J. Ackland. Development of an interatomic potential for the simulation of phase transformations in zirconium. *Philosophical Magazine Letters* **87**,February 2012 (2007). DOI: 10.1080/09500830701191393.

[18] M. Mendelev et al. Development of suitable interatomic potentials for simulation of liquid and amorphous Cu-Zr alloys. *Philosophical Magazine* **89**,11 (2009). DOI: 10.1080/14786430902832773.

[19] Y. Q. Cheng, E. Ma, and H. W. Sheng. Atomic level structure in multicomponent bulk metallic glass. *Physical Review Letters* **102**,June (2009). DOI: 10.1103/PhysRevLett.102.245501.

[20] S. Nosé. A unified formulation of the constant temperature molecular dynamics methods. *The Journal of Chemical Physics* **81**,1 (1984). DOI: 10.1063/1.447334.

[21] W. G. Hoover. Canonical dynamics: Equilibrium phase-space distributions. *Physical Review A* **31**,3 (1985). DOI: 10.1103/PhysRevA.31.1695.

[22] Y. Waseda. *The Structure of Non-Crystalline Materials*. New York: McGraw-Hill Inc., 1980.

[23] J.-P. Hansen and I. R. McDonald. *Theory of Simple Liquids: with Applications to Soft Matter*. Fourth. Amsterdam: Elsevier/AP, 2013.

[24] O. Gereben et al. A new version of the RMC++ Reverse Monte Carlo programme, aimed at investigating the structure of covalent glasses. *Journal of Optoelectronics and Advanced Materials* **9**,10 (2007).

[25] J. Park and Y. Shibutani. Common errors of applying the Voronoi tessellation technique to metallic glasses. *Intermetallics* **23**, (2012). DOI: 10.1016/j.intermet.2011.12.019.

[26] B. J. Gellatly and J. L. Finney. Calculation of protein volumes: An alternative to the Voronoi procedure. *Journal of Molecular Biology* **161**,2 (1982). DOI: 10.1016/0022-2836(82)90155-3.

[27] M. Gerstein, J. Tsai, and M. Levitt. The volume of atoms on the protein surface: Calculated from simulation, using Voronoi polyhedra. *Journal of Molecular Biology* **249**,5 (1995). DOI: 10.1006/jmbi.1995.0351.

[28] W. Brostow et al. Voronoi polyhedra and Delaunay simplexes in the structural analysis of molecular-dynamics-simulated materials. *Physical Review B* **57**,21 (1998). DOI: 10.1103/PhysRevB.57.13448.

[29] C. H. Rycroft et al. Analysis of granular flow in a pebble-bed nuclear reactor. *Physical Review E - Statistical, Nonlinear, and Soft Matter Physics* **74**,2 (2006). DOI: 10.1103/PhysRevE.74.021306. arXiv: 0602395 [cond-mat].

[30] C. H. Rycroft. VORO++: A three-dimensional Voronoi cell library in C++. *Chaos* **19**,4 (2009). DOI: 10.1063/1.3215722. arXiv: 0402209 [cond-mat].

[31] W. F. Gale and T. C. Totemeier, eds. *Smithells Metals Reference Book*. 8th. Oxford: Butterworth-Heinemann, 2004.

[32] A. K. Bhattacharyya. On a measure of divergence between two statistical populations defined by their probability distributions. *Bulletin of the Calcutta Mathematical Society* **35**, (1943).

[33] E. Hellinger. Neue Begründung der Theorie quadratischer Formen von unendlichvielen Veränderlichen. *Journal für die reine und angewandte Mathematik (Crelle's Journal)* **1909**,136 (1909). DOI: 10.1515/crll.1909.136.210.

[34] G. Ruocco, M. Sampoli, and R. Vallauri. Molecular dynamics simulations of liquid water: Voronoi polyhedra and network topology. *Journal of Molecular Structure* **250**,2-4 (1991). DOI: 10.1016/0022-2860(91)85033-Y.

[35] J. Ding et al. Temperature effects on atomic pair distribution functions of melts. *The Journal of chemical physics* **140**,6 (2014). DOI: 10.1063/1.4864106.

Chapter 4: Estimates of bond length and thermal expansion coefficients from x-ray scattering experimental data using reverse Monte Carlo simulations

This chapter has been published on the arXiv [1] in collaboration with K. F. Kelton and is awaiting submission to a peer-reviewed journal. It has been adapted to be consistent with the formatting in this dissertation. The author's contributions include performing the Molecular Dynamics (MD) and Reverse Monte Carlo (RMC) simulations, analyzing the resulting data, and writing the manuscript. The authors and other group members contributed to acquiring the X-ray diffraction data and the resulting analysis. All authors contributed in drafting the results.

4.1 Introduction

The static structure factor, $S(q)$, and the related pair distribution function, $g(r)$, obtained from experimental scattering data are routinely used to deduce the linear thermal expansion coefficient,

$$\beta = \frac{1}{3V}\frac{\mathrm{d}V}{\mathrm{d}T} \ , \tag{4.1}$$

where V is the volume, for crystalline systems by tracking the position of the first peak as a function of temperature. Following the same method, some studies in metallic liquids have shown an anomalous contraction of the first peak in $g(r)$ with increasing temperature, indicating a negative thermal expansion coefficient. However, values of β obtained from

direct measurements of the volume have been positive [2, 3]. To explain this difference, it was suggested that the coordination number decreased with increasing temperature, forming stronger bonds between the atoms and a decrease in the atomic separation. However, later studies determined that the contraction was likely due to a failure to account for the asymmetry of the nearest-neighbor distance (NND) distribution [4–7]. This asymmetry of the NND distribution is a consequence of the redistribution of neighboring atoms to typically larger distances due to the anharmonicity of the interatomic potential. It has also been also suggested that due to the complex interplay of the partial pair correlation functions it is unlikely that reliable data for β can be obtained from the $g(r)$ for the liquid.

One of these studies [5] suggested a promising approach using a skew normal distribution (SND) to fit the first peak of the total radial distribution function,

$$R(r) = \frac{g(r)}{4\pi r^2 \rho} \ , \tag{4.2}$$

where ρ is the number density. This gives an effective nearest neighbor distribution that accounts for the increasing skewness, bypassing many of the issues arising with the use of peak positions. From the fit the mean bond length can be identified and tracked with temperature to obtain an approximate value for β. However, as the authors point out this approach is not without flaws. For multi-component alloys the main peak in $g(r)$ will contain multiple partial pair correlation functions that may not be well described by a single SND. One option would be to fit each partial $g(r)$ with a SND and then sum them with the usual weighting factors (e.g. Faber-Ziman[8] coefficients) to obtain the total $g(r)$. This would then give an effective total NND distribution. Experimentally, however, it is typically difficult to obtain the needed information on all the pair correlation functions to perform this type of analysis.

Here a more detailed examination of the NND distribution is presented that is based on RMC and MD modeling using a Voronoi tessellation. The main conclusion is that unlike $g(r)$

the robust measures of central tendency for the NND distribution are well behaved, exhibiting only expansion, and give reliable information about the linear thermal expansion coefficient. Furthermore, it is shown that the rate of expansion obtained from the NND distribution is equal to the rate obtained from direct volume measurements. This calls into question a recent proposal that liquid fragility [9] (a measure of the deviation of the temperature dependence of the activation energy of the viscosity) is related to the temperature dependence of the peak positions of the 3rd and 4th peak positions in $g(r)$ [10]. Finally, the results presented here give more evidence of the local nature of fragility, which was recently reported [11].

4.2 Experimental and Analysis Methods

4.2.1 Experimental Methods

Equilibrium and supercooled liquid structural data was obtained at the Advanced Photon Source at Argonne National Laboratory on beamline 6ID-D using the beamline electrostatic levitation (BESL) technique. Density and thermal expansion measurements were made from video images of levitated samples back-lit by a high-intensity LED. The details of these experimental methods can be found elsewhere [2, 12–15].

4.2.2 Molecular Dynamics Simulations

Molecular dynamics (MD) simulations were made for 10 compositions using the LAMMPS [16] software. Some simulations employed the GPU package of LAMMPS [17–19]. Each simulation consisted of 15,000 atoms contained in a cubic box with periodic boundary conditions in the NPT ($P = 0$) ensemble. The Nosé-Hoover thermostat was used to equilibrate each system at each temperature before data collection. Ten configurations were used to obtain statistics on the NND distribution.

4.2.3 Reverse Monte Carlo Simulations

Reverse Monte Carlo simulations were made for 34 metallic liquids using the RMC++ [20] software. Structure factors, $S(q)$, obtained from X-ray scattering experiments were used as the only constraint. Reverse Monte Carlo simulations perform a minimization of the χ^2 given by

$$\chi^2 = \sum_i \frac{[S'(q) - S(q)]}{\sigma^2} \tag{4.3}$$

where $S'(q)$ is the structure factor calculated from the RMC atomic configuration, $S(q)$ is the experimental data, and σ is the reliability of the data set. This minimization is achieved by moving atoms, which are chosen randomly, in a random direction and computing the new χ^2 from this configuration. If the χ^2 is reduced the move is accepted while if the χ^2 increases the move is accepted according to a Boltzmann probability. This procedure is then repeated until the χ^2 is minimized.

The reliability of such minimally constrained simulation has been examined in a recent study (Chapter 3). To generate sufficient statistics and determine error in the Voronoi tessellation each liquid was simulated seven times. Each RMC simulation consisted of 10,000 randomly generated atoms in a cubic box whose size is consistent with the experimental number density of the liquid, using periodic boundary conditions. Minimum cutoff distances and swapping positions between atoms of different elements were used to improve the convergence time. Convergence was assumed when both the magnitude and the change with time of the χ^2 were sufficiently small.

4.2.4 Voronoi Tessellation

Voronoi tessellation was performed on each RMC configuration using a Python extension of the Voro++[21, 22] software. The Voronoi tessellation procedure can lead to significant errors when systems with different sized atoms are considered [23]. To account for this radical Voronoi tessellation [24, 25] was used for all systems containing multiple elements. In

this method, the distance to each bisecting plane is weighted by the radius of each atom; the Goldschmidt radii [26] were used for this weighting. Another error common to Voronoi tessellation is the occurrence of exceptionally small faces and edges, compared to the polyhedron average, which occur from slightly more distant atoms [27]. These more distant atoms tend to exaggerate the skewness of the "true" nearest-neighbor distribution. To attempt to account for this effect, small-faces were removed using a percentage of the system polyhedron average face area as the cutoff. Repeating this removal for multiple values gives a determination of the reliability of the final results.

A more robust method for removing more distant nearest neighbors was developed using Gaussian mixtures modeling (GMM), which is a fuzzy clustering algorithm. This method assumes that the NND and face area data are composed of two Gaussian distributions coming from only the more distant "artifact" atoms and the "true" nearest neighbors. The data is then clustered into groups according to the probability of inclusion in each distribution. Using the Scikit-learn Python library [28] a single Voronoi tessellation was fit. This fit was then used to predict which distribution each NND and face area pair belong to for the remaining Voronoi tessellations. This method, though more reasonable than a strict cutoff using face area, is still only approximate. Other clustering algorithms that are not mode-seeking and that allow for different size and covariance of clusters could also be used.

4.3 Results and Discussions

As mentioned in the preceding section a Voronoi tessellation often creates polyhedra with abnormally small faces. Figure 4.1 shows a typical distribution of the area of the faces of a Voronoi polyhedron and a typical Voronoi polyhedron which with a small face. Two distinct features are observed in the distribution, a peak corresponding to the larger-size faces representative of the typical NND and one corresponding to smaller faces, which come from more distant atoms. Although a clear minimum between the two peaks is observed here,

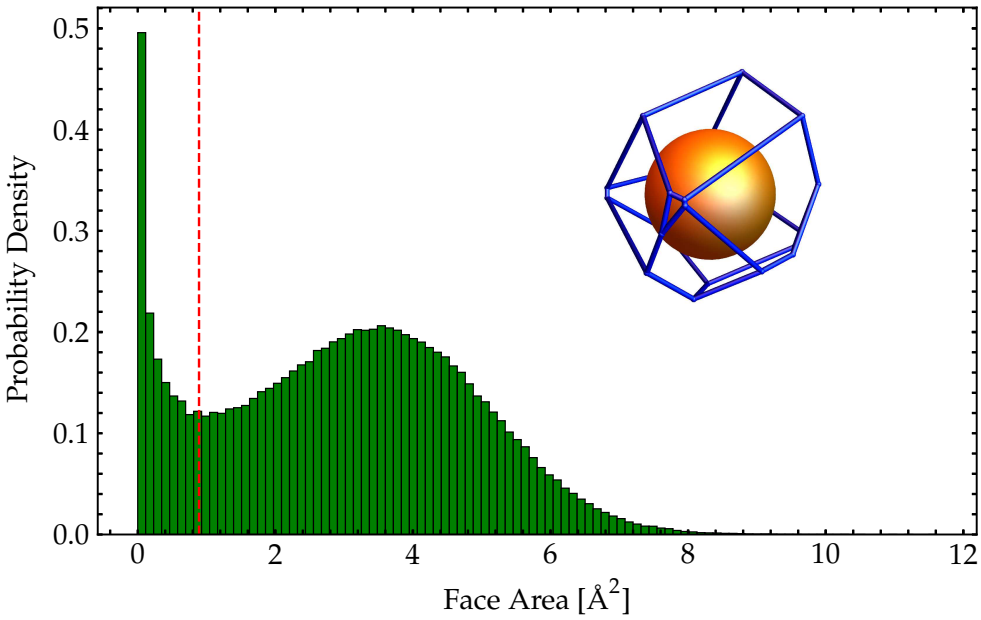

Figure 4.1: Representative probability density for polyhedron face area for $Zr_{80}Pt_{20}$ at $T = 1191$K. A schematic illustration of a Voronoi polyhedron that contains a small face is shown. The dashed line indicates an area cutoff using a fraction (here 0.3) of the average polyhedral face area.

providing an obvious choice for a cutoff, this is not always the case. Even for cases where there is an appreciable separation between the two peaks, the minimum becomes less prominent as the temperature of the system increases. Atoms are able to sample smaller and larger distances more frequently consistent with the anharmonicity of the interatomic potential. Since the overlap of these two distributions is significant, separating the two distributions becomes is non-trivial. A typical method for determining which faces to remove is to use a fraction of the average polyhedron face area, however the cutoff value from this method is arbitrary.

A less subjective method to separate the distributions (mentioned previously) is to use GMM, in which one Gaussian is centered on the "artifact" atoms and the other represents the true distribution of NNDs and face areas. Figure 4.2 shows a representative plot using the GMM method for the case of only two cluster centers and two features. The dashed lines are log-likelihood contour curves showing the probability of inclusion in each probability

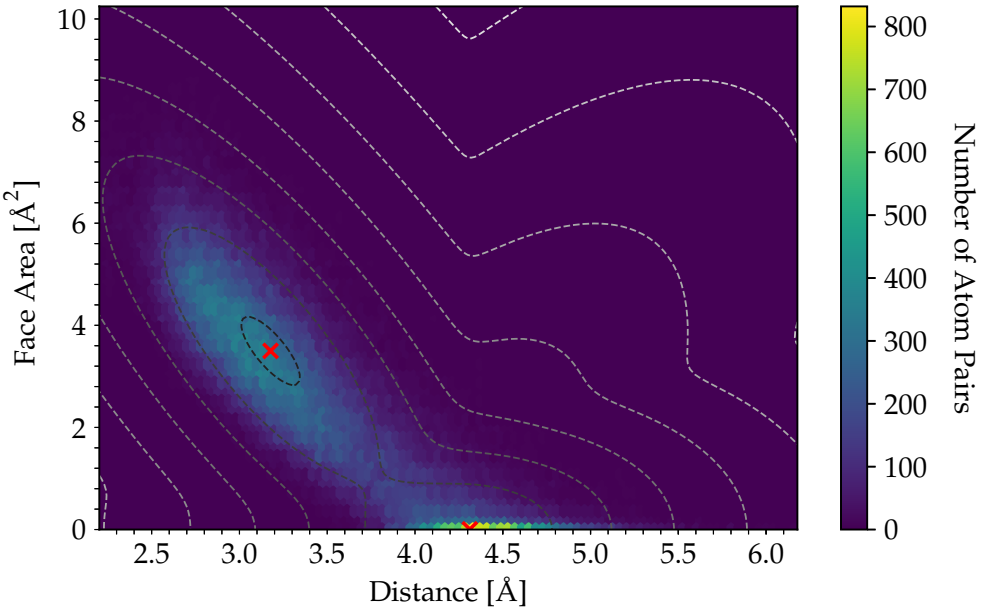

Figure 4.2: Representative hexbin plot for polyhedral face areas and nearest-neighbor distances for $Zr_{80}Pt_{20}$ at $T = 1191$K. The 'x' marks the centers of each Gaussian cluster. The dashed lines indicate the log-likelihood probability of being from a given distribution (dark shading indicates a high likelihood).

distribution and the crosses mark the centers of the distributions. This method does a good job of separating the distributions, but there are some limitations. By using a mixture of Gaussians the underlying NND distribution that is deduced is assumed to be Gaussian. However, this distribution is known to be inherently asymmetric due to the anharmonicity of the interatomic potential. It is also clear that the data points do not recreate the log-likelihood curves exactly, again indicating that a Gaussian distribution is not the best assumption. Finally, this method will tend to underestimate the skewness since the prediction uses a simple maximum probability to ascertain inclusion in a cluster, meaning that farther atoms will not be included. By including more features (i.e. polyhedron face perimeter etc.) in the GMM it might be possible to better determine the true NND distribution. However, care needs to be employed when increasing the number of features for multi-component systems, since the different atom types may cause unexpected clustering. In this case it may be necessary to isolate elements even for RMC simulations where chemical effects are not reproduced well.

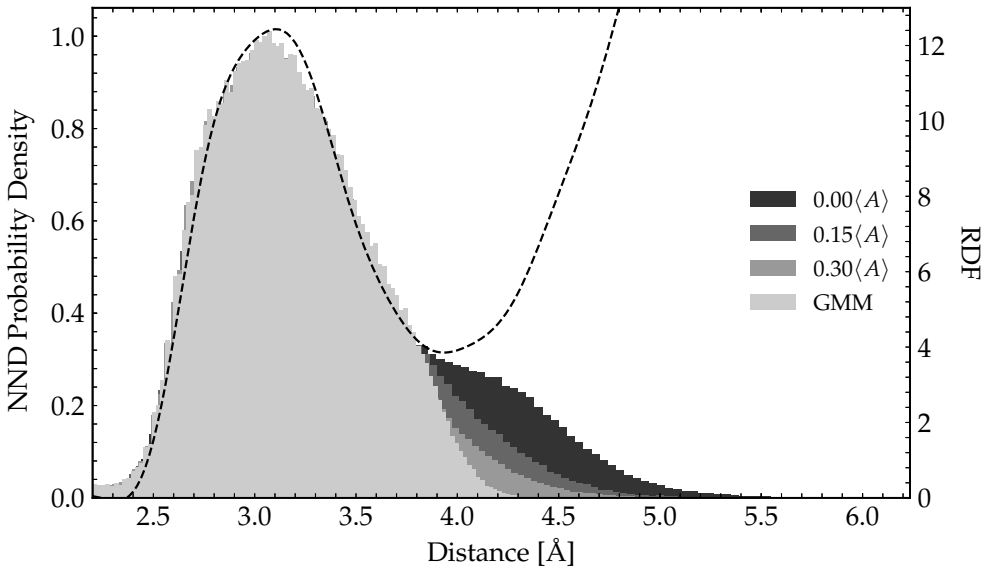

Figure 4.3: Plot of a representative, $Zr_{80}Pt_{20}$ nearest-neighbor distance distribution at $T = 1191$K (left) using each cutoff method (shading darkest to lightest): removing $A < 0.0$, $A < 0.15\langle A\rangle$, $A < 0.30\langle A\rangle$, (where A is the polyhedron face area) and using the Gaussian mixtures modeling. The radial distribution function (dashed line, right axis) is also shown for comparison.

A representative NND distribution is shown in Fig. 4.3 using each of the examined cutoff methods.

The linear expansion coefficients estimated from the GMM and fractional cutoff analyses, β_{Mean}, are shown as a function of the linear expansion coefficient measured from the volume change, β_{Volume} in Fig. 4.4. A strong correlation between these expansion coefficients exists, regardless of the method used to remove small faces, and even for the case when no faces were removed. This indicates, in contrast to recent claims[5, 7], that the expansivity can be deduced from the structural data with proper modeling. No more information is required other than that used to obtain $g(r)$. It is also important to note that the slope of the best fit line approaches unity if a sufficient number of faces are removed, indicating that the rate of expansion of the first shell is commensurate with that of the bulk. Since the local neighbor configurations expand as the same rate as the volume expansion, it is reasonable to conclude that all higher order coordination shells will expand at this rate as well.

From an examination of the peak positions in $G(r) = 4\pi r\rho[g(r) - 1]$ a recent study

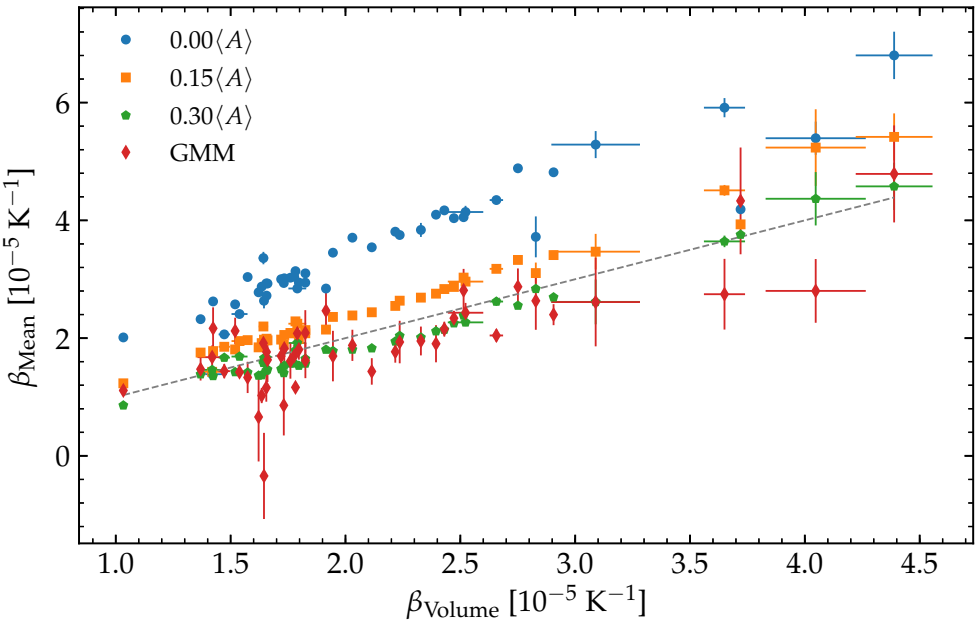

Figure 4.4: A comparison of the linear expansion coefficient from the mean of the nearest-neighbor distance distribution (β_{Mean}) with that obtained from direct measurements of the volume (β_{Volume}) evaluated at the liquidus temperature. The values for β_{Mean} obtained for removing no faces (circle), faces where $A < 0.15\langle A\rangle$ (square), faces where $A < 0.30\langle A\rangle$ (pentagon) and faces using the Gaussian mixture modeling (diamond). The dashed line shows the case of $\beta_{\mathrm{Mean}} = \beta_{\mathrm{Volume}}$ as a guide for the eye.

concluded that the fourth coordination shell is correlated with kinetic fragility [10]. Rather than tracking $g(r)$, $G(r)$ was examined since less information is required to obtain that quantity. However, $G(r)$ still exhibits the same asymmetric skewing as $g(r)$, raising doubts about the reliability of the conclusions drawn. In light of the results presented here, the lack of correlation with coordination shells lower than the fourth, especially the first coordination shell, is likely a result of not tracking the NNDs in the proper way. It is not surprising to find a correlation with higher order shells when using these weaker metrics for the central tendency, since the distribution of atoms tends to be less skewed for higher order coordination shells, since atoms are distributed more symmetrically (at longer distances the interatomic potential is more symmetric). If each coordination shell expands at the same rate then all of the metrics, $m_{str}^{(V_{i-j})}$ and $m_{str}^{(r_i)}$ used in the previous study reduce to the volume change between T_g (the glass transition temperature) and 0K or 1/3 of this value, respectively, extrapolated from the liquid which is a statement that the expansivity is related to the fragility as in [29].

The expansion coefficients for the best case shown in Fig. 4.4, i.e. removing faces with area less than 30% of the average face area, are listed in Table 4.1. The linear expansion coefficient calculated from the median and mode of the NND distribution are also listed. Since both the median and the mean use the entire distribution to give a measure of the central tendency it is not surprising that they give consistent estimates of an expansion, while the mode can give both expansion and contraction. The mode then tracks the behavior of the peak position of $g(r)$, technically $R(r)$ the radial distribution function. This analysis supports the conclusion of others [4, 7] who claim that the anomalous contraction previously reported fails to consider the increased skewness and deviation from Gaussian behavior. In particular, we see that it is dangerous to infer changes in the local configuration using the peak position for either $g(r)$ or $R(r)$, since they are not consistent estimators of the underlying atomic distribution.

Composition	Liquidus (K)	β_{Mean} (10^{-5}K^{-1})	β_{Median} (10^{-5}K^{-1})	β_{Mode} (10^{-5}K^{-1})	β (10^{-5}K^{-1})
Al	933	3.6(0.1)	3.1(0.1)	-3.0(1.0)	3.65(0.09)

†Al [30]	926	4.6(0.4)	4.0(0.3)	0.61(0.2)	4.4(0.2)
†Cu [30]	1353	2.6(0.4)	2.0(0.2)	0.41(0.1)	3.1(0.2)
$Cu_{30}Zr_{30}Ti_{40}$	1113	1.78(0.03)	1.5(0.04)	0.37(0.9)	1.945(0.001)
$Cu_{46}Zr_{54}$	1198	1.94(0.02)	1.61(0.02)	0.15(0.5)	2.2169(0.0007)
$Cu_{47}Zr_{47}Al_6$	1180	2.04(0.03)	1.84(0.03)	2.0(2.0)	2.236(0.001)
$Cu_{50}Zr_{42.5}Ti_{7.5}$	1152	2.14(0.02)	2.02(0.01)	6.0(1.0)	2.43(0.001)
$Cu_{50}Zr_{45}Al_5$	1173	2.117(0.008)	2.07(0.03)	7.0(1.0)	2.394(0.001)
$Cu_{50}Zr_{50}$	1222	2.01(0.02)	1.8(0.04)	3.0(1.0)	2.328(0.002)
†$Cu_{50}Zr_{50}$ [31]	1222	1.79(0.02)	1.63(0.02)	1.8(0.3)	1.78(0.01)
$Cu_{60}Zr_{20}Ti_{20}$	1127	2.55(0.02)	2.44(0.02)	0.069(0.3)	2.751(0.001)
$Cu_{64}Zr_{36}$	1200	2.69(0.01)	2.9(0.01)	0.086(0.3)	2.906(0.003)
Ge	1211	3.76(0.03)	3.87(0.03)	1.8(0.6)	3.72(0.002)
LM601	1157	1.83(0.02)	1.4(0.05)	-0.33(0.8)	2.115(0.002)
Ni	1728	2.84(0.06)	2.4(0.2)	2.0(2.0)	2.82865(3e-05)
†Ni [32]	1728	4.4(0.5)	3.4(0.3)	0.28(0.2)	4.0(0.2)
$Ni_{59.5}Nb_{40.5}$	1448	1.81(0.04)	1.75(0.05)	0.39(0.3)	2.03(0.002)
†$Ni_{62}Nb_{38}$ [33]	1523	2.62(0.07)	2.54(0.03)	1.0(0.1)	2.66(0.03)
$Pd_{82}Si_{18}$	1081	2.25(0.02)	1.23(0.02)	-2.2(0.3)	2.472(0.002)
Pt	2041	1.66(0.04)	1.5(0.2)	-2.1(0.9)	1.656(0.006)
†Pt [34]	1890	1.69(0.02)	1.734(0.009)	-0.344(0.01)	1.54(0.03)
†Si()	1687	1.46(0.04)	1.4(0.05)	50.0(20.0)	1.42(0.06)
†Ta [35]	3290	0.858(0.03)	0.755(0.03)	0.2(0.1)	1.03(0.02)
Ti	1941	1.8(0.03)	1.82(0.04)	1.5(0.5)	1.9151(0.0001)
†Ti [36]	1918	1.67(0.02)	1.65(0.03)	1.88(0.07)	1.47(0.02)
$Ti_{38.5}Zr_{38.5}Ni_{23}$	1126	1.57(0.02)	1.05(0.02)	-0.94(0.4)	1.7603(0.0008)
$Ti_{40}Zr_{10}Cu_{30}Pd_{20}$	1189	2.38(0.03)	2.09(0.04)	-0.62(0.5)	2.514(0.002)
$Ti_{40}Zr_{10}Cu_{36}Pd_{14}$	1185	2.27(0.06)	2.03(0.04)	-0.072(0.2)	2.52(0.08)
$Ti_{45}Zr_{45}Ni_{10}$	1543	1.66(0.09)	1.2(0.1)	-3.0(2.0)	1.645(0.003)
Vit105	1093	1.57(0.03)	0.94(0.04)	-0.57(0.6)	1.825(0.002)
Vit106	1123	1.53(0.02)	0.841(0.04)	-1.2(0.4)	1.734(0.001)
Vit106a	1125	1.47(0.03)	0.833(0.03)	-0.29(0.3)	1.7199(0.0007)
Zr	2128	1.42(0.01)	1.38(0.02)	-0.15(0.8)	1.52(0.003)
†Zr [37]	2109	1.92(0.07)	1.67(0.04)	1.1(0.1)	1.79(0.04)
$Zr_{50}Ti_{50}$	1823	1.65(0.02)	1.47(0.02)	0.47(0.5)	1.825(0.001)
$Zr_{56}Co_{28}Al_{16}$	1241	1.53(0.02)	0.733(0.02)	-1.8(0.5)	1.797(0.001)
$Zr_{57}Ni_{43}$	1433	1.41(0.02)	1.01(0.04)	-0.91(0.6)	1.731(0.001)
$Zr_{59}Ti_3Ni_8Cu_{20}Al_{10}$	1145	1.47(0.02)	0.825(0.02)	-0.72(0.2)	1.661(0.001)
$Zr_{60}Ni_{25}Al_{15}$	1248	1.36(0.06)	0.612(0.04)	-0.59(0.8)	1.622(0.003)
$Zr_{62}Ni_8Cu_{20}Al_{10}$	1145	1.57(0.02)	0.832(0.03)	-1.1(0.2)	1.777(0.001)
$Zr_{64}Ni_{25}Al_{11}$	1212	1.37(0.02)	0.597(0.04)	-0.66(0.6)	1.635(0.001)
$Zr_{65}Al_{7.5}Cu_{17.5}Ni_{10}$	1170	1.45(0.02)	0.763(0.02)	-0.66(0.3)	1.655(0.001)
$Zr_{75.5}Pd_{24.5}$	1303	1.417(0.009)	1.04(0.02)	-0.59(0.5)	1.574(0.0008)
$Zr_{80}Pt_{20}$	1450	1.39(0.02)	1.17(0.02)	0.23(0.3)	1.3692(0.0005)
†$Zr_{80}Pt_{20}$ [38]	1450	1.58(0.03)	1.41(0.05)	1.8(0.2)	1.64(0.02)
$Zr_{82}Ir_{18}$	1513	1.36(0.02)	1.09(0.03)	-0.8(0.6)	1.424(0.001)

Table 4.1: Data for the linear expansion coefficient, β, for each composition using the mean, median, and mode of the nearest-neighbor distance distribution (removing faces with area $A < 0.3\langle A\rangle$), where $\langle A\rangle$ is the average face area, and the value from volumetric measurements evaluated at the liquidus temperature (melt for elementals and phase diagram values for MD systems which were not previously calculated). Error estimates are listed in parentheses. (†) denotes compositions which were simulated using MD.

4.4 Conclusion

The primary result of this study shows that to understand the change in the bond length as a function of temperature the nearest-neighbor distance distribution and robust measures of central tendency (such as the mean or median) should be considered, rather than $g(r)$ or any of its various forms that have typically been used. It is also shown that in agreement with recent studies [4, 6, 7] failing to account for the asymmetry of the NND distribution, but instead tracking the mode of the distribution, is the reason for the previously reported [2, 3] anomalous contraction. The thermal expansion coefficient is shown to be directly related to the shift in the mean of the NND distribution, and that the rate of expansion in the bulk is likely equal to the expansion in the NND. This calls into question the methods used in a recent study that correlates the shift in the peak positions and volumetric dilation with the kinetic fragility [10].

4.5 References

[1] R. Ashcraft and K. F. Kelton. Estimates of bond length and thermal expansion coefficients from x-ray scattering experimental data using reverse Monte Carlo simulations. **m**, (2018). arXiv: 1810.08889.

[2] A. K. Gangopadhyay et al. Anomalous thermal contraction of the first coordination shell in metallic alloy liquids. *Journal of Chemical Physics* **140**,4 (2014). DOI: 10.1063/1.4861666.

[3] H. Lou et al. Negative expansions of interatomic distances in metallic melts. *Proceedings of the National Academy of Sciences of the United States of America* **110**,25 (2013). DOI: 10.1073/pnas.1307967110.

[4] J. Ding et al. Temperature effects on atomic pair distribution functions of melts. *The Journal of chemical physics* **140**,6 (2014). DOI: 10.1063/1.4864106.

[5] S. V. Sukhomlinov and M. H. Müser. Determination of accurate, mean bond lengths from radial distribution functions. *The Journal of Chemical Physics* **146**,2 (2017). DOI: 10.1063/1.4973804.

[6] J. Ding and E. Ma. Computational modeling sheds light on structural evolution in metallic glasses and supercooled liquids. *npj Computational Materials* **3**,1 (2017). DOI: 10.1038/s41524-017-0007-1.

[7] A. K. Gangopadhyay and K. F. Kelton. A re-evaluation of thermal expansion measurements of metallic liquids and glasses from x-ray scattering experiments. *Journal of Chemical Physics* **148**,20 (2018). DOI: 10.1063/1.5032319.

[8] Y. Waseda. *The Structure of Non-Crystalline Materials*. New York: McGraw-Hill Inc., 1980.

[9] C. A. Angell. Formation of Glasses from Liquids and Biopolymers. *Science* **267**,5206 (1995). DOI: 10.1126/science.267.5206.1924.

[10] S. Wei et al. Linking structure to fragility in bulk metallic glass-forming liquids. *Applied Physics Letters* **106**,18 (2015). DOI: 10.1063/1.4919590.

[11] C. E. Pueblo, M. Sun, and K. F. Kelton. Strength of the repulsive part of the interatomic potential determines fragility in metallic liquids. *Nature Materials* **16**,8 (2017). DOI: 10.1038/nmat4935.

[12] N. A. Mauro and K. F. Kelton. A highly modular beamline electrostatic levitation facility, optimized for in situ high-energy x-ray scattering studies of equilibrium and supercooled liquids. *Review of Scientific Instruments* **82**,3 (2011). DOI: 10.1063/1.3554437.

[13] S. K. Chung, D. B. Thiessen, and W.-K. Rhim. A noncontact measurement technique for the density and thermal expansion coefficient of solid and liquid materials. *Review of Scientific Instruments* **67**,9 (1996). DOI: 10.1063/1.1147584.

[14] A. K. Gangopadhyay et al. Beamline electrostatic levitator for in situ high energy x-ray diffraction studies of levitated solids and liquids. *Review of Scientific Instruments* **76**,7 (2005). DOI: 10.1063/1.1932447.

[15] A. K. Gangopadhyay et al. Thermal expansion measurements by x-ray scattering and breakdown of Ehrenfest's relation in alloy liquids. *Applied Physics Letters* **104**,19 (2014). DOI: 10.1063/1.4876125.

[16] S. Plimpton. Fast Parallel Algorithms for Short-Range Molecular Dynamics. *Journal of Computational Physics* **117**,1 (1995). DOI: 10.1006/jcph.1995.1039. arXiv: nag.2347 [10.1002].

[17] W. M. Brown et al. Implementing molecular dynamics on hybrid high performance computers - short range forces. *Computer Physics Communications* **182**,4 (2011). DOI: 10.1016/j.cpc.2010.12.021.

[18] W. M. Brown et al. Implementing molecular dynamics on hybrid high performance computers - Particle-particle particle-mesh. *Computer Physics Communications* **183**,3 (2012). DOI: 10.1016/j.cpc.2011.10.012.

[19] W. M. Brown and M. Yamada. Implementing molecular dynamics on hybrid high performance computers - Three-body potentials. *Computer Physics Communications* **184**,12 (2013). DOI: 10.1016/j.cpc.2013.08.002.

[20] O. Gereben et al. A new version of the RMC++ Reverse Monte Carlo programme, aimed at investigating the structure of covalent glasses. *Journal of Optoelectronics and Advanced Materials* **9**,10 (2007).

[21] C. H. Rycroft et al. Analysis of granular flow in a pebble-bed nuclear reactor. *Physical Review E - Statistical, Nonlinear, and Soft Matter Physics* **74**,2 (2006). DOI: 10.1103/PhysRevE.74.021306. arXiv: 0602395 [cond-mat].

[22] C. H. Rycroft. VORO++: A three-dimensional Voronoi cell library in C++. *Chaos* **19**,4 (2009). DOI: 10.1063/1.3215722. arXiv: 0402209 [cond-mat].

[23] J. Park and Y. Shibutani. Common errors of applying the Voronoi tessellation technique to metallic glasses. *Intermetallics* **23**, (2012). DOI: 10.1016/j.intermet.2011.12.019.

[24] B. J. Gellatly and J. L. Finney. Calculation of protein volumes: An alternative to the Voronoi procedure. *Journal of Molecular Biology* **161**,2 (1982). DOI: 10.1016/0022-2836(82)90155-3.

[25] M. Gerstein, J. Tsai, and M. Levitt. The volume of atoms on the protein surface: Calculated from simulation, using Voronoi polyhedra. *Journal of Molecular Biology* **249**,5 (1995). DOI: 10.1006/jmbi.1995.0351.

[26] W. F. Gale and T. C. Totemeier, eds. *Smithells Metals Reference Book*. 8th. Oxford: Butterworth-Heinemann, 2004.

[27] W. Brostow et al. Voronoi polyhedra and Delaunay simplexes in the structural analysis of molecular-dynamics-simulated materials. *Physical Review B* **57**,21 (1998). DOI: 10.1103/PhysRevB.57.13448.

[28] F. Pedregosa et al. Scikit-learn: Machine Learning in Python. *Journal of Machine Learning Research* **12**, (2012). DOI: 10.1007/s13398-014-0173-7.2. arXiv: 1201.0490.

[29] A. K. Gangopadhyay et al. Correlation of the fragility of metallic liquids with the high temperature structure, volume, and cohesive energy. *Journal of Chemical Physics* **146**,15 (2017). DOI: 10.1063/1.4981011.

[30] M. I. Mendelev et al. Analysis of semi-empirical interatomic potentials appropriate for simulation of crystalline and liquid Al and Cu. *Philosophical Magazine* **88**,12 (2008). DOI: 10.1080/14786430802206482.

[31] M. Mendelev et al. Development of suitable interatomic potentials for simulation of liquid and amorphous Cu-Zr alloys. *Philosophical Magazine* **89**,11 (2009). DOI: 10.1080/14786430902832773.

[32] M. I. Mendelev et al. Development of interatomic potentials appropriate for simulation of liquid and glass properties of nizr2 alloy. *Philosophical Magazine* **92**,35 (2012). DOI: 10.1080/14786435.2012.712220.

[33] Y. Zhang et al. Experimental and molecular dynamics simulation study of structure of liquid and amorphous Ni62Nb38 alloy. *The Journal of Chemical Physics* **145**,20 (2016). DOI: 10.1063/1.4968212.

[34] H. W. Sheng et al. Highly optimized embedded-atom-method potentials for fourteen FCC metals. *Physical Review B - Condensed Matter and Materials Physics* **83**,13 (2011). DOI: 10.1103/PhysRevB.83.134118.

[35] L. Zhong et al. Formation of monatomic metallic glasses through ultrafast liquid quenching. *Nature* **512**,7513 (2014). DOI: 10.1038/nature13617.

[36] M. I. Mendelev, T. L. Underwood, and G. J. Ackland. Development of an interatomic potential for the simulation of defects, plasticity, and phase transformations in titanium. *Journal of Chemical Physics* **145**,15 (2016). DOI: 10.1063/1.4964654.

[37] M. I. Mendelev and G. J. Ackland. Development of an interatomic potential for the simulation of phase transformations in zirconium. *Philosophical Magazine Letters* **87**,February 2012 (2007). DOI: 10.1080/09500830701191393.

[38] A. Hirata et al. Geometric frustration of icosahedron in metallic glasses. *Science (New York, N.Y.)* **341**,July (2013). DOI: 10.1126/science.1232450.

Chapter 5: A Possible Structural Signature of the Onset of Cooperativity in Metallic Liquids

This chapter has been published in The Journal of Chemical Physics in collaboration with R. Dai and K. F. Kelton [1] and has been adapted to be consistent with the formatting for this dissertation. The author's contributions include reduction of some scattering data, programming and creation of analysis techniques for determining T_A, and determination of initial correlation for a small subset of the examined data. A majority of the writing and final analysis was performed by R. Dai. The scattering data was collected during BESL2016 with the help of C.E. Pueblo, D. Van Hoesen, M. Sellers, N. A. Mauro, A. K. Gangopadhyay and S. Chen.

5.1 Introduction

Upon cooling, all liquids show an astounding increase in the shear viscosity, changing by more than 15 orders of magnitude from its value at the melting temperature to that at the glass transition temperature, T_g. Of basic interest is the existence of a crossover temperature for the shear viscosity near the liquidus temperature. While the viscosity has an Arrhenius temperature dependence at high temperature [2, 3], this changes to super-Arrhenius behavior with decreasing temperature. The temperature at which this crossover occurs is defined as T_A (see Fig 5.1). Recent molecular dynamics simulations suggest that this corresponds to the temperature at which structural rearrangements become cooperative [4, 5]. Above T_A, rearrangements within individual clusters are independent of surrounding clusters. Below T_A, the atoms "communicate" beyond nearest neighbors, with multiple clusters beginning to rearrange cooperatively in the liquid's response to shear [6]. Molecular dynamics simulations

and experimental data suggest that T_A is the starting point for the glass transition. The transition is complete at the glass transition temperature, T_g, which is approximately one-half the value of T_A in metallic liquids [7].

While a correlation between liquid/glass dynamics and structure has been suggested [8–12],the structural changes are typically so small that a clear demonstration of the role of structure in the dynamical crossover remains elusive, but there is some evidence. Fragility is a common measure of liquid dynamics, with "strong" liquids showing an approximately Arrhenius behavior (constant activation energy) from the liquids temperature to T_g and "fragile" liquids showing a sharp increase in the activation energy upon approaching T_g [13]. Recent experimental studies [14] have demonstrated a connection between the rate of structural ordering of the liquids near T_g and the fragility by extrapolating features of the X-ray structure factor, $S(q)$, to T_g. also X-ray scattering measurements as a function of temperature in a $Pd_{42.5}Cu_{30}Ni_{7.5}P_{20}$ liquid [8]suggest a connection between the formation of chemical short-range order and the rapid non-Arrhenius increase in viscosity. Studies in NI-Nb liquids also argue that chemical ordering is correlated with the liquids dynamics [15].

Recent Molecular simulations of $Cu_{64}Zr_{36}$ indicate [6] that the result of the cooperative rearrangements is the growth of extended structural order. They also predict the existence of a structural crossover that underlays the dynamical one. However, no experimental evidence that directly connects the dynamical crossover with a crossover in the length scale of structural ordering exists.

In the present study, experimental evidence is presented for a structural crossover underlying the dynamical one in several metallic liquids. The dynamical crossover temperature, T_A, was determined from the viscosity measurements using the Washington University Beamline Electrostatic Levitator (WU-BESL) [16].Structural ordering beyond nearest neighbors is reflected in the acceleration of the growth in intensity of a low-q sub-peak in the second peak of the liquid structure factor, obtained from high-energy X-ray scattering studies using WU-BESL at the Advanced Photon Source. The results presented strengthen the validity of

a connection between the structure and dynamics in liquids and offer the first experimental evidence of the MD predictions for a growing length scale for structural ordering and the super-Arrhenius behavior of the shear viscosity.

5.2 Experimental Procedure

Master ingots of the desired alloy compositions of approximately 1 g each were prepared by arc-melting high-purity elements in the proper ratio on a water-cooled hearth in a high-purity (99.999%) Ar environment. A Ti-Zr getter located close to the alloy was first melted to further reduce the oxygen concentration in the chamber. To ensure a homogeneous composition of the ingot, the ingot was flipped and re-melted, a process that was repeated four times. The mass loss during alloy melting was controlled to less than 0.1% to ensure proper composition. Any ingots having a greater mass loss were discarded. Samples for ESL processing (30-60 mg) were prepared by re-melting portions of the master ingots.

The containerless processing environment of WU-BESL eliminates the sources of heterogeneous nucleation from a container. This allows the liquids to be cooled considerably below their melting temperatures (supercooled) before crystallization occurs [16] making physical property measurements of the supercooled liquids possible. The ESL samples (2.0-4.0 mm in diameter) were levitated under high vacuum (10^{-7} Torr) using three pairs of orthogonal electrodes and electrostatic fields of 0-2.5 MV m^{-1} [16] The location of the levitated sample was tracked from the shadow of a back-lit sample [using two orthogonal high-intensity light-emitting diodes (LEDs)] onto two orthogonal position sensitive detectors (PSDs). Using this information, the voltages of the electrodes were adjusted to maintain the position of the sample using a gain-scheduled control algorithm [16]. During the experiment, the sample was heated by a 50 W diode laser. The temperature of the sample was measured by a Process Sensors Metis MQ22 two-color ratio pyrometer, using wavelengths of 1.40 and 1.64 µm [17]. The temperatures were calibrated by matching the uncorrected solidus temperature to the

sample's true solidus temperature as determined by DTA [17]. A more detailed discussion of WU-BESL can be found elsewhere [16].

The viscosity of the supercooled liquids was measured as a function of temperature using the oscillating drop technique [18]. A small sinusoidal voltage signal was added to the vertical levitation voltage to modulate the levitation field near the liquid's resonant frequency, inducing a $l = 2$ spherical harmonic mode of the liquid sample. After the driving signal was removed, the sample surface acted as an underdamped harmonic oscillator, with a decay constant (τ) inversely proportional to the viscosity (η) [19] by

$$\eta = \frac{\rho r^2}{5\tau} \tag{5.1}$$

where ρ is the sample density and r is the radius. The volume of the sample was also measured as a function of temperature using a digital monochrome camera to record the image of a back-lit sample (using a high intensity LED) through a telocentric lens [20]. Knowing the mass of the sample, the density is readily obtained as a function of temperature.

High-energy X-ray (E =131.7 keV,λ =0.094 114 9 Å) scattering data were obtained in a transmission geometry from levitated liquids to a momentum transfer, q, of 15 Å, using a GE Revolution 41-RT amorphous Si flat-panel X-ray detector. Diffraction patters were measured during isothermal holds over a wide temperature range; scattering data were collected for 15-20 s at each temperature step. The sample to detector distance, tilt angle, and detector center were calibrated using polycrystalline Si samples placed at the same position as the levitated sample. The scattering data were processed by applying a pixel efficiency gain map, masking bad pixels, averaging the images during the isothermal holds, and subtracting the detector dark current and scattering background [21]. The images were corrected [21, 22] for sample geometry, polarization, absorption, Compton scattering contributions, fluorescence, oblique incidence, inelastic scattering, and multiple scattering using in-house analysis

packages written in LabVIEW. The total structure factors were calculated using

$$S(q) = \frac{I(q) - \sum_{i=1}^{n} c_i |f_i(q)|^2}{|\sum_{i=1}^{n} c_i f_i(q)|^2} + 1 \tag{5.2}$$

where $I(q)$ is the corrected diffraction intensity, c_i is the atomic fraction of each species, and $f_i(q)$ is the q-dependent atomic form factor for each species. The sums were taken overall species and an isotropic and statistically homogeneous atomic distribution was assumed.

5.3 Results and Discussion

Following the procedure outlined in the section title Experimental Procedure, the viscosity was measured as a function of temperature for a range of metallic liquids. The highest temperature for which viscosity measurements could be made were limited by the vapor pressures of the samples and the ability to excite only the $l = 2$ mode [23], while the lowest temperature were limited by the ability to excite oscillations in the sample. The high-temperature viscosities of all the liquids measured followed an Arrhenius temperature dependence. This changed to a super-Arrhenius dependence as the liquids was supercooled, in agreement with the results from precious studies [7, 24, 25].

Since the crossover from Arrhenius to super-Arrhenius behavior is gradual, determining the temperature (T_A) where this first begins to happen is difficult. A universal curve [7] model was recently proposed to fit the viscosity of a wide range of metallic liquids and to allow a determination of T_A. However, this uses the viscosity data for Vit106a to determine the functional form of the curve for other metallic liquids, which may not be correct. Also, the determination of some of the parameters in the model is somewhat subjective. Here, we introduce a model-independent approach to determine T_A. The viscosity data were first sorted by their temperature values (from highest to lowest) and the logarithm of the viscosity was plotted as a function of inverse temperature. The linearity of these reduced data was then tracked by the R^2 value of a linear fit as low temperature data points were removed from the

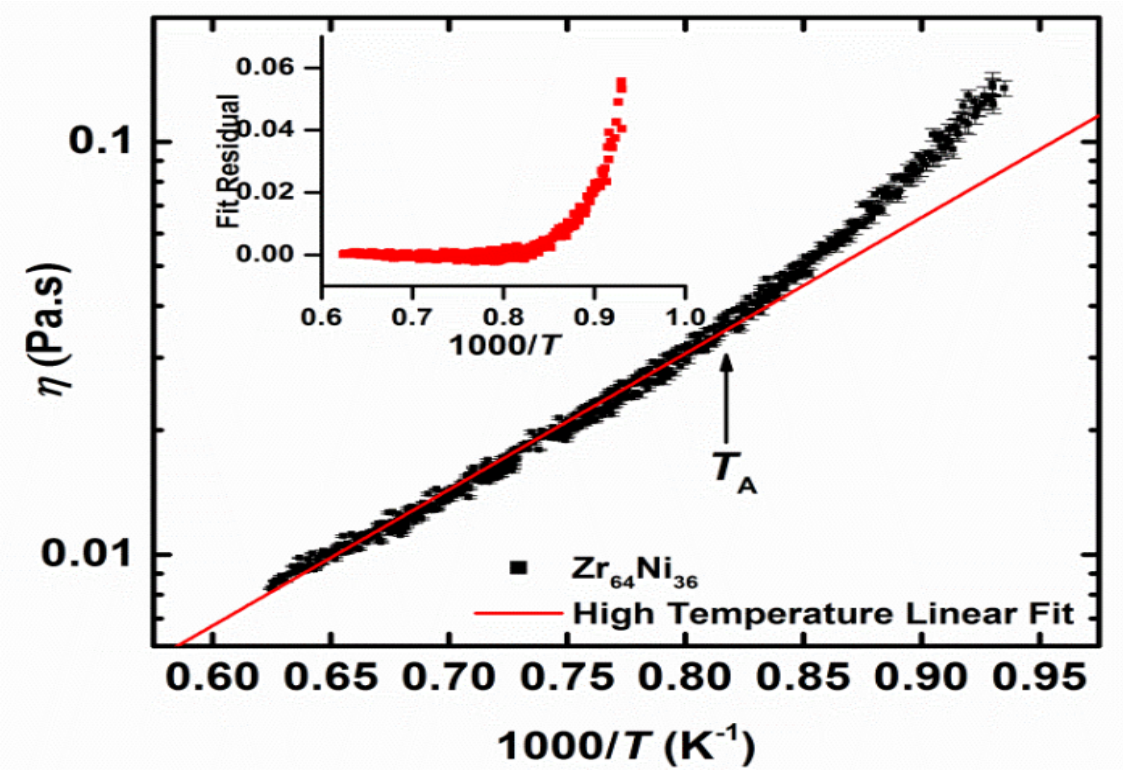

Figure 5.1: Typical example of the behavior of liquid viscosity data, on a log-scale, as a function of inverse temperature, showing a departure from Arrhenius behavior on cooling below T_A. The inset shows the fit residual. Reproduced with permission from [7]. Copyright 2015 Springer Nature.

fit. As observed in the inset of Fit. 5.1, the R^2 value increases as the low temperature viscosity data points are sequentially removed. If the Arrhenius crossover temperature is within the temperature range of the fit, R^2 should either go through a maximum or approach a limiting value (≈ 1). Typically, the R^2 goes through a maximum because of the variance of the viscosity data in the Arrhenius region. The point at which a maximum occurs or a limiting value is reached is defined to be T_A. To both estimate the error in T_A and incorporate the error in our viscosity measurements, a resampling method was employed. Each data point is assumed to be the average of a Gaussian distribution with a full width at half maximum that is proportional to the error in the viscosity. A resampled version of the data is extracted from these distributions and then binned so that it can be analyzed by the method just described. Carrying out this procedure many time(≈ 7500) gives a distribution of T_A values. From this distribution, a mean and standard deviation are calculated to be used as the measured value and standard error of T_A, respectively. This is illustrated in Fig. 5.2 for a $Zr_{56}Co_{28}Al_{16}$ liquid. The T_A distribution is shown in red in the same plot. The method used is closely related to a block bootstrapping routine.

As mentioned earlier, recent studies suggest that the crossover behavior in the viscosity is correlated with a growing structural length scale in the liquid. To investigate this, structural changes in the liquids were measured as a function of temperature from high-energy X-ray scattering experiments. The scattering data were collected during isothermal holds from $\sim$200 K above their respective liquidus temperatures down to temperatures at which the samples crystallized. As for the viscosity measurements, the highest temperatures were limited by the vapor pressure of the sample. However, the lowest temperature for collecting scattering data was limited by the time to crystallize, not the magnitude of the viscosity. This allowed structural studies to be made on more deeply supercooled liquids than was possible for viscosity measurements. The total structure factors were derived from the scattering data following the procedure outlined in the section title Experimental Procedure. As expected, the peaks in $S(q)$ sharpened and grew in intensity with decreasing temperature, reflecting

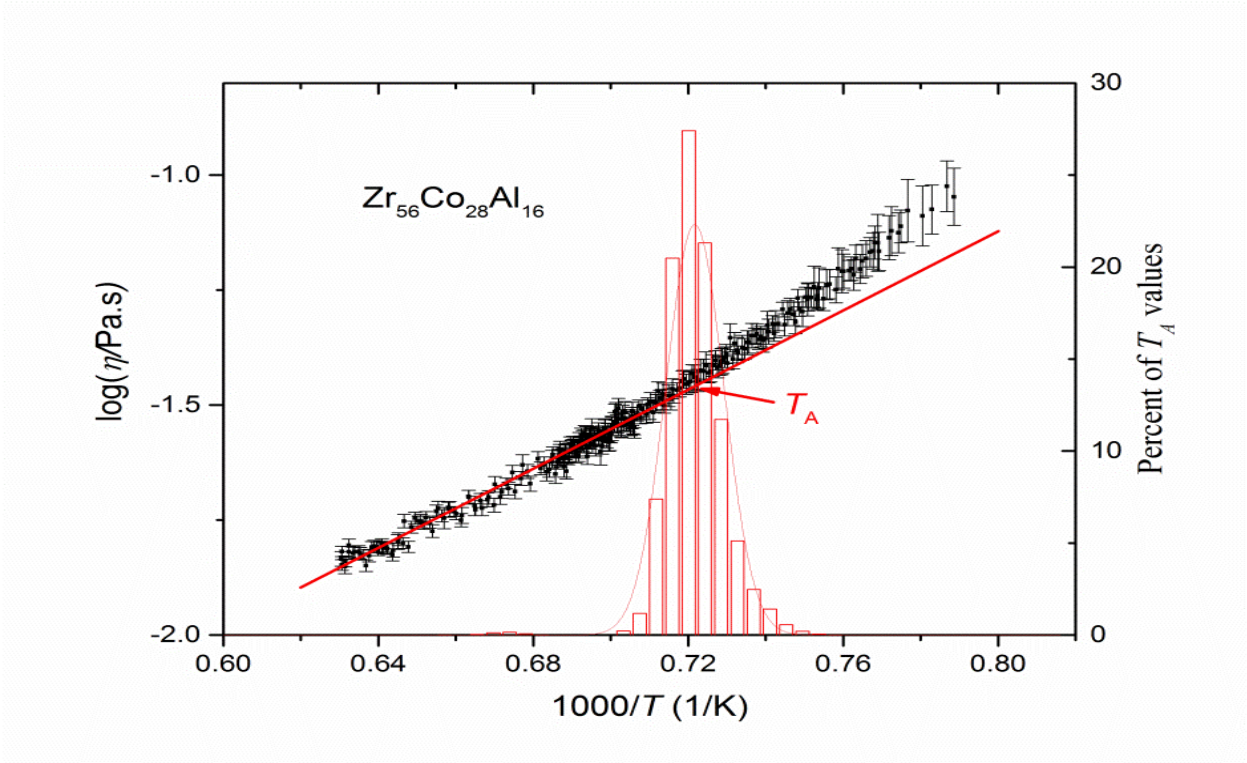

Figure 5.2: Typical data of the logarithm of the high-temperature viscosity as a function of inverse temperature (black solid squares, error bars are one standard deviation), showing a deviation from an Arrhenius temperature dependence below T_A, as well as the distribution of T_A (red histogram).

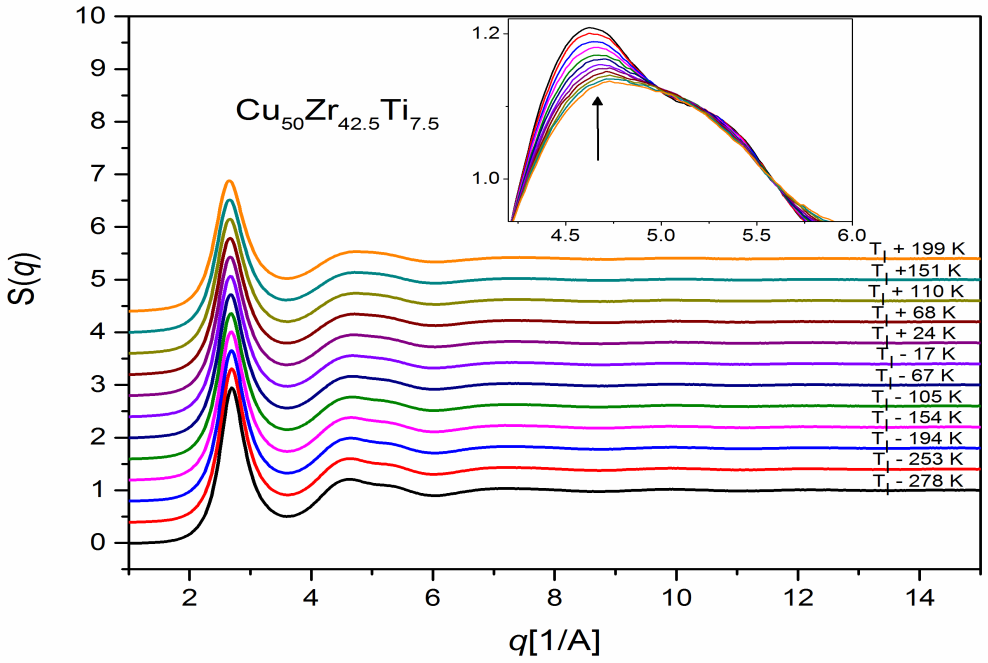

Figure 5.3: Structure factors of the equilibrium and supercooled $Cu_{50}Zr_{42.5}Ti_{7.5}$ liquid (T_l =1152 K). The inset shows the development of the low-q feature in the second peak with decreasing temperature.

an overall ordering of the liquid. Of particular note is the second peak of $S(q)$ [designated as $S_2(q)$ from here on] which develops a feature on the low-q side of the peak with decreasing temperature, causing the peak to appear as two overlapping peaks (for a typical example see Fig. 5.3.

Earlier MD studies have indicated that the onset of super-Arrhenius behavior in the viscosity is due to the growth of the ordering in the liquid [4]. The intensity data for the low-q and high-q sub-peaks in $S_2(q)$ was fit using two Gaussian functions (see the supplementary material), representing two overlapping peaks. As shown in Fit 5.4, this fitting procedure gives a good representation of the growth of the two features in the experimental data. taking the $Cu_{50}Zr_{45}Al_5$ liquid as an example (Fig 5.5) in the high-temperature liquid, the amplitude of the low-q sub-peak increases linearly with decreasing temperature but begins to accelerate below a specific crossover temperature (here designated as T_S). Although the

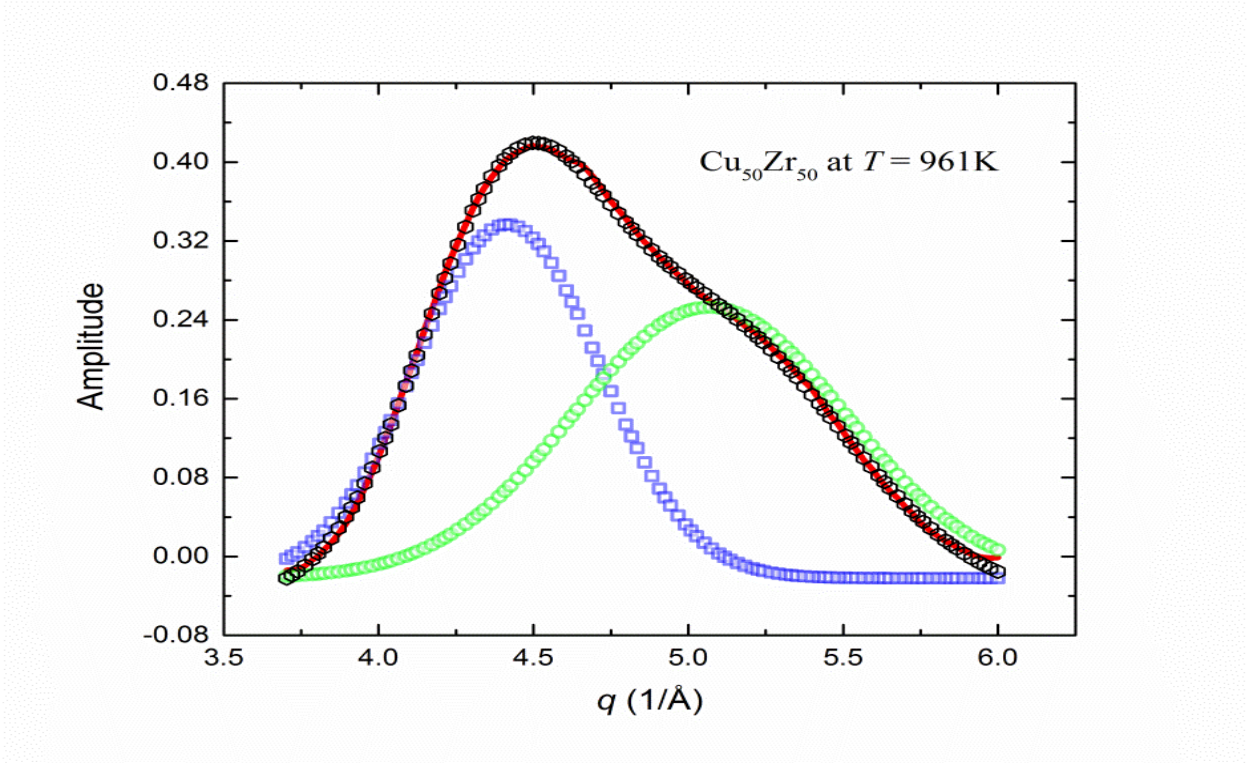

Figure 5.4: Typical example of the fits of the low-q and high-q sub-peaks to the second peak of the liquid structure factor, $S_2(q)$/ The two Gaussian sub-peaks are indicated (blue squares for the low-q sub-peak and green circles for the higher-q sub-peak). The red line is the corrected $S_2(q)$, with the baseline and offset obtained from the fits to the two Gaussian sub-peaks subtracted; the fit to this is shown by the black hexagonal symbols.

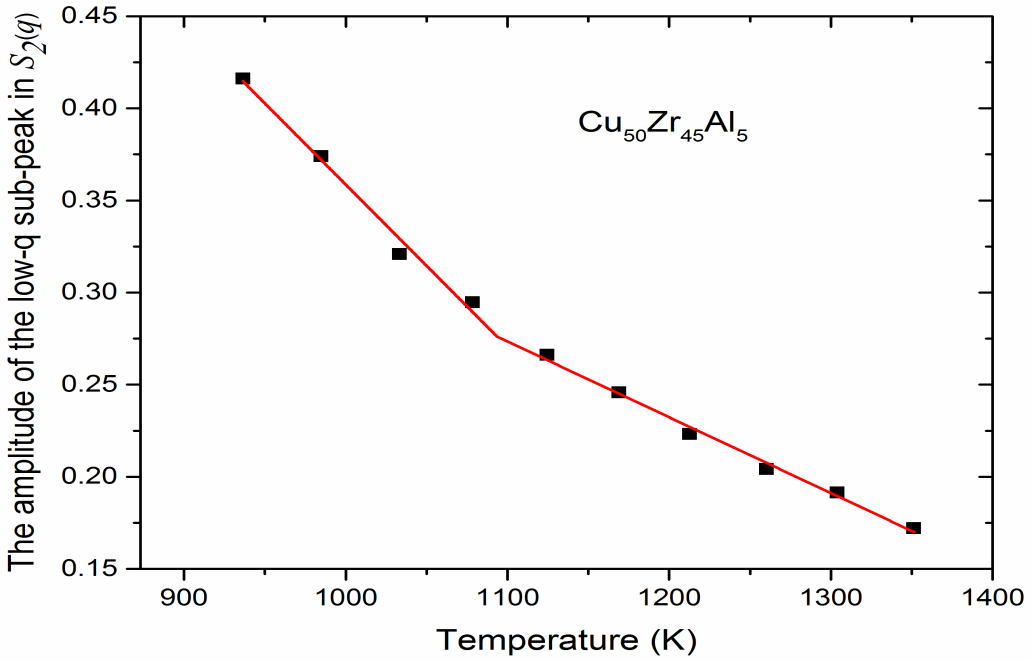

Figure 5.5: The intensity of the low-q sub-peak in $S_2(q)$ (solid black squares) as a function of temperature showing an acceleration below T_S, which is determined by the piecewise linear function (red line).

temperature dependence of the amplitude below T_S is not linear over a wide temperature range, it is approximately linear over a small temperature range near T_S. As shown in Fig 5.5, then, piecewise linear functions can be used to provide reasonable values for the crossover temperature. While the combined error for the values obtained include errors in the calculation of the total structure factor from the scattering data, the fitting of $S_2(q)$ using two Gaussian functions, and the determination of the crossover temperature with two piecewise linear functions, the large temperature interval between the isothermal holds is usually the dominant error in determining T_S.

Figure 5.6 shows the correlation between the values of T_A, and T_S (determined from the procedure described in the previous section) for several different metallic alloy liquids. Clearly T_A and T_S are strongly correlated, with the slope of a linear fit to these data equal to 0.93 ± 0.17. While the large amount of data as a function of temperature allowed T_A

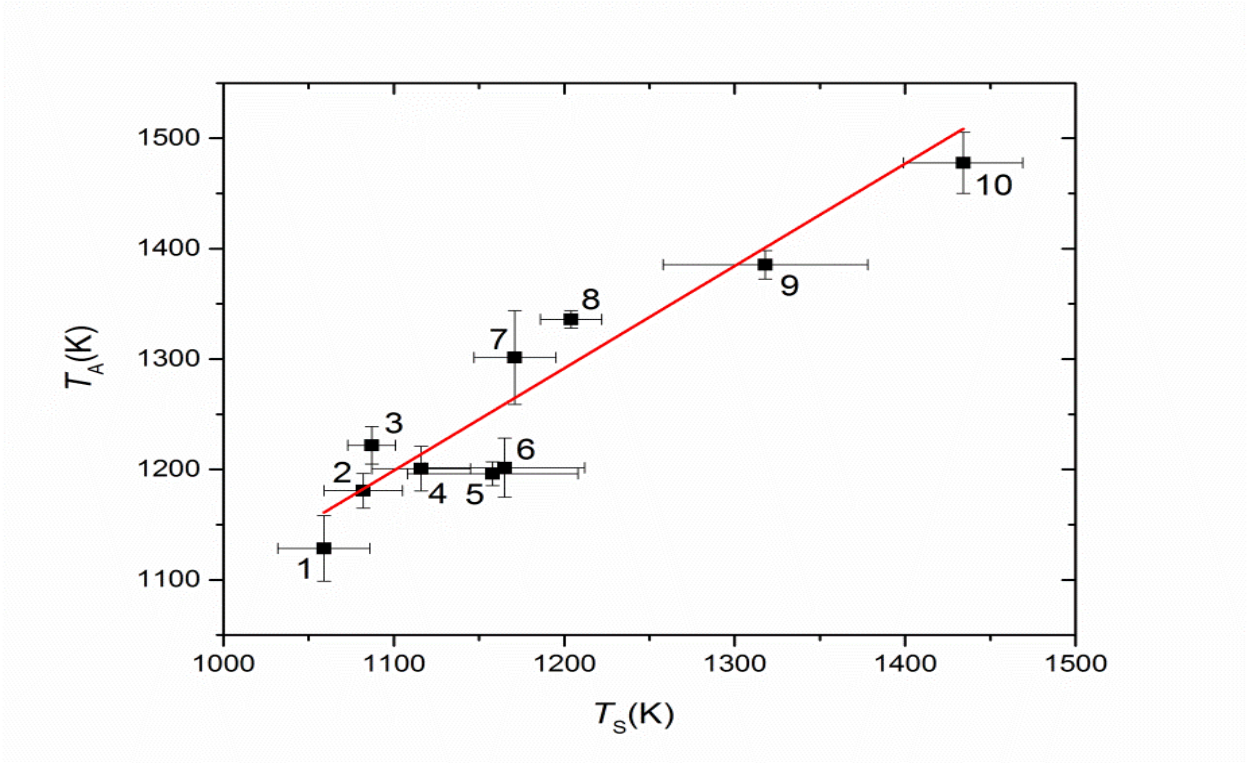

Figure 5.6: The correlation between the crossover temperature (T_S)obtained from measurements of the growth in intensity of the low-q sub-peak in $S_2(q)$ and that obtained from the viscosity measurements (T_A). The alloy compositions corresponding to the numbers are $Cu_{46}Zr_{54}$ (1),$Cu_{50}Zr_{42.5}Ti_{7.5}$ (2), $Cu_{50}Zr_{45}Al_5$ (3), $Cu_{50}Zr_{40}Ti_{10}$ (4), $Cu_{50}Zr_{50}$ (5), $Cu_{64}Zr_{36}$ (6), LM601 (7), Vit105 (8), $Zr_{56}Co_{28}Al_{16}$ (9), and $Zr_{82}Ir_{18}$ (10).

to be obtained from the viscosity following the procedure discussed earlier, this was not possible for T_S due to the fewer temperature data for the X-ray diffraction studies. However, fitting the viscosity data using two piecewise linear functions gave nearly the same correlation between T_A and T_S as shown in Fig. 5.6. This significant correlation suggest that the onset of an accelerated growth of the amplitude of the low-q sub-peak in $S_2(q)$ with decreasing temperature is a structural signature of T_A.

It should be pointed out, however, that although T_A and T_S clearly are correlated, the magnitude of T_S is always a little lower than the T_A obtained from viscosity data. At this time, the reasons for this are not clear, The differences may arise because the viscosity is very sensitive to structural changes, with the viscosity varying by over 15 orders of magnitude from the liquidus temperature to T_g. Although the viscosity data discussed here were measured

over a narrower temperature range, their values still increased by more than one order of magnitude. By comparison, the measured structure changes are very small across the accessible supercooled temperature range [26],making it difficult to determine a deviation in the linear evolution of the structure with temperature until it is sufficiently far below the T_A value obtained from the viscosity measurements. It was possible to observe these changes at all is due to the use of containerless processing and a high-intensity synchrotron X-ray source. The lack of a container greatly increased the signal-to-noise level in the scattering experiments and limited the influence of heterogeneous nucleation, allowing measurement to be made to deeper supercooling.

Similar features in $S_2(q)$ were identified in earlier studies of a $Ti_{39.5}Zr_{39.5}Ni_{21}$ liquid [27]. The analysis of those data assumed that icosahedral clusters were dominant in establishing the local order of the liquid. The high-q feature was identified as arising from the center-to-vertex bonds (nearest-neighbor bonds), and the low-q feature was identified as arising from the vertex-to-vertex bonds (next-nearest-neighbor bonds). Since the intensity of the high-q feature increased little with decreasing temperature, it was argued that the nearest-neighbor bonds were already established at very high temperatures. Since Ni populated the centers of the clusters with Ti/Zr on the vertices, this was reasonable given the strong bonding of Ti/Zr with Ni. With decreasing temperature, the number of next-nearest-neighbor bonds increased, causing the growth of the low-q feature. Like the experimental studies of the $Ti_{39.5}Zr_{39.5}Ni_{21}$ liquid, MD studies of Cu-Zr liquids and glasses show that the fundamental clusters have an icosahedral or icosahedral-like symmetry [28–31]. These conclusions are also in agreement with the results of RMC fit for $Cu_{46}Zr_{54}$ liquids [32], which showed that the next-nearest-neighbor ordering accelerates with decreasing temperature and is associated with an increasing intensity of the low-q side of $S_2(q)$. By contrast, the high-q side is only weakly temperature dependent. Another MD study of $Cu_{64}Zr_{36}$ shows that the cooperative rearrangements that began at T_A induce the growth of domains of locally preferred structure (LPS)s, establishing connections between isolated clusters [6].

All of these studies focused on a dominant icosahedral cluster. Detailed studies of X-ray and neutron scattering data for metallic liquids (see $Zr_{80}Pt_{20}$ and $Zr_{77}Rh_{23}$ as two examples [22]) have shown that the liquid structure is often characterized by several local cluster types, not all of which have icosahedral symmetry. However, the general conclusion reached in the experimental and MD studies remains. Regardless of the cluster symmetry, the low-q feature emerges from ordering beyond the nearest-neighbors [27, 33–35]. It is likely that at T_A the cooperative rearrangements prefer the connection of the LPSs, as was shown in $Cu_{64}Zr_{36}$. Above T_A, the rearrangement within the LPS is sufficient to relax the liquid [4, 5]. Below T_A, the LPSs act cooperatively [4, 5]. The rearrangements of larger regions of the liquid with decreasing temperature increase the activation energy for flow and manifest as the onset of super-Arrhenius behavior in the viscosity [6]. Based on the MD studies in $Cu_{64}Zr_{36}$, with decreasing temperature, the coherence length of the ordered regions increases, eventually leading to a percolation of the LPSs that results in the glass transition. In a real sense, then, the process that leads to the glass transition starts at T_A, which for metallic liquids is approximately $2T_g$ [7].

The growing amplitude of the low-q feature in $S_2(q)$, signaling order growing beyond the nearest neighbors, is the first experimental evidence of the structural signature of the dynamical crossover at T_A predicted by MD studies of metallic liquids. This lends validity to the MD predictions and more generally establishes a strong connection between the structure and dynamics.

5.4 Summary and Conclusions

In summary, a possible structural signature of the dynamical crossover in metallic liquids at high temperature was experimentally confirmed based on coordinated shear viscosity measurements and high-energy X-ray scattering experiments. From the viscosity data, the dynamical crossover at T_A was determined by the change from Arrhenius to super Arrhenius

temperature dependence. Upon cooling, a low-q feature develops in the second peak of the static structure factor $S(q)$, which indicates ordering beyond nearest neighbors. Like the viscosity, the rate of increase in amplitude of this feature has a crossover behavior at a temperature T_S. The strong correlation between T_A and T_S is the experimental evidence for the connection between structural ordering and the dynamical behavior in the supercooled liquids and provides the first confirmation of recent predictions from molecular dynamics studies. Why the structural crossover occurs at a lower temperature than the dynamical crossover is not totally clear. It may simply be due to the difficulty of measuring the very small changes in structure that accompany the larger dynamical changes. However, this needs further study, addressing questions of the possible universality of the difference, the effect of cooling rate, etc.

5.5 References

[1] R. Dai, R. Ashcraft, and K. Kelton. A possible structural signature of the onset of cooperativity in metallic liquids. *The Journal of Chemical Physics* **148**,20 (2018). DOI: 10.1063/1.5026801.

[2] D. Kivelson et al. A thermodynamic theory of supercooled liquids. *Physica A: Statistical Mechanics and its Applications* **219**,1-2 (1995). DOI: 10.1016/0378-4371(95)00140-3.

[3] C. A. Angell. Formation of Glasses from Liquids and Biopolymers. *Science* **267**,5206 (1995). DOI: 10.1126/science.267.5206.1924.

[4] T. Iwashita, D. M. Nicholson, and T. Egami. Elementary Excitations and Crossover Phenomenon in Liquids. *Physical Review Letters* **110**,20 (2013). DOI: 10.1103/PhysRevLett.110.205504.

[5] S. P. Chen, T. Egami, and V. Vitek. Local fluctuations and ordering in liquid and amorphous metals. *Physical Review B* **37**,5 (1988). DOI: 10.1103/PhysRevB.37.2440.

[6] R. Soklaski et al. A locally preferred structure characterises all dynamical regimes of a supercooled liquid. *Philosophical Magazine* **96**,12 (2016). DOI: 10.1080/14786435.2016.1158427. arXiv: 1502.01739.

[7] M. E. Blodgett et al. Proposal for universality in the viscosity of metallic liquids. *Scientific Reports* **5**, (2015). DOI: 10.1038/srep13837.

[8] D. V. Louzguine-Luzgin et al. Structural basis for supercooled liquid fragility established by synchrotron-radiation method and computer simulation. *Journal of Applied Physics* **110**,4 (2011). DOI: 10.1063/1.3624745.

[9] A. Gangopadhyay and K. Kelton. Recent progress in understanding high temperature dynamical properties and fragility in metallic liquids, and their connection with atomic structure. *Journal of Materials Research* **32**,14 (2017). DOI: 10.1557/jmr.2017.253.

[10] K. F. Kelton. Kinetic and structural fragility-a correlation between structures and dynamics in metallic liquids and glasses. *Journal of Physics: Condensed Matter* **29**,2 (2017). DOI: 10.1088/0953-8984/29/2/023002.

[11] C. P. Royall and S. R. Williams. The role of local structure in dynamical arrest. *Physics Reports* **560**, (2015). DOI: 10.1016/j.physrep.2014.11.004. arXiv: 1405.5691.

[12] J. Ding et al. Short-range structural signature of excess specific heat and fragility of metallic-glass-forming supercooled liquids. *Physical Review B - Condensed Matter and Materials Physics* **85**,6 (2012). DOI: 10.1103/PhysRevB.85.060201.

[13] C. A. Angell. Strong and Fragile Liquids. *Relaxations in Complex Systems* **22161**,3 (1985).

[14] N. A. Mauro and K. F. Kelton. A highly modular beamline electrostatic levitation facility, optimized for in situ high-energy x-ray scattering studies of equilibrium and supercooled liquids. *Review of Scientific Instruments* **82**,3 (2011). DOI: 10.1063/1.3554437.

[15] D. Holland-Moritz et al. Structural aspects of glass-formation in Ni-Nb melts. *Journal of Applied Physics* **115**,20 (2014). DOI: 10.1063/1.4878921.

[16] N. A. Mauro et al. Short- and medium-range order in $Zr_{80}Pt_{20}$ liquids. *Physical Review B* **83**,18 (2011). DOI: 10.1103/PhysRevB.83.184109.

[17] J. C. Bendert et al. Temperature Calibration for Optical Pyrometry in Containerless Systems Using Differential Scanning Calorimetry: Application to $Cu_{100-x}Zr_x$ $x = 45 - 50$). *International Journal of Thermophysics* **35**,9-10 (2014). DOI: 10.1007/s10765-014-1660-y.

[18] W.-K. Rhim et al. Noncontact technique for measuring surface tension and viscosity of molten materials using high temperature electrostatic levitation. *Review of Scientific Instruments* **70**,6 (1999). DOI: 10.1063/1.1149797.

[19] H. Lamb. On the Oscillations of a Viscous Spheroid. *Proceedings of the London Mathematical Society* **s1-13**,1 (1881). DOI: 10.1112/plms/s1-13.1.51.

[20] J. C. Bendert and K. F. Kelton. Containerless Measurements of Density and Viscosity for a Cu $$_{48}$$ 48 Zr $$_{52}$$ 52 Liquid. *International Journal of Thermophysics* **35**,9-10 (2014). DOI: 10.1007/s10765-014-1664-7.

[21] J. C. Bendert, N. A. Mauro, and K. F. Kelton. Pair distribution function analysis of X-ray diffraction from amorphous spheres in an asymmetric transmission geometry: Application to a Zr 58.5Cu15.6Ni12.8Al10.3Nb 2.8 glass. *Journal of Applied Crystallography* **46**,4 (2013). DOI: 10.1107/S0021889813013162.

[22] M. L. Johnson et al. Measurements of structural and chemical order in Zr80Pt20 and Zr77Rh23 liquids. *Physical Review B* **93**,5 (2016). DOI: 10.1103/PhysRevB.93.054203.

[23] M. E. Blodgett. Thermophysical Properties and Structural Evolution of Supercooled Metallic Liquids. PhD thesis. Washington University in St. Louis, 2015.

[24] G. Tarjus et al. Disentangling density and temperature effects in the viscous slowing down of glassforming liquids. *Journal of Chemical Physics* **120**,13 (2004). DOI: 10.1063/1.1649732. arXiv: 0309579 [cond-mat].

[25] D. Kivelson et al. Fitting of viscosity: Distinguishing the temperature dependences predicted by various models of supercooled liquids. *Physical Review E* **53**,1 (1996). DOI: 10.1103/PhysRevE.53.751.

[26] A. Cavagna. Supercooled liquids for pedestrians. *Physics Reports* **476**, (2009). DOI: 10.1016/j.physrep.2009.03.003. arXiv: 0903.4264.

[27] G. W. Lee et al. Local structure of equilibrium and supercooled Ti-Zr-Ni liquids. *Physical Review B - Condensed Matter and Materials Physics* **77**,18 (2008). DOI: 10.1103/PhysRevB.77.184102.

[28] G. Duan et al. Molecular dynamics study of the binary Cu46Zr54 metallic glass motivated by experiments: Glass formation and atomic-level structure. *Physical Review B - Condensed Matter and Materials Physics* **71**, (2005). DOI: 10.1103/PhysRevB.71.224208.

[29] J. Antonowicz et al. Icosahedral order in Cu-Zr amorphous alloys studied by means of X-ray absorption fine structure and molecular dynamics simulations. *Philosophical Magazine* **92**,15 (2012). DOI: 10.1080/14786435.2012.659008.

[30] Y. Q. Cheng, H. W. Sheng, and E. Ma. Relationship between structure, dynamics, and mechanical properties in metallic glass-forming alloys. *Physical Review B - Condensed Matter and Materials Physics* **78**,1 (2008). DOI: 10.1103/PhysRevB.78.014207.

[31] G. A. Almyras et al. On the microstructure of the Cu65Zr35 and Cu35Zr65 metallic glasses. *Scripta Materialia* **62**,1 (2010). DOI: 10.1016/j.scriptamat.2009.09.019.

[32] V. Wessels et al. Rapid chemical and topological ordering in supercooled liquid Cu46Zr54. *Physical Review B* **83**,9 (2011). DOI: 10.1103/PhysRevB.83.094116.

[33] S. Sachdev and D. R. Nelson. Order in metallic glasses and icosahedral crystals. *Physical Review B* **32**,7 (1985). DOI: 10.1103/PhysRevB.32.4592.

[34] S. Sachdev and D. R. Nelson. Theory of the structure factor of metallic glasses. *Physical review letters* **53**,20 (1984). DOI: 10.1103/PhysRevLett.53.1947.

[35] D. Holland-Moritz et al. Short-range order in undercooled melts forming quasicrystals and approximants. *Journal of Alloys and Compounds* **342**,1-2 (2002). DOI: 10.1016/S0925-8388(02)00142-1.

Chapter 6: Experimental determination of the temperature-dependent Van Hove function in a $Zr_{80}Pt_{20}$ liquid

This chapter has been published on the arXiv [1] in collaboration with Z. Wang, D. L. Abernathy, T. Egami, and K. F. Kelton and has been submitted to a peer-reviewed journal. It has been adapted to be consistent with the formatting in this dissertation. The author's major contributions include performing the Molecular Dynamics (MD) simulations, devising and programming analysis techniques, and collecting inelastic neutron scattering (INS) data. All authors contributed to devising analysis techniques and in drafting the results.

6.1 Introduction

The viscosity, η, of liquids shows common behavior among various disparate groups of liquids [2]. At high temperatures it follows an Arrhenius temperature dependence with a constant activation energy. But below a certain temperature, the viscosity crossover temperature, T_A, it becomes super-Arrhenius. Kivelson [3] first showed that the viscosity of various liquids can be scaled into one curve as a function of T/T_A ($T_A = T^*$ in their work). T_A is also the temperature below which the mode-coupling becomes appreciable [4, 5]. The fundamental time-scale for viscosity is the Maxwell relaxation time, $\tau_M = \eta/G_\infty$, where G_∞ is the infinite-frequency shear modulus . Recent molecular dynamics (MD) studies of metallic liquids suggest that for $T > T_A$, τ_M is approximately equal to τ_{LC}, the lifetime of the atomic bond [5–7].

To evaluate this relationship inelastic neutron scattering measurements were made on

liquid $Zr_{80}Pt_{20}$. To access the supercooled state and to avoid contamination all measurements were made with the liquid held in a containerless environment in high vacuum using the Neutron Electrostatic Levitator (NESL) facility [8] located at the Spallation Neutron Source (SNS). The results were converted into the time-dependent pair-distribution function, i.e. the Van Hove function [9], $G(r,t)$, which allowed a study of the spatial and temporal correlations of the atoms. Due to experimental difficulties, studies of the Van Hove function in the past have been largely limited to computer simulations. Only in a few cases have measurements of $G(r,t)$ been made in metallic liquids at the melting temperature [10], and for water by inelastic x-ray scattering [11, 12]. While τ_{LC} cannot be measured directly from experiment, new MD results discussed here show that it can be related to the decay time of the first peak area in the distinct part of the Van Hove function, $G_d(r,t)$. A comparison of the activation energies of τ_{VH} and τ_M confirms the prediction that both have an Arrhenius temperature dependence and the same activation energy. To our knowledge, this is the first significant experimental evidence indicating that local structural rearrangements underlie the dynamical behavior of high temperature metallic liquids.

6.2 Methods

Measurements of the high temperature properties of liquid metals such as Zr are often plagued by sample reactivity and oxygen contamination. These are minimized by processing the liquids without a container in a high vacuum environment using the technique of electrostatic levitation [13]. The viscosity measurements were made with the Washington University Beamline Electrostatic Levitator (WU-BESL) facility [14]; the experimental methods are discussed elsewhere [15, 16]. Inelastic neutron scattering measurements were made at Oak Ridge National Laboratory (ORNL) on the Wide Angular-Range Chopper Spectrometer (ARCS) [17] beamline at the SNS. The samples were processed in high vacuum using the NESL facility, which is optimized for both elastic and inelastic time-of-flight (TOF) neutron

scattering studies [8]. The TOF inelastic neutron diffraction measurements on the levitated liquid samples were made with the incident energy E_i= 20meV. Due to the kinematic restrictions inherent to inelastic neutron scattering experiments, however, the maximum q range for this incident energy is restricted to $q < 6\text{Å}^{-1}$. Though this restricted q-range can introduce termination ripples in the spatial Fourier transform to obtain the Van Hove correlation function, the increased energy resolution was deemed to be more important for the data needed. The procedure for analyzing the data is only briefly described here; a more detailed description will be given in a future publication.

The MD simulations were performed with the LAMMPS software [18] using the Zr-Pt embedded atom [19] (EAM) potential developed by H. Sheng [20]. The $Zr_{80}Pt_{20}$ system was simulated with 15000 atoms under the NPT ensemble (P=0) with periodic boundary conditions. The Nosé-Hoover thermostat [21, 22] was used to equilibrate the system at a target temperature for 15ns before data collection. The Maxwell time was calculated from the atomic level stress using the Green-Kubo formula (see [23] for example). The method for computing the Van Hove time is the same as for the experimental data which is discussed later. Additional details of the MD simulation are provided in the supplemental material (Appendix D).

6.3 Results and Discussion

The steps to obtain the dynamic structure factor $S(q, E)$ include the conversion of the TOF data to energy and momentum transfer, a physical normalization factor, the assumption of detailed balance and a correction for the resolution of the spectrometer. The initial conversion used a standard reduction routine employing the MANTID [24] software. The required source beam parameters [25] for this reduction were obtained from previous calibration experiments, since they could not be measured in the NESL studies due to the presence of an internal beam-stop. For normalization, the condition that $S(q) \rightarrow 1$ as

$q \to \infty$ was enforced, using the $S(q)$ obtained from the intermediate scattering function, $F(q,t)$. This normalization was checked by comparing the $S(q)$ obtained here with one obtained from earlier neutron and x-ray diffraction data. Detailed balance was used to extend the negative energy transfer data into regions that are inaccessible in the positive energy transfer region. A typical $S(q,E)$ obtained after these corrections is shown in Fig. 6.1a. Since $F'(q,t) = F(q,t)R(t)$, where F' is the measured and F is the true intermediate scattering functions and R is the resolution function, the true intermediate scattering function can be obtained by dividing the measured signal with the resolution function. The resolution function was obtained from inelastic scattering measurements from vanadium at room temperature and was Fourier-transformed to the time domain.

The intermediate scattering function, $F(q,t)$, is obtained by a Fourier transform of $S(q,\omega)$

$$F(q,t) = \int_{-\infty}^{\infty} S(q,\omega) e^{i\omega t} \mathrm{d}\omega \tag{6.1}$$

The self ($F_s(q,t)$) and distinct ($F_d(q,t)$) parts of the intermediate scattering function, which describe single particle and collective density fluctuations respectively, are extracted by assuming that the self-part has a Gaussian form, i.e. $F_s(q,t) = A(t)\exp(-w(t)q^2)$ [10], where the decay parameter, $w(t)$, and the amplitude, $A(t)$ are fitting parameters. The Gaussian approximation comes from expressions for the self-part of the Van Hove correlation function, $G_s(r,t)$, which has a Gaussian dependence in r in both the hydrodynamic and free-particle limits [26, 27]. For intermediate times, which are of interest here, the Gaussian approximation should still be a good approximation [27, 28]. The distinct Van Hove correlation function is obtained from the Fourier transform of $F_d(q,t)$

$$G_d(r,t) - 1 = \frac{1}{2\pi^2\rho} \int_{-\infty}^{\infty} F_d(q,t) \frac{q}{r} \sin(qr) \mathrm{d}q \tag{6.2}$$

where ρ is the number density for the sample. A representative example of $G_d(r,t)$ obtained from the data is shown in Fig. D.1. At $t = 0$, $G_d(r,0)$ is equal to the equal-time (snapshot)

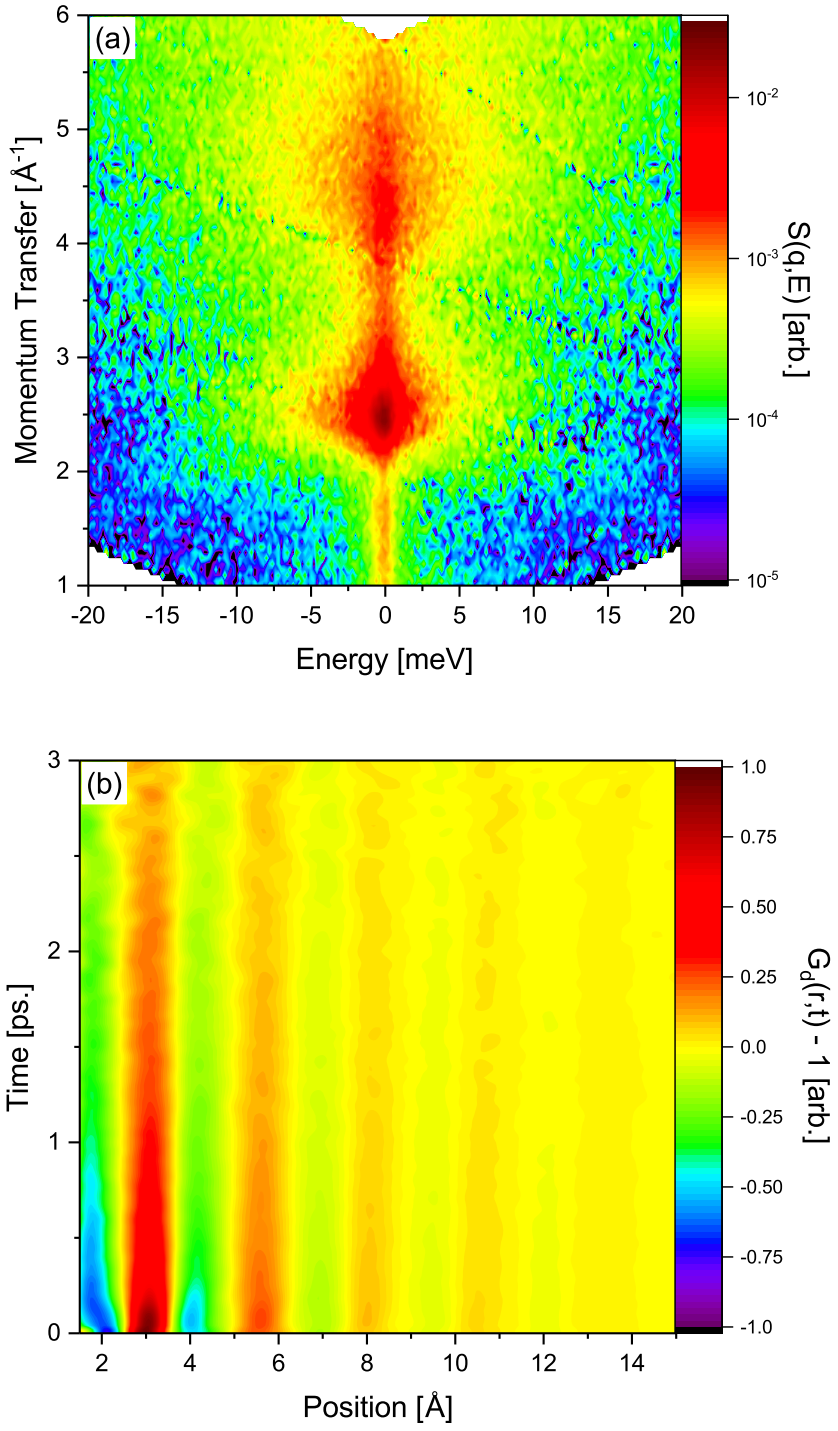

Figure 6.1: Inelastic neutron scattering data for $Zr_{80}Pt_{20}$ at 1833K with $E_i = 20$meV. (a) The dynamic structure factor, $S(q, E)$ correcting for physical normalization ($S(q) \to 1$ as $q \to \infty$) and detailed balance. (b) The distinct Van Hove correlation function, $G_d(r, t) - 1$, with the same corrections and the correction for the resolution function.

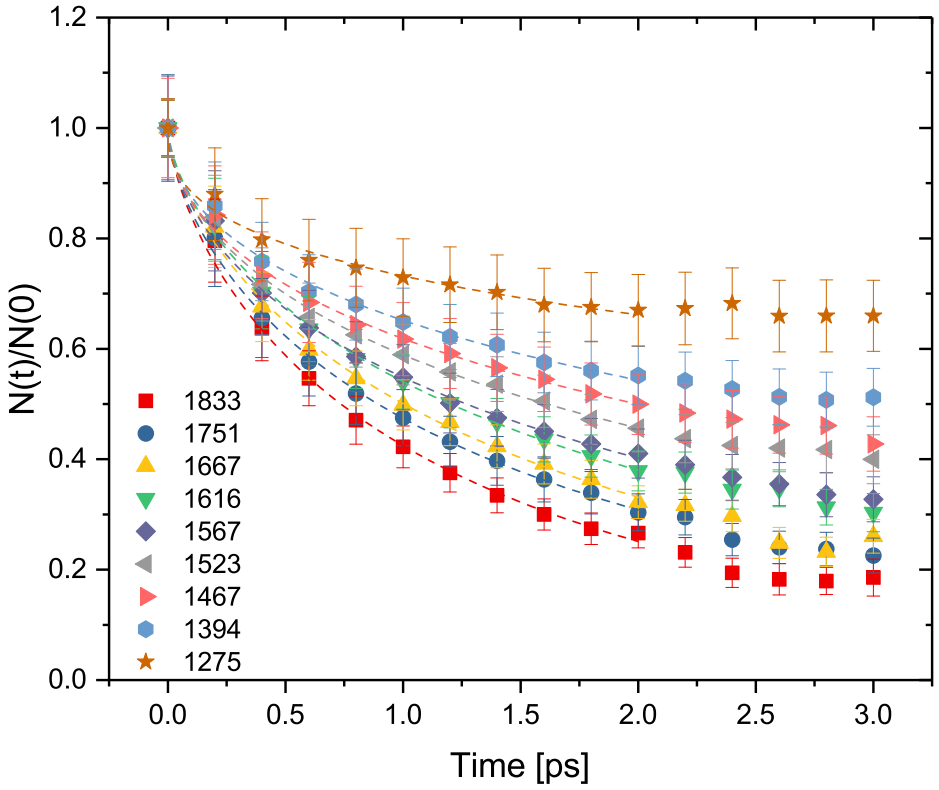

Figure 6.2: (Color online) The normalized integrated peak intensity $N(t)/N(0)$ versus time plotted for each temperature (K). The data is fit (dashed lines) out to 2.0 ps. using the stretched-exponential function (Eq.6.4). For clarity calculated error bars are shown for a select number of times but are representative of errors for all points of a given temperature.

pair-density function, $g(r)$. The integrated peak intensity is computed for each temperature from

$$N(t) = \int_D 4\pi r^2 \rho(G_d(r,t) - 1)\mathrm{d}r \tag{6.3}$$

where D is the positive region of the first intense peak of the integrand. Because $G_d(r,t)$ decays to unity at large t, $G_d(r,t) = 1$ provides the baseline to define the density fluctuation. $N(t)$ is proportional to the dynamic coordination number, and reflects the average decorrelation fime for atoms located near the first peak of $G_d(r,t)$. The decorrelation time is the time for an atom initially located near the central atom to begin to diffuse away. This time is a function of the distance that an atom is from the central atom's initial position. It also depends on the local structure, which can be quite varied [29]. Since the exponential

decay time for each atom is different, the overall decay of $N(t)$ could be described by a Kohlrausch-Williams-Watts (KWW) stretched exponential function [30],

$$y(t) = \exp\left(-(t/\tau)^{\beta}\right) \tag{6.4}$$

where τ is the time constant and β is the stretching factor. From MD simulations and a recent study on water [12] $N(t)$ is expected to have two decay rates; one is due to ballistic motion and another one describes the changes in the configuration of the nearest-neighbors, the opening of the cage. However, due to the limited energy range of these experiments for $Zr_{80}Pt_{20}$ it was not possible to determine the decay rate in the ballistic region. The normalized peak intensity $N(t)/N(0)$ is shown in Fig. D.4. The initial decay in $N(t)/N(0)$, $t < 0.1$ps, is due to ballistic motion and is only weakly dependent on temperature. As $t \to \infty$ it is expected that $N(t)/N(0) \to 0$ as the correlations between the initial position are lost. The data show plateaus at longer times; these are artifacts from the resolution function correction (see supplemental material in Appendix D) and are not fit to the KWW expression. The ballistic region is not well described by the single KWW expression. The dashed lines in Fig. D.4 are fits to the KWW expression, which describes well the data beyond 0.1ps for all temperatures studied.

As mentioned earlier, the local configuration time, τ_{LC} cannot be obtained directly from the experimental data. However, our MD simulations show that τ_{LC} is related to a measurable quantity called here the Van Hove time, τ_{VH}, which is the long decay time corresponding to the configuration of nearest-neighbors in the first peak in $G_d(r,t)$. The experimental value of the Van Hove time was obtained from the mean relaxation time of the KWW function fit to the data, $\langle\tau_r\rangle = \frac{\tau}{\beta}\Gamma(\frac{1}{\beta}) \equiv \tau_{VH}$. The results from the MD simulations shown in Fig. 6.3 indicate that $\tau_{LC} \approx \tau_{VH}/3.6$ for $T > T_A$. Since the ratio is approximately constant for $T/T_A > 1.2$ the activation energy for τ_{VH} will be the same as for τ_{LC}. For water τ_{LC} was approximately equal to τ_{VH} (τ_2 in their work) [12]. Since metallic liquids have more nearest

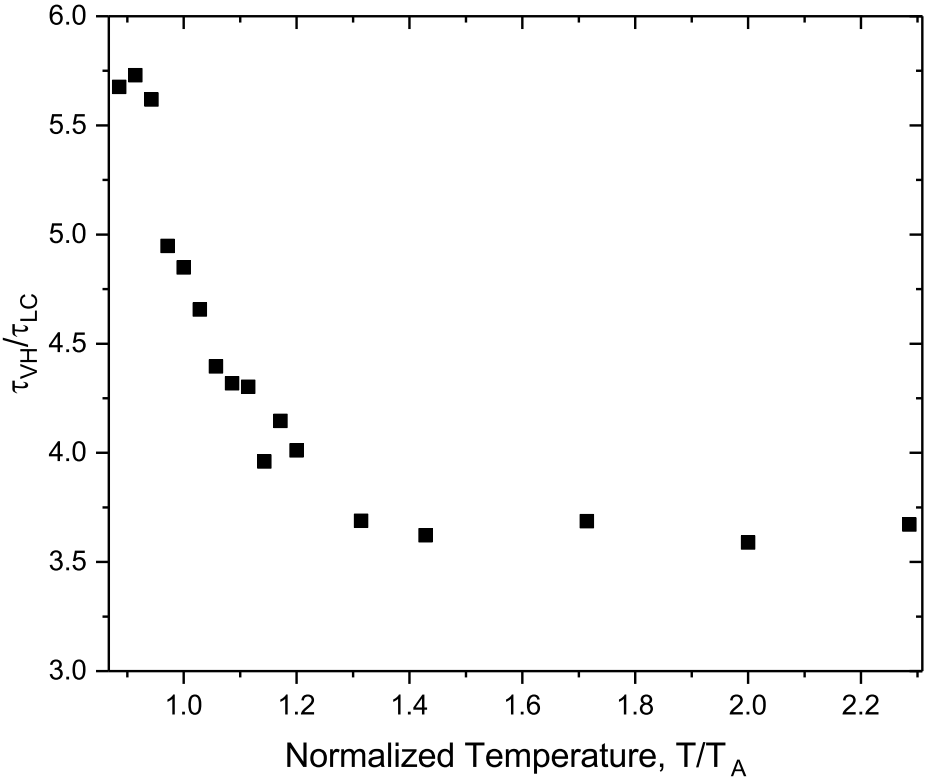

Figure 6.3: The ratio of the Van Hove time, τ_{VH}, to the local configuration time, τ_{LC}, as a function of temperature normalized to $T_A \approx 1750$K from MD simulations of liquid $Zr_{80}Pt_{20}$. $\tau_{VH}/\tau_{LC} \approx 3.6$ for $T > T_A$.

neighbors than does water ($\sim$ 13 for metallic liquids and 4 for water), the ratio τ_{VH}/τ_{LC} should reflect this difference.

As shown in Fig. 6.4a, τ_{VH} obtained from the scattering data shows an Arrhenius temperature dependence for $T_A/T > 1$, as indicated by the previous MD simulations for the related local configuration time, τ_{LC} [7]. The results from the MD studies indicate that τ_{LC} remains Arrhenius far below T_A. Based on the results in Fig. 6.3, τ_{VH} should become super-Arrhenius below this temperature, as suggested by the data in Fig 6.4b. The activation energy for τ_{VH} (and from Fig. 6.3, for τ_{LC}) above T_A is 750$\pm$90meV. As shown in Fig. 6.4b, the activation energy for the measured viscosity above T_A is 730$\pm$30meV. Within experimental error, then, these activation energies are equal, indicating that the energy barrier is the same for each process. Furthermore, approximating τ_M from the viscosity (not shown) and comparing to τ_{LC} we find that $\tau_M \approx \tau_{LC}$. This provides experimental evidence that the MD predictions [6, 7] are correct, i.e. showing that the atomic rearrangements that determine τ_{VH} (and τ_{LC}) are controlling the viscosity at high temperatures.

6.4 Conclusion

In summary, the time dependent pair distribution function (distinct Van Hove function, $G_d(r,t)$) was obtained as a function of temperature from inelastic neutron scattering data for equilibrium and supercooled $Zr_{80}Pt_{20}$ liquids made in a containerless environment. Molecular dynamics simulations showed that the relaxation time of the of the positive peak area in $G_d(r,t)$ (defined as the Van Hove time, τ_{VH}) is related to the local configuration time, τ_{LC} , and has the same temperature dependence above the crossover temperature, T_A. A comparison of the experimental neutron scattering and viscosity data show that the activation energy of τ_{VH} and that of the Maxwell time, τ_M are equal to within experimental error, strongly suggesting that they are governed by the same process . To our knowledge this is the first experimental evidence for a key prediction from recent MD studies for metallic liquids,

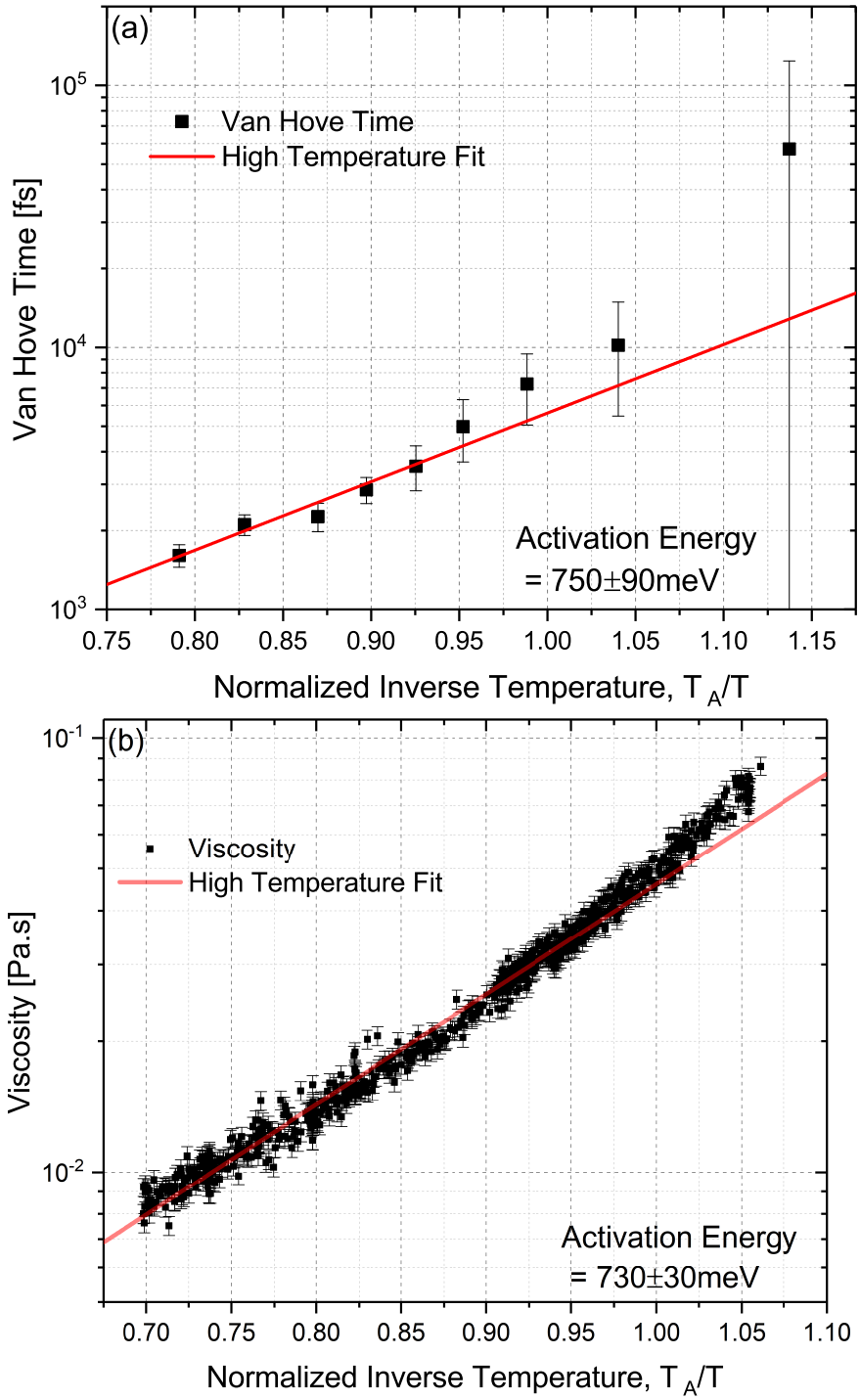

Figure 6.4: (Color online) (a) Van Hove time and (b) viscosity data for liquid $Zr_{80}Pt_{20}$ versus inverse temperature normalized to the Arrhenius crossover temperature determined from the viscosity (T_A = 1450K). The best fit lines for the activation energy are shown; the slopes give an activation energy of 730meV for the viscosity and 750meV for τ_{VH}. The error bars shown for τ_{VH} are 3σ and are calculated from the error in the fit parameters from Eq. 6.4.

which indicate that local structural excitations underlie the viscosity at high temperature.

6.5 References

[1] R. Ashcraft et al. Experimental measurements of the temperature-dependent Van Hove function in a $Zr_{80}Pt_{20}$ liquid - Confirmation of a structural origin for the dynamics at high temperature (2018). arXiv: 1810.02351.

[2] C. A. Angell. Formation of Glasses from Liquids and Biopolymers. *Science* **267**,5206 (1995). DOI: 10.1126/science.267.5206.1924.

[3] D. Kivelson et al. Fitting of viscosity: Distinguishing the temperature dependences predicted by various models of supercooled liquids. *Physical Review E* **53**,1 (1996). DOI: 10.1103/PhysRevE.53.751.

[4] W. Gotze and L. Sjögren. Relaxation processes in supercooled liquids. *Reports on Progress in Physics* **55**,3 (1992).

[5] R. Soklaski et al. A locally preferred structure characterises all dynamical regimes of a supercooled liquid. *Philosophical Magazine* **96**,12 (2016). DOI: 10.1080/14786435.2016.1158427. arXiv: 1502.01739.

[6] T. Iwashita, D. M. Nicholson, and T. Egami. Elementary Excitations and Crossover Phenomenon in Liquids. *Physical Review Letters* **110**,20 (2013). DOI: 10.1103/PhysRevLett.110.205504.

[7] T. Iwashita and T. Egami. Local energy landscape in a simple liquid. *Physical Review E* **90**,5 (2014). DOI: 10.1103/PhysRevE.90.052307.

[8] N. A. Mauro et al. Electrostatic levitation facility optimized for neutron diffraction studies of high temperature liquids at a spallation neutron source. *Review of Scientific Instruments* **87**,1 (2016). DOI: 10.1063/1.4939194.

[9] L. Van Hove. Correlations in space and time and born approximation scattering in systems of interacting particles. *Physical Review* **95**,1 (1954). DOI: 10.1103/PhysRev.95.249.

[10] U. Dahlborg, W. Gudowski, and M. Davidovic. Van Hove correlation functions from coherent neutron inelastic scattering. *Journal of Physics: Condensed Matter* **1**,35 (1989). DOI: 10.1088/0953-8984/1/35/016.

[11] T. Iwashita et al. Seeing real-space dynamics of liquid water through inelastic x-ray scattering. *Science Advances* **3**,12 (2017). DOI: 10.1126/sciadv.1603079.

[12] Y. Shinohara et al. Viscosity and real-space molecular motion of water: Observation with inelastic x-ray scattering. *Physical Review E* **98**,2 (2018). DOI: 10.1103/PhysRevE.98.022604.

[13] W. K. Rhim et al. Development of an electrostatic positioner for space material processing. *Review of Scientific Instruments* **56**,2 (1985). DOI: 10.1063/1.1138349.

[14] N. A. Mauro et al. Short- and medium-range order in $Zr_{80}Pt_{20}$ liquids. *Physical Review B* **83**,18 (2011). DOI: 10.1103/PhysRevB.83.184109.

[15] W.-K. Rhim et al. Noncontact technique for measuring surface tension and viscosity of molten materials using high temperature electrostatic levitation. *Review of Scientific Instruments* **70**,6 (1999). DOI: 10.1063/1.1149797.

[16] A. K. Gangopadhyay et al. Correlation of the fragility of metallic liquids with the high temperature structure, volume, and cohesive energy. *Journal of Chemical Physics* **146**,15 (2017). DOI: 10.1063/1.4981011.

[17] D. L. Abernathy et al. Design and operation of the wide angular-range chopper spectrometer ARCS at the Spallation Neutron Source. *Review of Scientific Instruments* **83**,1 (2012). DOI: 10.1063/1.3680104.

[18] S. Plimpton. Fast Parallel Algorithms for Short-Range Molecular Dynamics. *Journal of Computational Physics* **117**,1 (1995). DOI: 10.1006/jcph.1995.1039. arXiv: nag.2347 [10.1002].

[19] Y. Q. Cheng and E. Ma. Atomic-level structure and structure-property relationship in metallic glasses. *Progress in Materials Science* **56**,December 2010 (2011). DOI: 10.1016/j.pmatsci.2010.12.002.

[20] A. Hirata et al. Geometric frustration of icosahedron in metallic glasses. *Science (New York, N.Y.)* **341**,July (2013). DOI: 10.1126/science.1232450.

[21] S. Nosé. A unified formulation of the constant temperature molecular dynamics methods. *The Journal of Chemical Physics* **81**,1 (1984). DOI: 10.1063/1.447334.

[22] W. G. Hoover. Canonical dynamics: Equilibrium phase-space distributions. *Physical Review A* **31**,3 (1985). DOI: 10.1103/PhysRevA.31.1695.

[23] Relaxation processes in liquids: Variations on a theme by Stokes and Einstein. *Journal of Chemical Physics* **138**,12 (2013). DOI: 10.1063/1.4775741.

[24] O. Arnold et al. Mantid - Data analysis and visualization package for neutron scattering and μ SR experiments. *Nuclear Instruments and Methods in Physics Research, Section A: Accelerators, Spectrometers, Detectors and Associated Equipment* **764**, (2014). DOI: 10.1016/j.nima.2014.07.029. arXiv: 1407.5860.

[25] D. L. Abernathy, J. L. Niedziela, and M. B. Stone. Extracting source parameters from beam monitors on a chopper spectrometer. *EPJ Web of Conferences* **83**, (2015). DOI: 10.1051/epjconf/20158303001.

[26] T. Scopigno, G. Ruocco, and F. Sette. Microscopic dynamics in liquid metals: The experimental point of view. *Reviews of Modern Physics* **77**,3 (2005). DOI: 10.1103/RevModPhys.77.881. arXiv: 0503677 [cond-mat].

[27] J. R. Copley and S. W. Lovesey. The dynamic properties of monatomic liquids. *Reports on Progress in Physics* **38**,4 (1975). DOI: 10.1088/0034-4885/38/4/001.

[28] J.-P. Hansen and I. R. McDonald. *Theory of Simple Liquids: with Applications to Soft Matter*. Fourth. Amsterdam: Elsevier/AP, 2013.

[29] M. L. Johnson et al. Measurements of structural and chemical order in Zr80Pt20 and Zr77Rh23 liquids. *Physical Review B* **93**,5 (2016). DOI: 10.1103/PhysRevB.93.054203.

[30] A. Cavagna. Supercooled liquids for pedestrians. *Physics Reports* **476**, (2009). DOI: 10.1016/j.physrep.2009.03.003. arXiv: 0903.4264.

Chapter 7: Summary and Conclusion

This dissertation has examined, through both experimental and Molecular Dynamics simulation techniques, the relationship between the dynamics and structure in the equilibrium and supercooled liquid. These studies were aimed at developing a better understanding of the liquid state in an attempt to eventually understand why some liquids more easily form glasses than others. To this end, high quality X-ray and neutron diffraction and thermophysical property measurements were made in the equilibrium and supercooled liquid using the containerless processing technique. The major results from these studies are summarized below.

In Chapter 3 Molecular Dynamics (MD) simulations were performed on three model systems (Zr, $Cu_{50}Zr_{50}$, and $Cu_{50}Zr_{45}Al_5$) to obtain the atomic configuration and $g(r)$. Corresponding Reverse Monte Carlo simulations were conducted using the $g(r)$ found as the only input constraint, termed in this thesis as minimally constrained reverse Monte Carlo (mcRMC) simulations. The mcRMC atomic configurations were then compared to the original MD configurations using the Voronoi tessellation technique to characterize the local atomic environment. The results of an analysis in terms of the Voronoi index, nearest-neighbor distance, asphericity, volume and coordination number were compared using the L^1 histogram distance. In general, it was found that the distributions of the Voronoi index, asphericity, volume and coordination number are not well reproduced, especially if the system contains more than one atomic species. However, the average properties of the system were typically reproduced, although in most cases the temperature dependence of the parameters, when compared to the original MD values, were not consistent. This study was meant to mimic the use of mcRMC simulations from X-ray or neutron diffraction experiments with a realistic number of constraints, and thus examines the reliability of the mcRMC for experimental data.

In Chapter 4 Reverse Monte Carlo (RMC) simulations of X-ray diffraction data obtained using the Electrostatic Levitation (ESL) technique and Molecular Dynamics (MD) simulation data were presented to examine the recent reports of anomalous thermal contraction, based on a more robust measure of the nearest-neighbor distances. Previous studies have attempted to examine the average atomic position using the peak position in $g(r)$. This amounts to using the mode of the nearest-neighbor distribution, which fails to account for the inherent skewness, due to the anharmonicity of the interatomic pair potential, and increasing skewness with increasing temperature of the nearest-neighbor distance distribution. Using the results of the reliability of mcRMC from Chapter 3 to obtain the nearest-neighbor distances, distributions were computed from a Voronoi tessellation of the mcRMC and MD configurations. The central tendency, mean and median, of these distributions were then tracked as a function of temperature to extract the thermal expansion coefficient. It was found that the thermal expansion coefficient obtained using only the nearest-neighbor distance correlates with the bulk volumetric measurements and the rates of expansion were similar. This provides strong evidence that all higher order coordination shells likely expand at the same rate. These two results taken together call into question the interpretation of results by other who claim that fragility is related to only longer range (third and fourth coordination shell) correlations. Our work exhibits the local nature of fragility.

In Chapter 5 the results from X-ray diffraction and viscosity measurements using the Electrostatic Levitation (ESL) technique were combined to examine the structure dynamics connection in the equilibrium and supercooled liquid. The viscosity measurements were examined using a bootstrapping routine, where the viscosity data is resampled within error to obtain multiple measurements of the Arrhenius crossover temperature T_A so that the error could be estimated. The X-ray diffraction data is reduced to obtain the static structure factor, $S(q)$, which is the momentum space equivalent of the pair distribution function, $g(r)$. The second peak of $S(q)$ exhibits marked changes with temperature, developing a shoulder on the high-q side. This peak was fit with two Gaussian functions, and the height of the low-

q peak was tracked with temperature. This sub-peak, which is commonly associated with the next-nearest neighbor distance, exhibited an accelerated growth at a temperature T_S which is correlated with, but always lower, than T_A. Though the reason for $T_S < T_A$ is still an open question, the connection between the two is clear evidence of a structure-dynamics connection.

In Chapter 6 inelastic neutron scattering (INS) measurements using the Electrostatic Levitation (ESL) technique and Molecular Dynamics (MD) simulations of $Zr_{80}Pt_{20}$ were presented. These results confirm that local configurational excitations (corresponding to the time, τ_{LC}, that it takes to change the coordination number of a local cluster by one) control the liquid viscosity, as predicted in recent MD studies. In the INS measurements the dynamic structure factor, $S(q,\omega)$ was obtained and a new analysis method was developed to reduce the diffraction data. After basic instrument corrections $S(q,\omega)$ was Fourier transformed to obtain the intermediate scattering function, $F(q,t)$, where a physical normalization, i.e. forcing $F(q,0) \equiv S(q) \to 1$ as $q \to \infty$, is applied. To obtain only the coherent (distinct) scattering data, which contains the pair correlations, an approximation to the incoherent (self) data was fitted to the full signal and subtracted out. This result was Fourier transformed to obtain the distinct dynamic pair correlation function, $G_d(r,t)$, also known as the distinct Van Hove correlation function. The area under the first peak in $G_d(r,t)$, which can be related to τ_{LC}, was tracked, yielding the Van Hove time, τ_{VH}, and the activation energy of this was determined. The Van Hove time, multiplied by a scale factor determined from MD simulations, was equal in both temperature dependence and magnitude, to the Maxwell relaxation time (obtained from the viscosity). This confirms that the high temperature liquid is controlled by local structural excitations. Furthermore, since the Maxwell time becomes super Arrhenius as the liquid is cooled while the configurational excitations remain Arrhenius a crossover occurs in the viscosity, where cooperativity or longer range interactions begin.

A clear and extensive connection between established that spans from the equilibrium to the supercooled liquid. While the results presented here do not expressly connect to

the glass transition they do aid in understanding the liquid and the changes that begin to occur in both structure and dynamics at the crossover temperature T_A, and which appear to culminate in the glass transition. They make it clear that a deeper understanding of the structure-dynamics relationship at high temperature is key to understanding the glass transition and the ability to predict glass formation.

Appendix A: Inelastic Neutron Analysis Guide

This appendix gives an overview of the steps needed to produce the distinct Van Hove correlation function, $G_d(r,t)$, from inelastic neutron scattering (INS) data taken at the Wide Angular-Range Chopper Spectrometer (ARCS) beamline located at Oak Ridge National Laboratory (ORNL). This method has been discussed briefly in Chapter 6, but it is informative to give a more complete description along with the code used. A complete diagram of the analysis is shown in Fig. D.2.

A.1 Analysis and Methods

The first step, after acquiring the data, is to use a standardized time-of-flight direct-geometry spectrometer (DGS) data reduction routine in MANTID [1]. A manual for the DGS reduction can be found on the ORNL website (`https://neutrons.ornl.gov/sites/default/files/mantid-dgs-data-reduction-for-users-5-03.pdf`) and is performed on the Oak Ridge National Laboratory (ORNL) analysis server (`https://analysis.sns.gov/`). An XML file is created and run within an ipython environment (in the command line run `"ipython"`) using the command `"run -i dgsreductionmantid *.xml"` where * is replaced with the name of the user created XML file. An example XML file is shown in Fig. A.2 for the data collected during scan 95531 from ARCS2017.

Most options shown in this file will not change between runs or even experiments and are mentioned in more detail in the dgsreduction guide. Some of the more important parameters are briefly mentioned here. "runs" determines the dataset that will be reduced from the XML files."save" sets save options, where iofqearray is the most important because it is used in the following analysis. The incident neutron energy is set with the "efixed" command while the time delay for the peak of the neutron pulse from the moderator is set with "t0". These

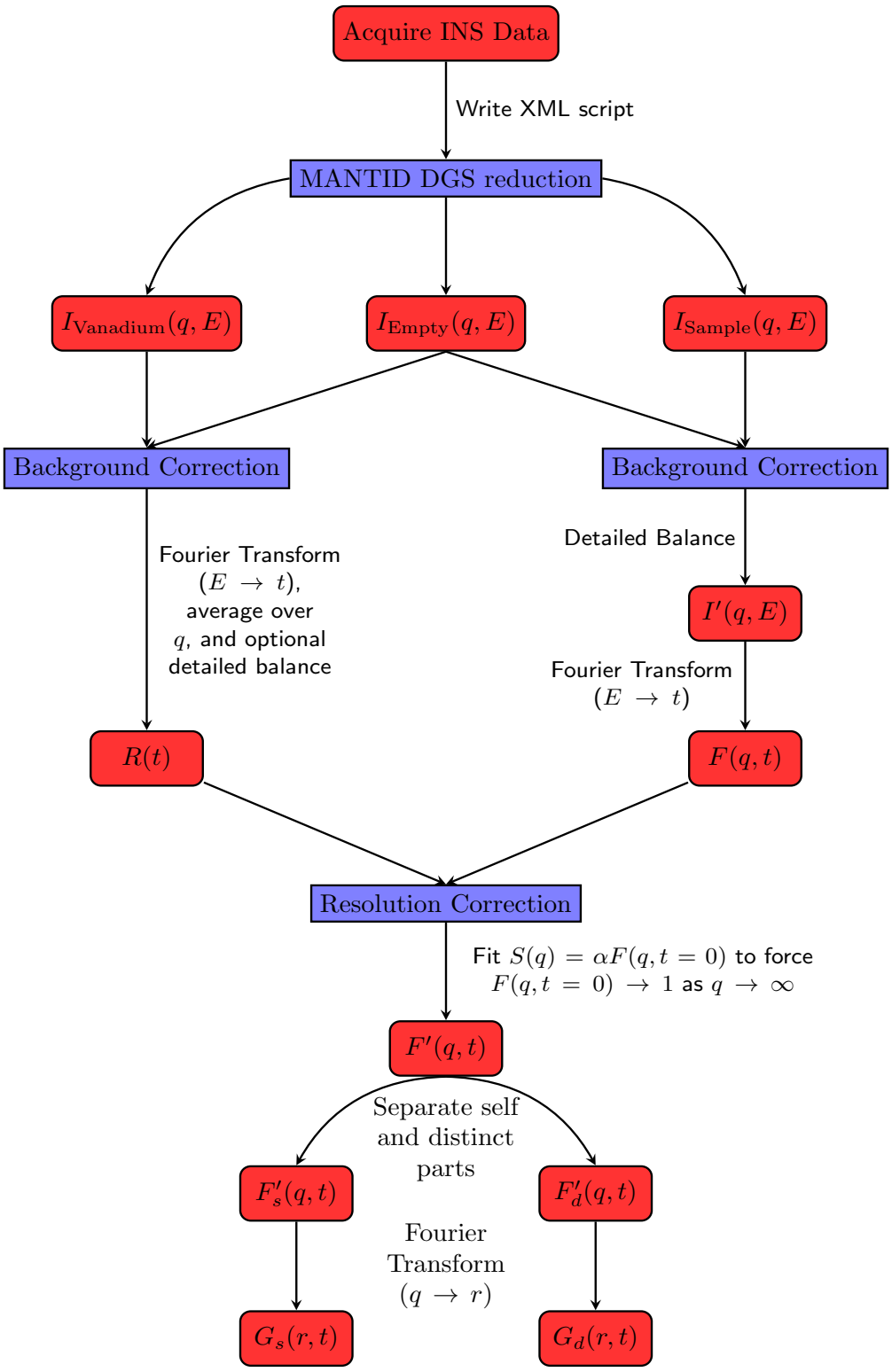

Figure A.1: A detailed flow chart for the evaluation of inelastic neutron scattering data acquired at the ARCS beamline. Blue boxes indicate calculations that combine data or set spacing where care needs to be taken to ensure common spacing.

```
<?xml version="1.0" ?>
<dgsreduction>
  <!-- DEFAULTS section -->
    <defaults
      instrument="ARCS"
      filterbadpulses = "False"
      save='summary'
    />

  <!-- CALIBRATION AND MASKING section -->
    <calibration processedfilename = "Vanadium_95545_white_20170511.nxs" units="wavelength" normalizedcalibration
    = "False">
      <vanruns>95545</vanruns>
      <vanmin>0.35</vanmin>
      <vanmax>0.75</vanmax>
      <mask algorithm="BankTubePixel" pixel="1-7"/>
      <mask algorithm="BankTubePixel" pixel="122-128"/>
      <mask algorithm="BankTubePixel" bank="71" pixel="1-14"/>
      <mask algorithm="BankTubePixel" bank="71" pixel="114-128"/>
      <mask algorithm="BankTubePixel" bank="70" pixel="1-12"/>
      <mask algorithm="BankTubePixel" bank="70" pixel="117-128"/>
      <mask algorithm="angle" twothetamax="2.5"/>
      <mask algorithm="BankTubePixel" bank="3" tube="3"/>
      <mask algorithm="BankTubePixel" bank="80" />
      <mask algorithm="FindDetectorsOutsideLimits" LowThreshold="0.1"/>
      <mask algorithm="MedianDectectorTest" LowThreshold="0.5" HighThreshold="1.5" ExcludeZeroesFromMedian=
      "1" LevelsUp="1" CorrectForSolidAngle="1"/>
    </calibration>
  <!-- SCAN section -->
    <scan runs="95531" save='nxspe,nxs,iofqearray,summary' efixed='19.9883' emin='-60.1' emax='60.1' ebin='0.2' t0=
    '41.0925' calce='false' grouping='2X1' friendlyname='20171002_Zr80Pt20_20meV_minus_150C' qmin='0.515' qmax='8'
    qstep='0.05'/>
</dgsreduction>
```

Figure A.2: An example XML file reducing the data for run 95531. Many of the lines in this file are default values and will not need to be changed.

two parameters are linked and must be changed together. They are not directly available from scattering with the NESL but can be obtained from the beamline scientist. If they are poorly set a noticeable shift in the location of the elastic line from $E_i = 0$ will occur. "calce" tells the reduction routine to calculate the incident energy which must be set to false. The "vanruns" parameter under the calibration section is the white beam vanadium calibration scan run number. The energy range should typically go to $\pm E_i$ though more data is available in on the neutron energy gain side ($E < 0$). The maximum q value is set by the kinematic restrictions of INS scattering as discussed in Chapter 2. The q-spacing should be ∼0.5-1.0% of the maximum q on the elastic line. The E-spacing should be ∼1.0% of the incident energy. The remaining parameters are either self-explanatory, default values, or available in the dgsreduction guide.

The dgs analysis must be run for the sample, vanadium and empty scans changing the run numbers as needed in the XML file (the rest of the parameters should be the same). The vanadium reduction is only needed if the resolution function of the spectrometer is going to be approximated from the vanadium scattering profile. The empty scattering is necessary

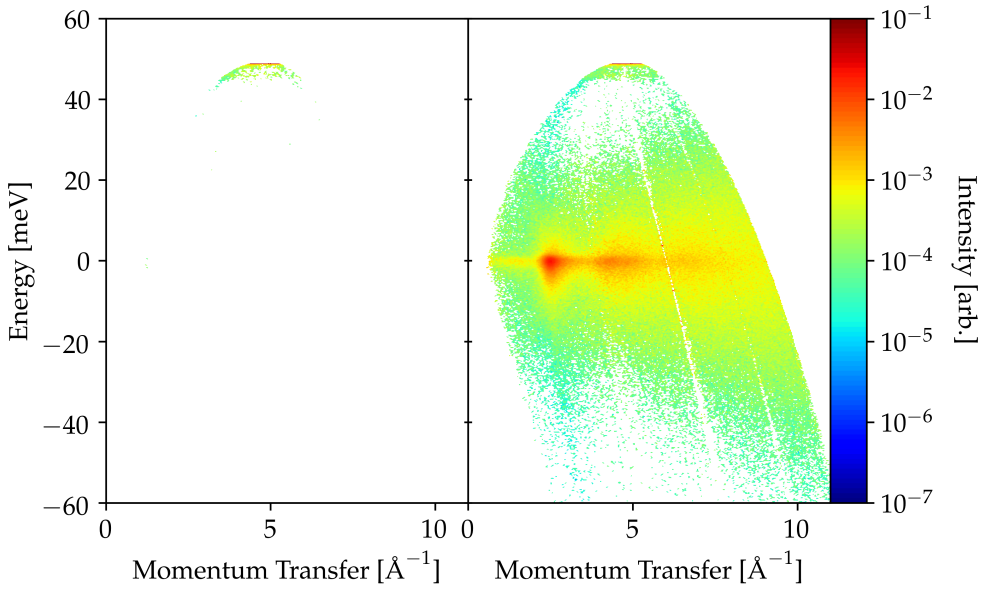

Figure A.3: Output DGS reduction for a typical liquid sample (right) and empty chamber (left). The empty chamber only produces a scattering signal near the maximum energy transfer ($E_i = 50$meV).

to eliminate scattering from the sample environment (the NESL in this case). However, scattering from the NESL and other background is extremely small compared to the sample except at the limit of neutron energy loss ($E \approx E_i$). If this region is removed the background correction can be effectively omitted. The background compared to the sample signal can be seen in Fig A.3. The need for a background correction increases at lower incident energy as the signal at the maximum energy transfer begins to impinge on the inelastic scattering from the sample.

The scattering intensity output from the DGS reduction is given by

$$I(q, E) = \frac{\Phi}{\epsilon} \frac{k_1}{k_2} I^0(q, E) * R(q, E) \ , \tag{A.1}$$

where $I^0(q, E)$ is the ideal scattering intensity, $R(q, t)$ is the resolution function of the spectrometer, ϵ is the detector efficiency, Φ is the flux of incident neutrons (using proton charge), $\frac{k_1}{k_2}$ is the ratio of the incoming to outgoing wave number and $*$ signifies the convolution operation. This is proportional to the dynamic scattering factor ($S(q, E)$), again convoluted with

the resolution function. To perform the remaining corrections, the output file containing the scattering intensity is transferred from the ORNL analysis server to a local computer. The data can be transferred using the Cyberduck SFTP program (instructions are included on the analysis server login page). The remaining corrections and analysis are performed via python using a Jupyter notebook (*INS_Analysis.ipynb*) for interactive plotting and changing of input parameters. The line numbers referenced within this section refer to the code for the analysis located in the next section.

The first correction applied to both the vanadium and sample scattering data is the background correction (i.e. $I_S(q,E) - I_E(q,E)$) (lines 88-105,472). As mentioned previously this correction can be omitted if the chosen incident neutron energy is high enough. This would mean that E_i would need to be larger than the extent of the required inelastic signal by approximately 5 meV. Other than the intense scattering signal near E_i the background scattering for the NESL is extremely low (again see Fig. A.3).

The next correction applied to the scattering intensity is detailed balance (lines 107-156,473), which is a result of the equal probability of a neutron losing or gaining energy as a result of the scattering interaction. The correction is given by:

$$S(q,E) = S(q,-E)e^{-\frac{E}{k_b T}} \ , \tag{A.2}$$

where $S(q,E)$ is replaced with proportional scattering intensity from the DGS reduction routine. This factor is used to extend the range of data in the positive energy transfer region and is only applied to locations where data is missing. Several options are available when using detailed balance: symmetrizing the data with respect to the positive or negative energy transfer and filling in missing data (as it done here). Figure A.4 shows the DGS reduced $I(q,E)$ data and the data with both the detailed balance factor applied and corrected for background scattering.

The intensity data with the background and detailed balance corrections is then Fourier

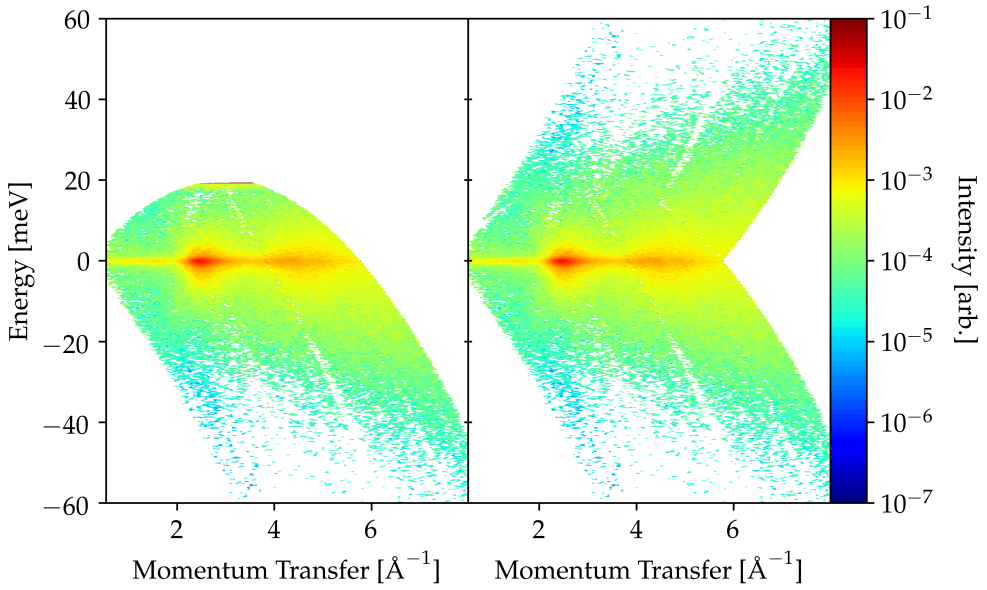

Figure A.4: Example INS data before (left) and after (right) the detailed balance correction. The empty chamber correction was used to remove the scattering signal near $E_i = 20$meV.

transformed (lines 179-227,474) to obtain the intermediate scattering function

$$F(q,t) = \int S(q,\omega)e^{-i\omega t}\mathrm{d}\omega \ , \tag{A.3}$$

where $E = \hbar\omega$. The energy range available for the Fourier transform is dependent on the chosen incident energy but the region may be extended using the detailed balance factor and by using more of the negative energy transfer region (this region is not limited like the positive energy transfer). The Fourier transformed data is shown in Fig. A.5. Due to the shape of the input data nothing past the maximum q value on the elastic line is usable and the data becomes less trustworthy as $q \to 0$.

Up until this point the data has consisted of a convolution of the resolution function and the true scattering intensity. After the Fourier transform this is instead a product of the resolution function (as a function of time) and the scattering intensity. If the resolution function is determined (lines 283-305) then it can be divided out to obtain the true scattering signal. The left branch of Fig. D.2 shows the reduction of the vanadium scattering data to

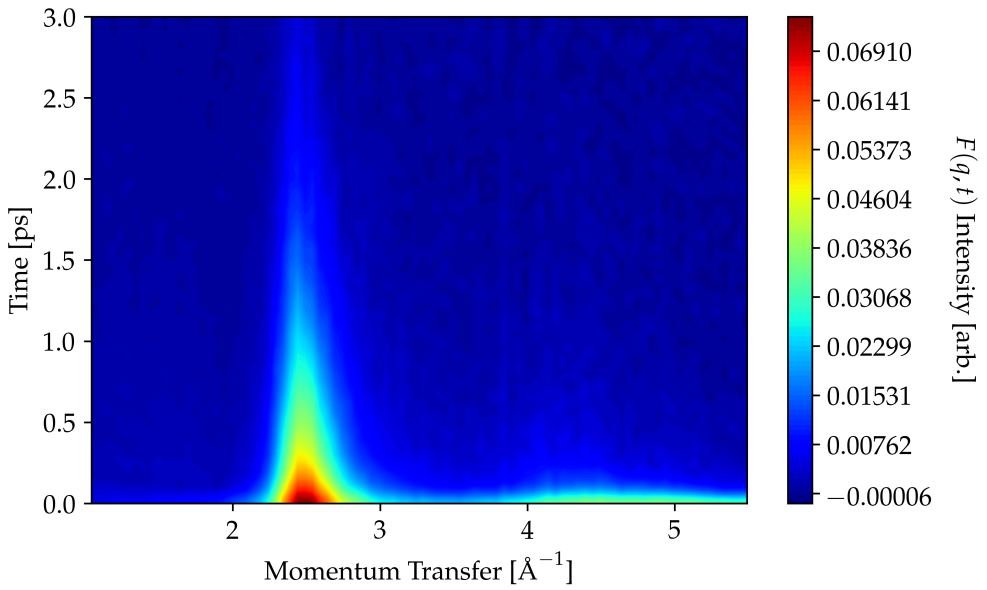

Figure A.5: Representative plot of the intermediate scattering function ($F(q,t)$) obtained by Fourier transforming the dynamic structure factor ($S(q,E)$).

obtain the resolution function, which is similar to the data reduction except the vanadium data is averaged over q and detailed balance is not applied. It is assumed that the vanadium scatters completely incoherently giving just the incident beam profile and that the resolution function (and vanadium) are independent of q. This last assumption is the more tenuous of the two but still holds if the vanadium data is truncated to a small enough region in q, E-space. The resolution function and the resolution function corrected intermediate scattering function (lines 476-479) are shown in Fig. A.6. The resolution function for ARCS is still not well understood and this approximate form causes the intermediate scattering function data to exhibit long time correlations, which is not expected in the liquid state. A better understanding of the resolution function is necessary to obtain more high quality data.

The final correction to be applied to the scattering data is the normalization factor (lines 307-361, 480), which puts the intensity into real units. This factor can be found from the vanadium scattering data but here the behavior of $S(q)$ as $q \to \infty$ is used instead. A multiplicative factor is needed to place the long-q limit of $S(q)$ to one. A complication arises from the truncated q-space typical of these INS experiments. To reduce the arbitrary

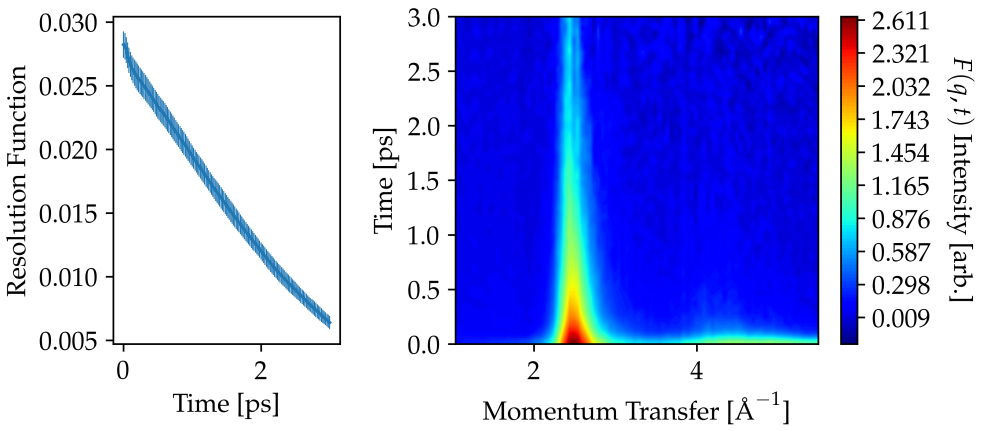

Figure A.6: (Left) Resolution function obtained from the vanadium scattering data as a function of time. (Right) Representative intermediate scattering function corrected for the resolution function. The resolution function causes the long time limit data to drastically increasing.

choice of the scale factor, previously measured X-ray and neutron (preferred) static structure factors, $S(q)$, at similar temperatures are used to fit the scale factor ($S(q) = \alpha F(q, t = 0)$). A representative result of this procedure is shown in Fig. A.7.

To separate the self and distinct parts (lines 363-420,481) of the intermediate scattering function a modified version of the method developed by Dahlborg *et al.* [2] is used. The fitting function which describes the self part is given by:

$$F_s(q,t) = A_t e^{-w_t q^2} \tag{A.4}$$

where A_t the amplitude and w_t the width are time dependent fitting parameters. A complication again arises from the small q-range available in these experiments. The fitting function does not have a very large region of the tailing behavior to fit to which will cause the fitting function to over fit the main peak in $F(q,t)$ and the low q region. To account for this a fictitious error is added to the fitting routine which weights the higher q region more strongly (an arbitrary choice of an exponential weighting in q was used). The relevant errors and fitting is shown in Fig. A.8.

Finally, the Fourier transform from $q \rightarrow r$ is performed (lines 229-281, 482) to obtain the

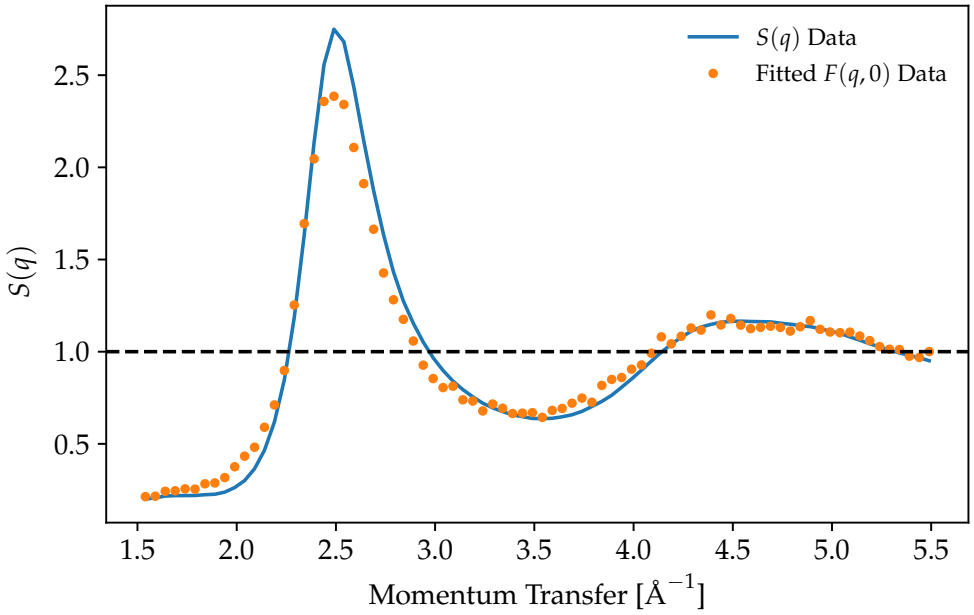

Figure A.7: Example of fitting $F(q, t = 0)$ INS data to $S(q)$ from previously measured X-ray diffraction. This fitting method is used to force $F(q, t = 0)$ to approach one at high-q giving a multiplicative normalization factor. The scale factor from this analysis is $\alpha = 0.888$.

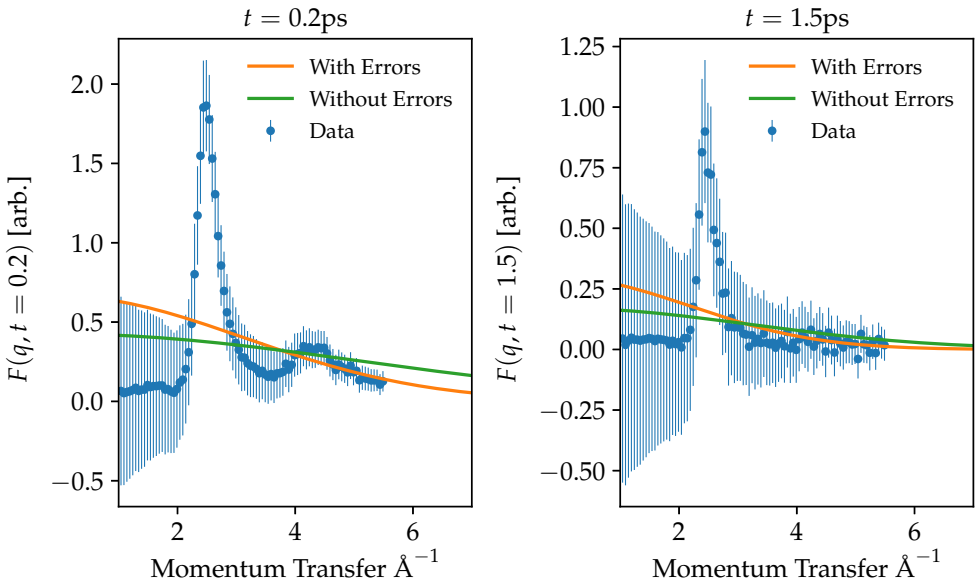

Figure A.8: Plot of $F(q, t)$ at two times t =0.2 ps and t =1.5 ps with modified error bars. The data is fit to a Gaussian function using the modified error bars (orange) emphasize the long q tail and without error bars (green).

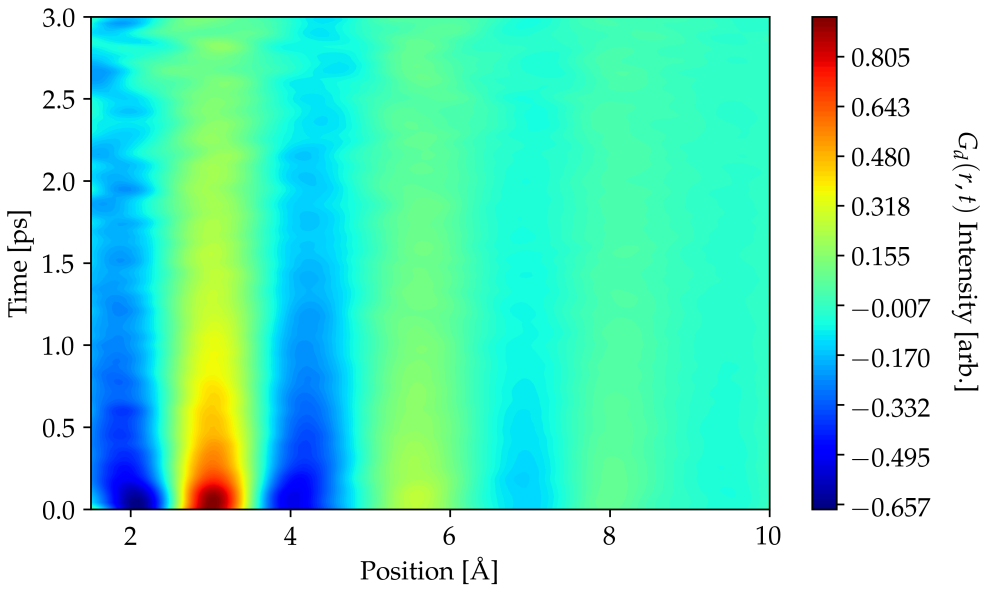

Figure A.9: A representative distinct Van Hove correlation function.

distinct Van Hove correlation function. This Fourier transform is given by

$$G_d(r,t) - 1 = \frac{1}{2\pi\rho} \int F_d(q,t) \frac{q}{r} \sin(qr) \mathrm{d}q \ , \tag{A.5}$$

where ρ is the sample density. An example distinct Van Hove correlation function is shown in Fig. A.9.

A.2 Python Code

The previous section documented the corrections and analysis performed to obtain the distinct Van Hove correlation function from INS data. This section gives the code developed which performs the corrections after the DGS reduction. The included code is written as a standard python script but it is better to run it in an interactive environment (such as a Jupyter notebook). There is currently no output/saving feature included by default but could easily be added by using the pandas package DataFrame saving methods.

```
1 '''This code uses the output file (iofqecolumn) of the MANTID dgs reduction routine to obtain the self and
      distinct parts of the Van Hove correlation function. The remaining corrections (namely a background
      correction, detailed balance, resolution function correction, and a normalization scale factor) are
```

```
    performed. The intermediate scattering function is then split into the self and distinct parts and
    Fourier transform to obtain the Van Hove correlation function. Consistent with Python 2.7.15.
Written by: Robert Ashcraft'''

from glob import glob
import numpy as np        #1.14.3
import pandas as pd       #0.23.0
from functools import partial
from scipy import integrate   #1.1.0
from numba import njit      #0.38.0
from lmfit import Parameters, fit_report, minimize    #0.9.10
from scipy.interpolate import splrep,splev    #1.1.0

#Plotting Options
import matplotlib.pyplot as plt
from matplotlib import ticker, cm
import matplotlib.colors as mcolors
from matplotlib import rc
rc('font',**{'family':'sans-serif','sans-serif':['Helvetica']})
rc('text', usetex=False)
rc('axes', labelsize=20)
rc('ytick',labelsize=16)
rc('xtick',labelsize=16)
plt.rc('axes', titlesize=20)
plt.rcParams["figure.figsize"] = [10,12]

def makevariable(start,end,spacing):
  '''Creates an evenly spaced array starting at start and ending closest to end given the spacing
    IN:
        start:    starting location (float)
        end:      maximum ending location (float)
        spacing:    variable spacing (float)
    OUT:
        var:      variable array (numpy array of float)'''

  var = np.arange(start,end+spacing,spacing)
  var = np.around(var,decimals=2)
  var = var[var<=end]
  return(var)

def readdata(f):
  '''Reads the data file f for (iofqecolumn format from dgs reduction)for the momentum
  transfer (q), energy transfer (E), data (I(q,E)), and error (err(q,E)) in the format below.
    IN:
        f:      file path (string)
        FILE FORMAT:
        Number-of-E Number-of-Q

        q1
        q2
        ...
        qN

        E1
        E2
        ...
        EN

        I(q1,E1)  I(q2,E1)  ... I(qN,E1)
        I(q1,E2)    .   .   .
        ...         .   .   .
        I(q1,EN)    .   .   .

        err(q1,E1)  err(q2,E1)  ... err(qN,E1)
        err(q1,E2)    .     .   .
        ...           .     .   .
        err(q1,EN)    .     .   .
    OUT:
        q:    momentum transfer array (numpy array of float)
        E:    energy transfer array (numpy array of float)
        data:   intensity DataFrame (pandas DataFrame of float)
        error:    intensity error DataFrame (pandas DataFrame of float)'''

  sizes = pd.read_csv(f,delim_whitespace=True,nrows=1,names=['Esize','qsize'])
  q = pd.read_csv(f,delim_whitespace=True,skiprows=2,nrows=sizes.loc[0,'qsize'],names=['q'])
  q = q.loc[:,'q'].values
  q = np.around(q,decimals=2)
  E = pd.read_csv(f,delim_whitespace=True,skiprows=2+sizes.loc[0,'qsize'],nrows=sizes.loc[0,'Esize'],names
    =['E'])
  E = E.loc[:,'E'].values
  E = np.around(E,decimals=2)
  data = pd.read_csv(f,delim_whitespace=True,skiprows=3+sizes.sum(1)[0],
          nrows=sizes.loc[0,'Esize'],names=q)
  data.index=E
  errors = pd.read_csv(f,delim_whitespace=True,skiprows=3+sizes.sum(1)[0]+sizes.loc[0,'Esize'],
          nrows=sizes.loc[0,'Esize'],names=q)
  errors.index=E
  return(q,E,data,errors)

def EmptyCorrection(emptypath,data,errors):
  '''Reads the emtpy data and corrects the smaple data from the empty
    IN:
```

```
        emptypath:      path to the empty data (string)
        data:          I(q,E) data for the sample (pandas DataFrame of float)
        errors:        I(q,E) error data for the sample (pandas DataFrame of float)
    OUT:
        corrdata:      Empty corrected data (pandas DataFrame of float)
        correrr:        Empty corrected data error (pandas DataFrame of float)'''

  if emptypath != None:
    q,E,datae,errorse = readdata(emptypath)
    corrdata = data-datae
    correrr = np.sqrt(np.square(errors)+np.square(errorse))
  else:
    corrdata = data
    correrr = errors
  return(corrdata,correrr)

def detailedBalance(Temp,data,errors,Temperr=None,Ecut=None):
  '''Performs the detailed balance correction on the input data and errors using temperature Temp
    IN:
        Temp:      sample temperature (float)
        data:      I(q,E) data (pandas DataFrame float)
        errors:    I(q,e) errors (pandas DataFrame float)
        Temperr:   [optional] error in sample temperature (float)
        Ecut:      [optional] region to exclude from detailed balance calculation [Ecut,Emax] (float)
    OUT:
        dbdata:    I(q,E) with detailed balance (pandas DataFrame float)
        dberrors: I(q,E) errors with detailed balance (pandas DataFrame float)'''

  kb = 0.0861733 #meV/Kelvin
  E = data.index.values
  dbdata = data.copy(deep=True)
  dberrors = errors.copy(deep=True)
  if Ecut!=None:
    dbdata.loc[slice(Ecut,None),:] = np.nan
  if Temperr is None:
    for i in E[E<0]:
      ind = dbdata.loc[-i,:].isnull()
      dbdata.loc[-i,ind] = dbdata.loc[i,ind]*np.exp(-i/(kb*Temp))
      dberrors.loc[-i,ind] = dberrors.loc[i,ind]*np.exp(-i/(kb*Temp))
  else:
    for i in E[E<0]:
      ind = dbdata.loc[-i,:].isnull()
      dbdata.loc[-i,ind] = dbdata.loc[i,ind]*np.exp(-i/(kb*Temp))
      y = np.sqrt(np.square(dberrors.loc[i,ind]/dbdata.loc[i,ind])+np.square((i*Temperr)/(kb*Temp*Temp)))
      dberrors.loc[-i,ind] = dbdata.loc[-i,ind]*y
  return(dbdata,dberrors)

@njit
def trapze(y,x,yerr,ire=True):
  '''Trapezoidal integration routine which includes an error calculation
    IN:
        y:       f(x) values to integrate over (numpy array of float)
        x:       x values for the integral (numpy array of float)
        yerr:    error values for f(x) (numpy array of float)
        ire:     sets errors to be independent and random (boolean)
    OUT:
        s/2.0:  trapezoidal integration of y over x (float)
        e:       error of the integration (float)'''

  yind = np.isfinite(y)
  if np.any(~yind):
    y = y[yind]
    x = x[yind]
    yerr = yerr[yind]
  yerrind = np.isfinite(yerr)
  if np.any(~yerrind):
      yerr[~yerrind] = 0.02*y[~yerrind]
  s = 0.0
  e = 0.0
  for i in range(1,len(x)):
    xval = x[i]-x[i-1]
    yval = y[i]+y[i-1]
    z = xval*yval
    s += z
    if ire:
      yvalerr = np.sqrt(np.square(yerr[i])+np.square(yerr[i-1]))
      zerr = np.abs(xval)*yvalerr
      e += np.square(zerr)
    else:
      yvalerr = yerr[i]+yerr[i-1]
      zerr = np.abs(xval)*yvalerr
      e += zerr
  if ire:
    e = np.sqrt(e)/2.0
  else:
    e = e/2.0
  return(s/2.0,e)

@njit
def FTe_E2t(data,errors,q,E,t,Eregion,ire):
  '''Fourier transfrom of S(q,E) data to F(q,t)
    IN:
```

```
183         data:     S(q,E) data (numpy qn by En array of float)
184         errors:   S(q,E) error data (numpy qn by En array of float)
185         q:        momentum transfer data (numpy array of float)
186         E:        energy transfer data (numpy array of float)
187         t:        time data (numpy array of float)
188         Eregion:    bounds for energy transfer region (array of float)
189         ire:      calculate errors as independent and random (boolean)
190       OUT:
191         ftdata:   F(q,t) Fourier transformed data (2D numpy array of float)
192         fterrors:   F(q,t) error data (2D numpy array of float)'''
193
194     hbar = 0.658212 #meV*ps
195     M,N = data.shape
196     L = len(t)
197     ftdata = np.zeros((L,N))
198     ftdataerr = np.zeros((L,N))
199     Einds = np.where((E<=Eregion[1])&(E>=Eregion[0]))[0]
200     x = E[Einds]/hbar
201     y = data[Einds,:]
202     yerr = errors[Einds,:]
203     for i in range(L):
204       for j in range(N):
205         z = np.cos(x*t[i])*y[:,j]
206         zerr = np.abs(np.cos(x*t[i]))*yerr[:,j]
207         ftdata[i,j],ftdataerr[i,j] = trapze(z,x=x,yerr=zerr,ire=ire)
208     return(ftdata,ftdataerr)
209
210 def FTEt_wrapper(data,errors,q,E,t,Eregion,ire):
211     '''Performs the Fourier Transform energy to time and places the output in a pandas dataframe
212       IN:
213         data:     S(q,E) data (numpy qn by En array of float)
214         errors:   S(q,E) error data (numpy qn by En array of float)
215         q:        momentum transfer data (numpy array of float)
216         E:        energy transfer data (numpy array of float)
217         t:        time data (numpy array of float)
218         Eregion:    bounds for energy transfer region (array of float)
219         ire:      calculate errors as independent and random (boolean)
220       OUT:
221         ftdata:   F(q,t) Fourier transformed data (pandas DataFrame of float)
222         fterrors:   F(q,t) error data (pandas DataFrame of float)'''
223
224     ftdata,fterrors = FTe_E2t(data.values,errors.values,q,E,t,Eregion,ire)
225     ftdata = pd.DataFrame(ftdata,index=t,columns=q)
226     fterrors = pd.DataFrame(fterrors,index=t,columns=q)
227     return(ftdata,fterrors)
228
229 @njit
230 def FTe_q2r(data,errors,t,q,r,qregion,ire):
231     '''Fourier transfrom of F(q,t) data to G(r,t)
232       IN:
233         data:     F(q,t) data (numpy 2D array of float)
234         errors:   F(q,t) error data (numpy 2D array of float)
235         t:        time data (numpy array of float)
236         q:        momentum transfer data (numpy array of float)
237         r:        position data (numpy array of float)
238         qregion:    bounds for momentum transfer region (array of float)
239         ire:      calculate errors as independent and random (boolean)
240       OUT:
241         ftdata:   G(r,t) Fourier transformed data (2D numpy array of float)
242         fterrors:   G(r,t) error data (2D numpy array of float)'''
243
244     M,N = data.shape
245     L = len(r)
246     ftdata = np.zeros((M,L))
247     fterrors = np.zeros((M,L))
248     qinds = np.where((q<=qregion[1])&(q>=qregion[0]))[0]
249     x = q[qinds]
250     y = data[:,qinds]
251     yerr = errors[:,qinds]
252     for i in range(L):
253       for j in range(M):
254         z = x*np.sin(x*r[i])*y[j,:]/r[i]
255         zerr = np.abs(x*np.sin(x*r[i])/r[i])*yerr[j,:]
256         ftdata[j,i],fterrors[j,i] = trapze(z,x=x,yerr=zerr,ire=ire)
257     ftdata = ftdata/(2.*np.pi*np.pi)
258     fterrors = fterrors/(2.*np.pi*np.pi)
259     return(ftdata,fterrors)
260
261 def FTqr_wrapper(data,errors,t,q,r,qregion,dens,denserr,ire):
262     '''Performs the Fourier Transform momentum transfer to position and places the output in a pandas
        dataframe
263       IN:
264         data:     F(q,t) data (numpy 2D array of float)
265         errors:   F(q,t) error data (numpy 2D array of float)
266         t:        time data (numpy array of float)
267         q:        momentum transfer data (numpy array of float)
268         r:        position data (numpy array of float)
269         qregion:    bounds for momentum transfer region (array of float)
270         dens:     Sample densiity (float)
271         denserr:    error in sample density (float)
272         ire:      calculate errors as independent and random (boolean)
273       OUT:
```

```
        ftdata:   G(r,t) Fourier transformed data (2D numpy array of float)
        fterrors:   G(r,t) error data (2D numpy array of float)'''

  ftdata,fterrors = FTe_q2r(data.values,errors.values,t,q,r,qregion,ire)
  ftgdata = pd.DataFrame(ftdata,index=t,columns=r)/dens
  ftgerrors = np.abs(ftdata/dens)*np.sqrt(np.square(fterrors/ftdata)+np.square(denserr/dens))
  ftgerrors = pd.DataFrame(ftgerrors,index=t,columns=r)
  return(ftgdata,ftgerrors)

def ResFunc(path,emptypath,temp,t,Eregion,qregion,vanEcut,ire):
  '''Creates the resolution function from vanadium data (empty corrected)
    IN:
        path:       path for the vanadium scattering data (string)
        emptypath:    path for the empty scattering data (string)
        temp:     temperature for detailed balance [not currently used] (float)
        t:          time data (numpy array of float)
        Eregion:      energy region to Fourier transform over (array of float)
        qregion:      momentum transfer region to Fourier transform over (array of float)
        vanEcut:    energy region to limit detailed balance [not currently used] (float)
        ire:        calculate errors as independent and random (boolean)
    OUT:
        ftdata:     F(q,t) vanadium resolution data (pandas DataFrame of float)
        fterrors:     F(q,t) vanadium resolution data errors (pandas DataFrame of float)'''

  q,E,data,errors = readdata(path)
  data,errors = EmptyCorrection(emptypath,data,errors)
  data = data.loc[slice(Eregion[0],Eregion[1]),slice(qregion[0],qregion[1])]
  errors = errors.loc[slice(Eregion[0],Eregion[1]),slice(qregion[0],qregion[1])]
  q = data.columns.values
  E = data.index.values
  ftdata,fterrors = FTEt_wrapper(data,errors,q,E,t,Eregion,ire)
  return(ftdata,fterrors)

def Normalize_fqt(sqpath,qlimits,fqt,fqterr,verbose=False):
  '''Performs the normalization to real units of the sample data using previously measured S(q) data
    IN:
        sqpath:     path for the S(q) data (string)
        qlimits:      limits for the range in q-space (array of float)
        fqt:        Intemediate scattering function to fit (pandas DataFrame of float)
        fqterr:     Error in intermediate scattering function (pandas DataFrame of Float)
        verbose:    Turn on to plot fit and print fit report (boolean)
    OUT:
        normfqt:      Intermediate scattering function with norm factor applied (pandas DataFrame of float
    )
        normfqterr:   Error in new Intermediate scattering function (pandas DataFrame of float)
        norm:     Normalization factor (float)
        normerr:      Error in normalization factor (float)'''

  def residualnorm(pars,x,y0,data=None,eps=None):
    # Fitting function y=A*F(q,t=0)
    parvals = pars.valuesdict()
    amp = parvals['amp']
    model = y0*amp
    if data is None:
      return(model)
    if eps is None:
      return(model-data)
    return((model-data)/eps)

  def norm_value(sqpath,x,y,yerr,verbose=False):
    '''Performs the fitting to determine the normalization factor by using a spline on the S(q) data
    to match the F(q,t=0) points.'''
    sqdata = pd.read_csv(sqpath,delim_whitespace=True,skiprows=4,index_col=0,usecols=[0,1,2],names=['q','
    Sq','Err'])
    splinerep = splrep(sqdata.index.values, sqdata.loc[:,'Sq'], s=0)
    yspline = splev(x, splinerep, der=0)

    params = Parameters()
    params.add('amp',value=1.0)
    out = minimize(residualnorm, params, args=(x,y), kws={'data':yspline,'eps':yerr})
    if verbose:
      fig,ax1 = plt.subplots(figsize=(10,10))
      ax1.plot(x,yspline, label='$S(q)$ Data')
      ax1.plot(x,residualnorm(out.params,x,y),linestyle='none',marker='.',label='Fitted $F(q,0)$ Data')
      ax1.axhline(y=1.0,xmin=0.0,xmax=1.0,linestyle='--',color='black')
      ax1.set_ylabel(r'$S(q)$')
      ax1.set_xlabel(r'Momentum Transfer, q [$\mathrm{\AA}^{-1}$]')
      ax1.legend(fontsize=20)
      plt.show()
      print(fit_report(out))
    return(out.params['amp'].value,out.params['amp'].stderr)

  ind = fqt.index.values[0]
  x = fqt.loc[ind,slice(qlimits[0],qlimits[1])].index.values
  y = fqt.loc[ind,slice(qlimits[0],qlimits[1])].values
  yerr = fqterr.loc[ind,slice(qlimits[0],qlimits[1])].values
  norm,normerr = norm_value(sqpath,x,y,yerr,verbose=verbose)
  normfqt = fqt*norm
  normfqterr = np.abs(normfqt)*np.sqrt(np.square(fqterr/fqt)+np.square(normerr/norm))
  return(normfqt,normfqterr,norm,normerr)

def separate_fqt(fqt,fqterr,t,q,qlimits):
```

```
  '''Performs the fitting to separate the self and distinct parts of the intermediate scattering function
    IN:
        fqt:      Intermediate scattering function to be fit (pandas DataFrame of float)
        fqterr:   Error in intermediate scattering function (pandas DataFrame of float)
        t:        array of time values (numpy array of float)
        q:        array of momentum transfer values (numpy array of float)
        qlimits:    limits for the q-region (array of float)
    OUT:
        fsqt:     Self intermediate scattering function (pandas DataFrame of float)
        fsqterr:    error in the self intermediate scattering function (pandas DataFrame of float)
        fdqt:     Distinct intermediate scattering function (pandas DataFrame of float)
        fdqterr:    error in the distinct intermediate scattering function (pandas DataFrame of float)
        widthdat: array of width fit parameter values (numpy array of float)
        ampdat:   array of amplitude fit parameter values (numpy array of float)'''

  def residual(pars,x,data=None,eps=None):
    # Fitting function y = A*exp(-w*x^2)
    parvals = pars.valuesdict()
    amp = parvals['amp']
    width = parvals['width']
    model = amp*np.exp(-width*x*x)
    if data is None:
      return(model)
    if eps is None:
      return(model-data)
    return((model-data)/eps)

  params = Parameters()
  params.add('amp',value=1.0,vary=True)
  params.add('width',value=1.0E-1,min=0.0)

  M,N = fqt.shape
  fsqt = np.zeros([M,N])
  fsqterr = np.zeros([M,N])
  x = fqt.loc[t[0],slice(qlimits[0],qlimits[1])].index.values
  widthdat = np.zeros([len(t),2])
  ampdat = np.zeros([len(t),2])
  for n,i in enumerate(t):
    y = fqt.loc[i,slice(qlimits[0],qlimits[1])].values
    yerr = np.exp(-x/2.0) #Forces fitting to long q tail
    out = minimize(residual, params, args=(x,), kws={'data':y,'eps':yerr})
    A = out.params['amp'].value
    Aerr =out.params['amp'].stderr
    w = out.params['width'].value
    werr = out.params['width'].stderr
    widthdat[n,:] = [w,werr]
    ampdat[n,:] = [A,Aerr]
    fsqt[n,:] = residual(out.params,q)
    try:
      fsqterr[n,:] = np.abs(fsqt[n,:])*np.sqrt(np.square(Aerr/A)+np.square(q*q*werr)-2.*q*q*out.covar
     [1,1]/A)
    except TypeError:
      fsqterr[n,:] = np.abs(fsqt[n,:])*np.sqrt(np.square(Aerr/A)+np.square(q*q*werr))
  fsqt = pd.DataFrame(fsqt,index=t,columns=q)
  fsqterr = pd.DataFrame(fsqterr,index=t,columns=q)
  fdqt = fqt-fsqt
  fdqterr = np.sqrt(np.square(fqterr)+np.square(fsqterr))
  return(fsqt,fsqterr,fdqt,fdqterr,widthdat,ampdat)

def get_gsrt(width,amp,t,r):
  '''Calculates the self Van Hove correlation function analytically from fit parameters
    IN:
        width:    array of width fit parameter values (numpy array of float)
        amp:      array of amplitude fit parameter values (numpy array of float)
        t:        array of time values (numpy array of float)
        r:        position data (numpy array of float)
    OUT:
        gsrt:     Self Van Hove function (pandas DataFrame of float)
        gsrterr:    error in the self Van Hove function (pandas DataFrame of float'''

  M,N = (len(t),len(r))
  gsrt = np.zeros([M,N])
  gsrterr = np.zeros([M,N])
  for i in range(M):
    gsrt[i,:] = amp[i,0]*np.exp(-(r*r)/(4*width[i,0]))/(4.*np.pi*width[i,0])**(3./2.)
    gsrterr[i,:] = gsrt[i,:]*((r*r-6.*width[i,0])/(4*np.square(width[i,0])))*width[i,1]
  gsrt = pd.DataFrame(gsrt,index=t,columns=r)
  gsrterr = pd.DataFrame(gsrterr,index=t,columns=r)
  return(gsrt,gsrterr)

################################## INPUTS ######################################
path = 'H:\\ARCS2017\\20180612_Zr80Pt20_wRes\\'
#********************* Empty Chamber Input Options ************************#
emptypath = None

#*********************** Vanadium Input Options ***************************#
vanpath = path+'20180330_Vanadium_run_number_95518_iofqearray.dat'
vantemp = 295.    #Vanadium temperature in Kelvin
vanECut = 10.0    #High energy cutoff for vanadium

#*********************** Sample Input Options ***************************#
datapath = path+'20171002_Zr80Pt20_20meV_plus_350C_run_number_95534_iofqearray.dat'
```

```
temp = 1560.+273.          #Sample temperature in Kelvin
temperr = 48.              #Error in sample temperature
Ecut = 15.0               #High energy cutoff for the sample
t = makevariable(0.0,3.0,0.02)
r = makevariable(0.1,15.0,0.05)
Eregion = [-60.0,60.0]         #Region in energy space to use
qregion = [1.5,5.5]          #Region in q space to use
dens = 0.04436             #Number density in atoms/Angstrom^3
denserr = 0.02*dens          #Number density error
ire = True

#********************** Normalization Options*****************************#
sqpath = 'H:\\BESL2016\\Zr80Pt20\\Step_Hold\\Curvature_Corrected\\
    STL16059_Increment_1_Step_1544C_11_19_peaks.S_sm.S.dat'
qlimits = [1.5,5.5]          #Limits for S(q) should be the same as qregion

#********************** Actual Analysis ***************************#
q,E,data,errors = readdata(datapath)
data,errors = EmptyCorrection(emptypath,data,errors)
dbdata,dberrors = detailedBalance(temp,data,errors,temperr,Ecut)
fqtdata,fqterrors = FTEt_wrapper(dbdata,dberrors,q,E,t,Eregion,ire)
res,reserr = ResFunc(vanpath,emptypath,vantemp,t,[-60.,15.],[1.0,2.5],vanECut,ire=True)
reserr = np.nanstd(res,axis=1)
res = np.nanmean(res,axis=1)
fqtres = fqtdata.divide(res,axis=0)
fqtreserr = np.abs(fqtres)*np.sqrt(np.square(fqterrors/fqtdata).add(np.square(reserr/res),axis=0))
normfqtres,normfqtreserr,norm,normerr = Normalize_fqt(sqpath,qlimits,fqtres,fqtreserr,verbose=True)
fsqt,fsqterr,fdqt,fdqterr,widthdat,ampdat = separate_fqt(normfqtres,normfqtreserr,t,q,qlimits)
gdrt,gdrterr = FTqr_wrapper(fdqt,fdqterr,t,q,r,qregion,dens,denserr,ire)
gsrt,gsrterr = get_gsrt(widthdat,ampdat,t,r)
gtrt,gtrterr = FTqr_wrapper(normfqtres,normfqtreserr,t,q,r,qregion,dens,denserr,ire)
```

A.3 References

[1] O. Arnold et al. Mantid - Data analysis and visualization package for neutron scattering and μ SR experiments. *Nuclear Instruments and Methods in Physics Research, Section A: Accelerators, Spectrometers, Detectors and Associated Equipment* **764**, (2014). DOI: 10.1016/j.nima.2014.07.029. arXiv: 1407.5860.

[2] U. Dahlborg, W. Gudowski, and M. Davidovic. Van Hove correlation functions from coherent neutron inelastic scattering. *Journal of Physics: Condensed Matter* **1**,35 (1989). DOI: 10.1088/0953-8984/1/35/016.

Appendix B: Guide to LAMMPS

This appendix gives a brief overview of how to run Large-scale Atomic/Molecular Massively Parallel Simulator (LAMMPS) [1] simulations on the Physics department high-performance computing (HPC) and details the code already developed to compute common quantities. For more in depth questions about LAMMPS see the manual (`https://lammps.sandia.gov/doc/Manual.html`). It should be immediately noted that the code developed here to analyze the MD data has not been optimized for speed and memory management but was created out of necessity and could benefit from this optimization. Section B.1 details how to run simulations on the HPC, section B.2 details some Python code to analyze the simulation data for common quantities and Section B.3 lists systems which I have simulated using LAMMPS.

B.1 Running Simulations on the HPC

This section provides details on running a LAMMPS simulation on the Washington University physics department HPC. Table B.1 contains links and descriptions for programs and repositories, which are useful for accessing the cluster and running LAMMPS simulations in general. Subsection B.1.1 gives information about running LAMMPS on the HPC cluster while subsection B.1.2 gives example LAMMPS input code for various simulations.

Name	Link	Description
LAMMPS	`https://lammps.sandia.gov/`	Main LAMMPS website with links for the manual, tutorials, program downloads, and more.
NIST Potential Repository	`https://www.ctcms.nist.gov/potentials/`	Contains LAMMPS style potentials for EAM simulations

H. Sheng Potential Repository	https://sites.google.com/site/eampotentials/	Contains LAMMPS style potentials for EAM simulations made by H. Sheng
OVITO	https://ovito.org/	Ovito is an analysis and visualization program particularly useful for analysis of LAMMPS dump files
Anaconda	https://www.anaconda.com/download/	Python package manager and data science platform
Cyberduck	https://cyberduck.io/	Used as an SFTP file transfer protocol to move files to and from the HPC sever.
PuTTY	https://www.putty.org/	Popular SSH client useful for windows users

Table B.1: This table contains a summary of useful links for running LAMMPS simulations and analyzing/visualizing the output.

B.1.1 LAMMPS and HPC Guide

The physics department HPC consists of 19 networked computing nodes which is accessible via an SSH client, e.g. PuTTY. A list of these computing nodes can be found on the physics department intranet but it is sufficient to remember a single node. An account is necessary to log in to the cluster and can be set up by contacting the Scientific Supervisor of Computing, who at the time of writing this is Sai Iyer. Once an account is created one can log in using PuTTY by launching the program and directing it to the host name **io.wustl.edu**, or any other node, and port 22. This will then prompt the user for the username and password. If not using PuTTY the user needs to preemptively specify the username by typing **ssh usernameio.wustl.edu**. This will log you into the **io** cluster node.

LAMMPS is a demanding program that will require most of the resources of the cluster node so it is pertinent to select one which is mostly idle. To determine which nodes are potentially idle use the **hpcload** command, which prints a list of the nodes, CPUs, RAM, and load over three different intervals. The load column is of interest in determining which

```
login as: ashcraftr
ashcraftr@io.wustl.edu's password:
Last login: Thu Dec 27 17:56:41 2018 from
[ashcraftr@io ~]$ hpcload
HOST         CPUs  RAM (GB)    Load (1 min, 5 min, 15 min)

adrastea       40       256    36.12, 36.08, 36.06
amalthea       40       256    23.28, 23.43, 24.57
callisto       40       256    36.98, 37.92, 40.77
cassini        40       256    4.39, 4.19, 4.18
europa         64       128    17.23, 17.09, 17.10
galileo        32       128    36.56, 36.27, 36.71
ganymede       40       256    66.60, 67.44, 70.43
io             40       256    10.68, 10.35, 10.29
jovian         64       128    0.10, 0.14, 0.13
jupiter        32       256    31.52, 31.30, 31.48
marduk         48       256    0.57, 0.36, 0.15
megadon        32        64    0.17, 0.12, 0.13
metis          40       256    39.81, 38.95, 42.28
monolith       48       256    4.01, 4.08, 4.12
parsley        40       256    0.09, 0.14, 0.13
rosemary       40       256    27.59, 27.91, 27.88
sage           40       256    0.00, 0.07, 0.12
thebe          40       256    0.00, 0.05, 0.29
thyme          40       256    8.73, 8.77, 8.78
[ashcraftr@io ~]$ ssh sage
Last login: Thu Dec 27 18:16:02 2018 from io.wustl.edu
[ashcraftr@sage ~]$
```

Figure B.1: Example of logging into the physics department HPC cluster using my username ashcraftr. The command **hpcload** is run to examine the load on all nodes on the cluster. Ganymede (red) shows a rather high and sage (green) shows a low load (compared to the CPUs column). Sage is then chosen and logged in to.

nodes are idle. The load is nominally around 0 indicating the node is idle while a load greater than this indicates the node is in use (typically a number near the CPUs column value indicates the node is completely in use but values above the number of CPUs is possible). Changing to a new node can be done using the **ssh** command from the current terminal, i.e. **ssh sage.wustl.edu** will change the current node to sage. Chose the node with the lowest load and **ssh** to it. These steps are shown in Fig. B.1

Once logged into a node with low load you need to check that there are either no programs running or that there are very few. It could be the case that there are many programs running but which only exhibit a high load briefly, which would be detrimental to running LAMMPS.

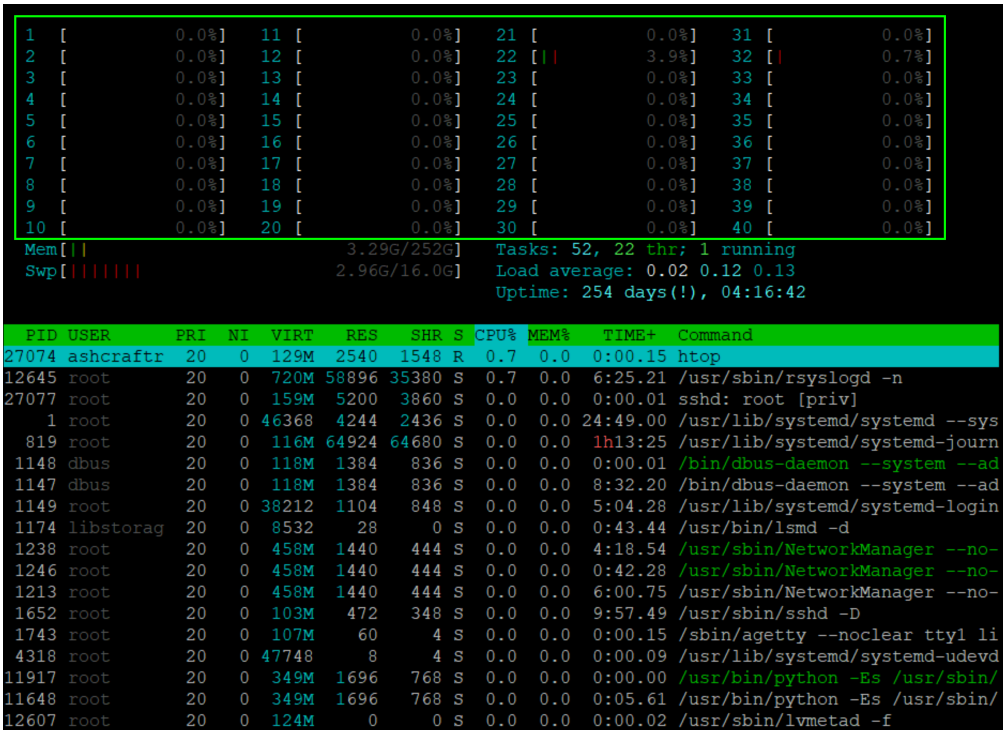

Figure B.2: Example of the htop command which lists many properties of the current nodes current processes. The current process is highlighted in blue, the green highlighted text gives the column headers for the lower part of the terminal, and the green box at the top shows the location of the CPU usage.

Running the command **htop** gives a lot of information about what is running and who is running it on the node. A typical idle node is shown in Fig. B.2. To contrast the idle node a busy node would have many processes listed by one or several users and will typically have higher values for the CPUs at the top of the screen (green box). To exit this screen use the **F10** key (options are listed at the bottom of the screen). If the terminal looks like Fig. B.2 it is likely a good choice to run your simulations on.

If the current node is determined to be good you need to navigate to the file which you want to run LAMMPS in and which contains the LAMMPS input file (discussed in the next subsection). This is done with the typical Linux change directory command, i.e. **cd /grad/username/directory/**. The mpi module used to run LAMMPS in parallel needs to be loaded with the command **module load mpi/openmpi-x86_64**. Finally, before running LAMMPS a screen environment should be created with **screen -S screen_name**,

where **screen_name** is a user chosen identifier. This creates an environment similar to the previous terminal that can be exited without killing the process in the terminal. The screen is exited using **ctrl+a+d** and can be rejoined using the terminal command **screen -R screen_name**. If the screen name is forgotten a list of current screens on the node can be printed to the screen using the command **screen -ls**. To close a screen completely type **exit** in the screen terminal. Other information about the screen environment can be found online in various locations.

Running a LAMMPS simulation in the previously setup screen environment is done with the command **mpirun -np n_cpus -*in in.**** where ***in.**** is the name of the input LAMMPS file. The flag **-np** signifies that the following number is the number of CPUs (n_cpus) to use to run the LAMMPS simulation. The input file name is preceded by the flag **-in**. The input file needs to be placed in the current directory typically using an SFTP program, i.e. Cyberduck, to move the file onto the cluster. After running this command LAMMPS should start printing information to the screen and creating any files requested in the simulation along with the *log.lammps* file, which contains all the information printed to the screen.

B.1.2 LAMMPS Input Codes

The code shown in Listing B.1 creates a simulation box with periodic boundary conditions of the given size where the units are defined by the metal LAMMPS unit system. The *NiZr_Mendelev_2012.eam.fs* potential is used for the Zr and Ni atoms. Atoms are randomly filled in the simulation region using the specified proportions and random seed numbers. A file *temp.txt* is created which stores some thermostyle variables. An energy minimization routine is run to reduce the magnitude of the force applied to close atoms at the beginning of the simulation (no dynamics are run at this step). The system is evolved at a relatively high temperature for a short time before being cooled at a specified rate. Binary files used to restart the simulation from the given time step are saved periodically during cooling so any temperature can be restarted and simulated quickly.

```
#------------------------------ Initialization ------------------------------
units metal   #Define the units to use in the simulation
boundary p p p    #Set all the boundarys for the simulation cell to be periodic
atom_style atomic   #Defines the style of simulation to run (default attributes for atoms)
timestep 0.005    #Defines default time step in uints defined by metal
region Box block -38 38 -38 38 -38 38   #Creates a region (called Box) in the simulation cell
create_box 2 Box    #Creates a simulation cell for the region Box containing 2 atom types

#------------------------------ Atom Definition ------------------------------
pair_style eam/fs     #Sets the pair potential style to EAM/FS
pair_coeff * * /grad/ashcraftr/Potentials/NiZr_Mendelev_2012.eam.fs Ni Zr   #Sets the pair coefficients
     using the file specified
create_atoms 1 random 5400 475652 Box   #Creates 5400 atoms in Box of type 1 using a random generation
     scheme
create_atoms 2 random 9600 5678 Box   #Creates 9600 atoms in Box of type 2 using a random generation
     scheme

#------------------------------ Settings ------------------------------
variable Temperature equal temp   #Creates a variable to store temp
variable TimeStep equal step    #Creates a variable to store step
variable Volume equal vol   #Creates a variable to store vol
variable Density equal density    #Creates a variable to store density
variable s equal stride(100000,1130000,30000)   #Creates a variable using the stride function

run_style verlet    #Sets the time integrator to use the velocity-Verlet algorithm
thermo 100      #Compute and print thermo variables every this many timesteps
fix thermo_print all print 100 "${TimeStep} ${Temperature} ${Volume} ${Density}" append Temp.txt title ""
     screen no   #Prints thermostyle variables to Temp.txt

#------------------------------ Runs Simulation ------------------------------
minimize 0.0 0.0 500 500    #Performs an energy minimization by moving atoms (needed to reduce overlap)

restart v_s restart.*.cooling   #Create restart files at timesteps defined by the variable s defined above
fix Thermostat all npt temp 3000 3000 0.5 iso 0 0 5.0   #Create a thermostat with the npt ensemble setting
     temperature initial and final and pressure
run 100000 upto   #Run the simulation upto the stated timestep

fix Thermostat all npt temp 3000 100 0.5 iso 0 0 5.0    #Create a thermostat with the npt ensemble setting
     temperature initial and final and pressure
run 1000000   #Run the simulation for the stated number of timesteps
```

Listing B.1: An example input file, *in.ZrNi_Initial*, for an initial LAMMPS simulation of $Zr_{64}Ni_{36}$ liquid.

In Listing B.2 one of these restart files (in particular the one located closest to 2000 K) is read in and the simulation restarted and run for a relatively long time (order of nanoseconds). This simulation makes another restart file at the end which contains, if the time was long enough, the steady state liquid system. This is checked by examining the time dependence of thermostyle variables.

```
#------------------------------ Initialization ------------------------------
read_restart restart.*.cooling remap    #Reads the restart file with the highest timestep value in place
     of *
pair_style eam/fs   #One of the options the restart file does not keep
pair_coeff * * /grad/ashcraftr/Potentials/NiZr_Mendelev_2012.eam.fs Ni Zr   #Sets the pair coefficients
     using the file specified
timestep 0.005    #Defines default time step in uints defined by metal

#------------------------------ Settings ------------------------------
variable CurrentTemp equal 2000   #Creates a variable to store 2000
variable Temperature equal temp   #Creates a variable to store temp
variable TimeStep equal step    #Creates a variable to store step
variable Volume equal vol   #Creates a variable to store vol
variable Density equal density    #Creates a variable to store density

run_style verlet    #Sets the time integrator to use the velocity-Verlet algorithm
thermo 100    #Compute and print thermo variables every this many timesteps
fix thermo_print all print 100 "${TimeStep} ${Temperature} ${Volume} ${Density}" append Temp.txt title ""
     screen no   #Prints thermostyle variables to Temp.txt

#------------------------------ Runs Simulation ------------------------------
fix Thermostat all npt temp ${CurrentTemp} ${CurrentTemp} 0.5 iso 0 0 5.0   #Create a thermostat with the
     npt ensemble setting temperature initial and final and pressure
run 3000000   #Run the simulation for the stated number of timesteps

```

```
22 write_restart restart.relaxed.${CurrentTemp}    #Write a restart file at the end of the simulation
```

Listing B.2: An example input file, *in.ZrNi_relaxation*, for the relaxation step of a LAMMPS simulation which continues the simulation started in Listing B.1.

Listing B.3 restarts a relaxed simulation and runs dynamics for a shorter amount of time and saves out dump files. These files contain all the information input on line 14, which in this case are the x, y, z atomic positions, atom id, and the atom element. The element is also changed to match the element name rather than using a numeric identifier. These dump files are then typically analyzed to determine structural and dynamic information. The length of the run and the value of the time step determine which dynamics can be examined in the subsequent analysis.

```
1  #-------------------------------  Variable -------------------------------
2  variable CurrentTemp equal 3000   #Creates a variable to store 3000
3
4  #------------------------------- Initialization -------------------------------
5  read_restart restart.relaxed.${CurrentTemp} remap   #Reads the restart file
6  pair_style eam/fs   #One of the options the restart file does not keep
7  pair_coeff * * /grad/ashcraftr/NiZr_Mendelev_2012.eam.fs Ni Zr    #Sets the pair coefficients using the
       file specified
8  reset_timestep 0    #Resets the timestep to 0
9  timestep 0.002    #Defines default time step in uints defined by metal
10
11 #-------------------------------  Settings -------------------------------
12 run_style verlet    #Sets the time integrator to use the velocity-Verlet algorithm
13
14 dump cfgDump all custom 100 position.*.cfg id element x y z   #Dumps specified variables to an output file
       where * is the timestep
15 dump_modify cfgDump pad 6   #Pads timestep of dump file
16 dump_modify cfgDump element Ni Zr   #Saves atom elements as strings instead of numbers
17
18 thermo 100    #Compute and print thermo variables every this many timesteps
19
20 #-------------------------------  Run Simulation -------------------------------
21 fix Thermostat all npt temp ${CurrentTemp} ${CurrentTemp} 0.5 iso 0 0 5.0   #Create a thermostat with the
       npt ensemble setting temperature initial and final and pressure
22 run 100000    #Run the simulation for the stated number of timesteps
```

Listing B.3: An example input file, *in.ZrNi_cfg*, which saves configuration data files from a LAMMPS simulation. This restarts the simulation performed in Listing B.2.

The above LAMMPS code is a subset of the code written for simulations done in this thesis which should give a good start to most liquid simulations. More code has been written for simulating the viscosity (using the Green-Kubo method), the mean-square-displacement, the local cluster time, structural analysis using Voronoi tessellation, the velocity autocorrelation function, the self intermediate scattering function, and the specific heat. Code for these can be easily developed or can be provided upon request.

B.2 Analyzing Output With Python

Listing B.4 contains an analysis script which can be used to calculate the static partial pair distribution function. This particular version creates the first images of all the data and uses this to calculate the PPCF to a larger distance. This python code is included to give an idea of how the analysis of output LAMMPS data can be accomplished using python on the HPC cluster. Analysis code has been developed for viscosity, structural analysis using Voronoi tessellation, dynamic pair correlation function, local cluster time, mean-square displacement, static structure factor, static pair correlation function, and specific heat. These are available on request.

```
from multiprocessing import Pool
from math import floor
from collections import Counter
import numpy as np
import matplotlib.pyplot as plt
from glob import glob
import itertools
from datetime import datetime
from timeit import default_timer as timer
import matplotlib.pyplot as plt
from functools import partial
import pandas as pd
from numba import njit

def ReadPosition(f):
  '''Function used to read a dump file output from LAMMPS which has the format:
     . . . . . . . . . . . . . . . . . . . . . . . .
     ITEM: TIMESTEP
     100
     ITEM: NUMBER OF ATOMS
     15000
     ITEM: BOX BOUNDS pp pp pp
     -3.0422290969884543e+01 3.0422290969884543e+01
     -3.0422290969884543e+01 3.0422290969884543e+01
     -3.0422290969884543e+01 3.0422290969884543e+01
     ITEM: ATOMS id element x y z
     10148 Nb -26.819 -26.0555 -26.1943
      . . . . . . . . . . . . . . . . . . . . . . . .
     Input: f - File path to dump file
     Output:  data - pandas DataFrame containing index, atom types, and all positions
          L - Simulation box length from LAMMPS dump file'''
  names = ('Atom_Type','X','Y','Z')
  data = pd.read_csv(f,skiprows=9,delim_whitespace=True,names=names,index_col=0)
  data.sort_index(inplace=True)
  data.set_index(np.arange(0,len(data)))
  L = pd.read_csv(f,skiprows=5,delim_whitespace=True,usecols=[1],nrows=1,names='L')['L'][0]
  return(data,L)

def Make_Images(data,L):
  '''Creates all first images (27) of the LAMMPS position data and appends to a new pandas DataFrame.
     Input: data - pandas DataFrame created by ReadPosition function
          L - Size of simulation box (scalar real) output by ReadPosition function
     Output:  dfimages - pandas DataFrame containing original data and all first images'''
  images = [np.array(i) for i in itertools.product([1.,0.,-1.],repeat=3)]
  dfimages = []
  for i in images:
    copy_for_image = data.copy()
    copy_for_image.loc[:,('X','Y','Z')] = copy_for_image.loc[:,('X','Y','Z')]+2*L*i
    dfimages.append(copy_for_image)
  dfimages = pd.concat(dfimages,ignore_index=True)
  return(dfimages)

def atom_type_conversion(data):
  '''Creates the conversion mapping for atom types to integers. Also the inversion back from integers to
     atoms
  is output. Finally all combinations of atomic types are created and output.
     Input: pandas DataFrame of atomic positions and types
```

```
    Output:  conversion - dictionary of {'atom_i': n_i}
          inversion - dictionary of {n_i: 'atom_i'}
          partials - array of atom combinations [[n_0, n_0],[n_0, n_1],...]'''
  uniquevalues = data.loc[:,'Atom_Type'].value_counts()
  conversion = {j:i for i,j in enumerate(uniquevalues.index.values)}
  inversion = {v: k for k, v in conversion.iteritems()}
  partials = np.array(map(list,list(itertools.product(conversion.values(),repeat=2))))
  return(conversion,inversion,partials)

def convert_atom_type(data,conversion):
  '''Converts the Atom_Type column in the pandas DataFrame to integer values according to conversion
    Input: data - pandas DataFrame output from ReadPosition function
          conversion - dictionary from atom_type_conversion function containing str to int conversion rules
    Output:  data - pandas DataFrame with Atom_Type column modified to integer values'''
  for atom_type,atom_num in conversion.iteritems():
    data.loc[data.loc[:,'Atom_Type']==atom_type,'Atom_Type'] = atom_num
  data.loc[:,'Atom_Type'] = data.loc[:,'Atom_Type'].values.astype(int)
  return(data)

def center_atoms(ixyz,L):
  '''Finds the most central atoms (equivalent to the original, non-image, data) within the new array
  containing the images and returns an array of index values.
    Input: ixyz - pandas DataFrame of image position data output from convert_atom_type function
          L - Size of simulation box (scalar real) output by ReadPosition function
    Output:  cind - numpy array of central atom indices'''
  xyz = ixyz.loc[:,('X','Y','Z')].values
  cind = np.where(np.all(xyz<L,axis=1)&np.all(xyz>-L,axis=1))[0]
  return(cind)

def hist_params(low,L,spacing):
  '''Creates the histogram bin parameters
    Input:  low - float for the low value of the distance histogram
          L - Size of simulation box (scalar real) output by ReadPosition function
          spacing - float for the distance spacing and histogram bin spacing
    Output: nbins - integer for number of bins
          limits - array of float for limits of the distance data'''
  hi = np.floor(L/spacing)*spacing
  modhi = np.floor((hi-low)/spacing)*spacing+low
  nbins = int(np.floor((hi-low)/spacing))
  limits = np.array([low,modhi])
  return(nbins,limits)

def min_hist_params(allfiles,low,spacing):
  '''Determines the minimum size of the histogram limits and bins necessary
    Input:  allfiles - list of paths for all configuration files to be read
          low - float for the low value of the distance histogram
          spacing - float for the distance spacing and histogram bin spacing
    Output: nbins - integer for number of bins
          limits - smallest array of float for limits of the distance data'''
  size = []
  for f in allfiles:
    data,L = ReadPosition(f)
    size.append(L)
  size = np.array(size)
  nbins,limits = hist_params(low,size.min(),spacing)
  return(nbins,limits)

def data_matrix(conversion,nbins):
  '''Creates a three dimensional array for storage of the histogram distance data
    Input:  conversion - dictionary of {'atom_i': n_i}
          nbins - integer for number of bins
    Output: mat - NxNxM sized matrix of floats'''
  mat = np.zeros((len(conversion),len(conversion),nbins))
  return(mat)

@njit
def partial_histogram(atom_types,XYZ,cind,limits,nbins,mat,partials):
  '''Creates the histogram of partial pair correlation distances
  Input:  atom_types - numpy array of atom types
        XYZ - numpy array of floats for atomic positions
        cind - numpy array of central atom indices
        limits - array of float for limits of the distance data
        nbins - integer for number of bins
        mat - NxNxM sized matrix of floats
        partials - array of atom combinations [[n_0, n_0],[n_0, n_1],...]
  Output: mat - NxNxM sized matrix of floats containing the ppcf data
        r - numpy array of floats for the radial distance'''
  for i in cind:
    dist = np.sqrt(np.square(XYZ-XYZ[i]).sum(axis=1))
    for j in range(len(partials)):
      m = partials[j,0]
      n = partials[j,1]
      if atom_types[i]==m:
        pdist = dist[np.where(atom_types==n)[0]]
        counts,bins = np.histogram(pdist,bins=nbins,range=limits)
        mat[m,n] += counts
  dr = np.diff(bins)
  N = len(cind)
  for i in range(len(partials)):
    a = partials[i,0]
    b = partials[i,1]
```

```
148     Na = (atom_types[cind]==a).sum()
149     Nb = (atom_types[cind]==b).sum()
150     mat[a,b] = mat[a,b]/(4.0*np.pi*Na*Nb*dr)
151   r = bins[:-1]+dr/2.0
152   mat = mat/(r*r)
153   return(mat,r)
154
155 def wrapper_func(conversion,limits,nbins,partials,f):
156   '''Function which reads and analyzes a single file to determine the partial pair correaltion histogram
157     Input:  conversion - dictionary from atom_type_conversion function containing str to int conversion
          rules
158           limits - array of float for limits of the distance data
159           nbins - integer for number of bins
160           partials - array of atom combinations [[n_0, n_0],[n_0, n_1],...]
161           f - string for configuration file path
162     Output: mat - NxNxM sized matrix of floats containing the ppcf data
163           bins - numpy array of floats for the radial distance'''
164   data,L = ReadPosition(f)
165   data = convert_atom_type(data,conversion)
166   ixyz = Make_Images(data,L)
167   cind = center_atoms(ixyz,L)
168   mat = data_matrix(conversion,nbins)
169   mat,bins = partial_histogram(ixyz.loc[:,'Atom_Type'].values,
170                   ixyz.loc[:,('X','Y','Z')].values,
171                   cind,limits,nbins,mat,partials)
172   mat = ((2.0*L)**3.0)*mat
173   return(mat,bins)
174
175 def aggregate_data(all_data):
176   '''Calculates the mean value of the distance and partial pair correlation function. The error in gr
177   is calculated from the standard deviation
178     Input:  all_data - array containing output from wrapper_func for all files examined
179     Output: r.mean(0) - numpy array for mean distance values
180           gr.mean(0) - numpy array for mean ppcf data
181           gr.std(0) - numpy array for the standard deviation of the ppcf data'''
182   gr = np.array([i[0] for i in all_data])
183   r = np.array([i[1] for i in all_data])
184   return(r.mean(0),gr.mean(0),gr.std(0))
185
186 def prepare_output(r,ppcf,ppcf_err):
187   '''Prepares the final data to be placed into a pandas dataframe which can be used to output
188   the data
189   Input:  r - numpy array of float containing distance values
190         ppcf - numpy array of float containing ppcf data
191         ppcf_err - numpy array of float containing errors for the ppcf data
192   Output: output - pandas DataFrame containing all input data'''
193   output = [r]
194   names = ['r']
195   for i in partials:
196     output.append(ppcf[i[0],i[1]])
197     names.append(inversion[i[0]]+inversion[i[1]])
198     output.append(ppcf_err[i[0],i[1]])
199     names.append(inversion[i[0]]+inversion[i[1]]+'_err')
200   output = pd.DataFrame(np.array(output).T,columns=names)
201   return(output)
202
203 #--------------------- Input Parameters ----------------------------------
204 Temp = '2000'   #Temperature for the data being analyzed
205 inpath = os.getcwd()+'/'    #Set path to the current directory
206 poolnum = 4   #Number of CPUs to use
207 spacing = 0.02    #Spacing of histogram data
208 low = 0.01    #Smallest distance to consider in the histogram
209
210 #---------------------- Program Start ------------------------------------
211 if __name__ == '__main__':
212   p = Pool(poolnum)
213   allfiles = glob(inpath+'position.*.cfg')[:4]
214   #Preperatory items
215   data,L = ReadPosition(allfiles[0])
216   conversion,inversion,partials = atom_type_conversion(data)
217   func = partial(wrapper_func,conversion,limits,nbins,partials)
218   #Obtaining the data
219   all_data = p.map(func,allfiles)
220   p.close()
221   p.join()
222   r,ppcf,ppcf_err = aggregate_data(all_data)
223   output = prepare_output(r,ppcf,ppcf_err)
224   output.to_csv('test.dat',sep='\t',header=False)
```

Listing B.4: An example Partial Pair Correlation Function (PPCF) analysis script which operates on LAMMPS dump files.

B.3 Simmulated Systems

Composition	Potential	Number of Atoms	Temp Range [K]	Calculated Quantities
Al_{100}	[2]	15000	1000-2500	TPCF
Cu_{100}	[2]	15000	1000-2500	TPCF
$Cu_{46}Zr_{54}$	[3]	15000	500-3000	PPCF, PSF
$Cu_{50}Zr_{45}Al_5$	[4]	15000	1900-3000	PPCF, SACF
$Cu_{50}Zr_{50}$	[3]	15000	500-3000	PPCF, PSF, DPPCF, SACF, MSD, SISF
		50000	1500-3000	PPCF
$Cu_{64}Zr_{36}$	[3]	15000	500-3000	PPCF, SACF
Ni_{100}	[5]	15000	1000-4000	TPCF, SACF
$Ni_{62}Nb_{38}$	[6]	15000	500-3000	PPCF, SACF
Pt_{100}	[7]	15000	1000-3500	TPCF
Si_{100}	†	15000	2000-4000	TPCF
Ta_{100}	[8]	15000	1500-4500	TPCF, SACF, MSD
Ti_{100}	[9]	15000	1200-3500	TPCF
Zr_{100}	[10]	15000	1500-5000	TPCF, TSF, MSD, SACF
$Zr_{64}Ni_{36}$	[5]	15000	500-3000	PPCF, SACF
$Zr_{80}Pt_{20}$	[11]	15000	1000-4000	PPCF, PSF, SISF, MSD, SACF

Table B.2: This table contains a summary of all the Molecular Dynamics (MD) simulations performed for this dissertation (and associated studies) and summarizes the obtained data. † this simulation was done using a PdSi potential from Howard Sheng's potential repository: `https://sites.google.com/site/eampotentials/`.

B.4 References

[1] S. Plimpton. Fast Parallel Algorithms for Short-Range Molecular Dynamics. *Journal of Computational Physics* **117**,1 (1995). DOI: 10.1006/jcph.1995.1039. arXiv: nag.2347 [10.1002].

[2] M. I. Mendelev et al. Analysis of semi-empirical interatomic potentials appropriate for simulation of crystalline and liquid Al and Cu. *Philosophical Magazine* **88**,12 (2008). DOI: 10.1080/14786430802206482.

[3] M. Mendelev et al. Development of suitable interatomic potentials for simulation of liquid and amorphous Cu-Zr alloys. *Philosophical Magazine* **89**,11 (2009). DOI: 10.1080/14786430902832773.

[4] Y. Q. Cheng, E. Ma, and H. W. Sheng. Atomic level structure in multicomponent bulk metallic glass. *Physical Review Letters* **102**,June (2009). DOI: 10.1103/PhysRevLett.102.245501.

[5] M. I. Mendelev et al. Development of interatomic potentials appropriate for simulation of liquid and glass properties of nizr2 alloy. *Philosophical Magazine* **92**,35 (2012). DOI: 10.1080/14786435.2012.712220.

[6] Y. Zhang et al. Experimental and molecular dynamics simulation study of structure of liquid and amorphous Ni62Nb38 alloy. *The Journal of Chemical Physics* **145**,20 (2016). DOI: 10.1063/1.4968212.

[7] H. W. Sheng et al. Highly optimized embedded-atom-method potentials for fourteen FCC metals. *Physical Review B - Condensed Matter and Materials Physics* **83**,13 (2011). DOI: 10.1103/PhysRevB.83.134118.

[8] L. Zhong et al. Formation of monatomic metallic glasses through ultrafast liquid quenching. *Nature* **512**,7513 (2014). DOI: 10.1038/nature13617.

[9] M. I. Mendelev, T. L. Underwood, and G. J. Ackland. Development of an interatomic potential for the simulation of defects, plasticity, and phase transformations in titanium. *Journal of Chemical Physics* **145**,15 (2016). DOI: 10.1063/1.4964654.

[10] M. I. Mendelev and G. J. Ackland. Development of an interatomic potential for the simulation of phase transformations in zirconium. *Philosophical Magazine Letters* **87**,February 2012 (2007). DOI: 10.1080/09500830701191393.

[11] A. Hirata et al. Geometric frustration of icosahedron in metallic glasses. *Science (New York, N.Y.)* **341**,July (2013). DOI: 10.1126/science.1232450.

Appendix C: Reverse Monte Carlo

This appendix summarizes the Reverse Monte Carlo (RMC) calculations using the RMC++ [1] software used in this thesis that were done on the Physics Department high-performance computing cluster. All of the input files and constraints are available upon request.

Composition	Target Dataset	Constraint	Number of Atoms	Temperature Range [K]
Al_{100}	BESL2016	TSF	10000	940-1160
$Cu_{30}Zr_{30}Ti_{40}$	BESL2016	TSF	10000	980-1396
$Cu_{46}Zr_{54}$	BESL2016	TSF	10000	926-1373
$Cu_{47}Zr_{47}Al_{6}$	BESL2016	TSF	10000	947-1362
$Cu_{50}Zr_{42.5}Ti_{7.5}$	BESL2016	TSF	10000	874-1351
$Cu_{50}Zr_{45}Al_{5}$	BESL2016	TSF	10000	939-1351
$Cu_{50}Zr_{45}Al_{5}$	MD[2]	TPCF	10000	900-2000
$Cu_{50}Zr_{50}$	BESL2016	TSF	10000	962-1349
$Cu_{50}Zr_{50}$	MD[3]	TPCF	10000	1000-3000
$Cu_{60}Zr_{20}Ti_{20}$	BESL2016	TSF	10000	959-1398
$Cu_{64}Zr_{36}$	BESL2016	TSF	10000	1016-1362
Ge_{100}	BESL2013	TSF	10000	1180-1533
LM601	BESL2016	TSF	10000	982-1397
Ni_{100}	BESL2007	TSF	10000	1486-1726
$Ni_{59.5}Nb_{40.5}$	BESL2016	TSF	10000	1396-1757
$Pd_{82}Si_{18}$	BESL2016	TSF	10000	944-1365
Pt_{100}	BESL2007	TSF	10000	1736-1926
Ti_{100}	BESL2007	TSF	10000	1655-1982
$Ti_{38.5}Zr_{38.5}Ni_{23}$	BESL2016	TSF	10000	1043-1519
$Ti_{40}Zr_{10}Cu_{30}Pd_{20}$	BESL2016	TSF	10000	926-1343
$Ti_{40}Zr_{10}Cu_{36}Pd_{14}$	BESL2016	TSF	10000	938-1419
$Ti_{45}Zr_{45}Ni_{10}$	BESL2016	TSF	10000	1378-1540
Vit105	BESL2016	TSF	10000	1034-1406
Vit106	BESL2016	TSF	10000	971-1413
Vit106a	BESL2016	TSF	10000	979-1452
Zr_{100}	BESL2016	TSF	10000	1813-2151
Zr_{100}	MD[4]	TPCF	10000	1700-5000
$Zr_{50}Ti_{50}$	BESL2016	TSF	10000	1556-1913
$Zr_{56}Co_{28}Al_{16}$	BESL2016	TSF	10000	1103-1487
$Zr_{57}Ni_{43}$	BESL2016	TSF	10000	1279-1599
$Zr_{59}Ti_{3}Ni_{8}Cu_{20}Al_{10}$	BESL2016	TSF	10000	989-1400

$Zr_{60}Ni_{25}Al_{15}$	BESL2016	TSF	10000	1232-1472
$Zr_{62}Ni_{8}Cu_{20}Al_{10}$	BESL2016	TSF	10000	942-1405
$Zr_{64}Ni_{25}Al_{11}$	BESL2016	TSF	10000	972-1412
$Zr_{65}Al_{7.5}Cu_{17.5}Ni_{10}$	BESL2016	TSF	10000	989-1412
$Zr_{75.5}Pd_{24.5}$	BESL2016	TSF	10000	1085-1592
$Zr_{80}Pt_{20}$	BESL2016	TSF	10000	1191-1930
$Zr_{82}Ir_{18}$	BESL2016	TSF	10000	1273-1683

Table C.1: This table contains a summary of all the Reverse Monte Carlo (RMC) simulations performed for this dissertation. A summary of the simulations is also provided.

C.1 References

[1] O. Gereben et al. A new version of the RMC++ Reverse Monte Carlo programme, aimed at investigating the structure of covalent glasses. *Journal of Optoelectronics and Advanced Materials* **9**,10 (2007).

[2] Y. Q. Cheng, E. Ma, and H. W. Sheng. Atomic level structure in multicomponent bulk metallic glass. *Physical Review Letters* **102**,June (2009). DOI: 10.1103/PhysRevLett.102.245501.

[3] M. Mendelev et al. Development of suitable interatomic potentials for simulation of liquid and amorphous Cu-Zr alloys. *Philosophical Magazine* **89**,11 (2009). DOI: 10.1080/14786430902832773.

[4] M. I. Mendelev and G. J. Ackland. Development of an interatomic potential for the simulation of phase transformations in zirconium. *Philosophical Magazine Letters* **87**,February 2012 (2007). DOI: 10.1080/09500830701191393.

Appendix D: Supplemental Material for Chapter 6

D.1 Experimental Information

Master ingots of $Zr_{80}Pt_{20}$(1-2g, using purity Zr (99.97%) and Pt (99.997%)) were first prepared by arc-melting on a water-cooled hearth in a high purity (99.999%) Ar atmosphere. To further reduce the oxygen concentration in the atmosphere, a Ti-Zr getter was melted prior to arc-melting the ingots. Both the ingot and the getter were held molten for 60 sec. This procedure was repeated three times, flipping the samples between melting to further increase mixing. The ingots were subsequently crushed and portions were used to create smaller spherical samples for viscosity (45 mg) and inelastic neutron scattering measurements (350 mg).

The inelastic neutron scattering samples were levitated in the NESL and heated to the desired temperatures using two fiber-coupled diode lasers (980nm,110W continuous maximum power output) that were focused on opposite sides of the samples to reduce the temperature gradient. The sample temperature was measured using a single Process Sensors Metis MQ22 two-color ratio pyrometer. To obtain sufficient statistics, the samples were held for 1.5-2hrs. at each temperature while inelastic scattering measurements were made. Occasionally it was not possible to maintain levitation of the same sample for the full time duration, in which case a different sample was used to obtain the remaining data and the two scattering data sets were combined. The temperature data were corrected after processing by using the solidus temperature as a point of reference. A more detailed discussion of this technique can be found elsewhere [1].

D.2 Molecular Dynamics Simulation

The MD simulations reported in this publication were made using the Washington University in St. Louis Physics department high performance computing cluster. The atoms in the simulation were initialized to random locations. The system was then allowed to relax to remove overlapping atoms and evolved for 0.5ns to obtain a structure more like that of the liquid. The temperature in the simulation was decreased at a rate of 7×10^{11} K/s and they system was subsequently equilibrated at each target temperature for 15ns. After these initial steps the Van Hove correlation function ($G(r,t)$), and the viscosity (η) were obtained.

D.2.1 Van Hove Function

The distinct Van Hove correlation function is given by:

$$G_d(r,t) = \sum_{\alpha,\beta} \frac{c_\alpha c_\beta b_\alpha b_\beta}{\left[\sum_\gamma c_\gamma b_\gamma\right]} G_d^{\alpha\beta}(r,t) \tag{D.1}$$

where c_α is the concentration and b_α is the scattering length of element α. The sum $\alpha\beta$ ranges over all atomic pairs. $G_d^{\alpha\beta}(r,t)$ is the partial distinct Van Hove correlation function given by

$$G_d^{\alpha\beta}(r,t) = \frac{N}{\rho N_\alpha N_\beta} \sum_i^{N_\alpha} \sum_{i\neq j}^{N_\beta} \langle \delta(r - r_i(0) + r_j(t)) \rangle, \tag{D.2}$$

where N_α is the number of atoms of α and ρ is the number density. Structural data used to calculate $G_d(r,t)$ was collected for 10ps. A typical $G_d(r,t)$ calculated from MD is shown in Fig. D.1.

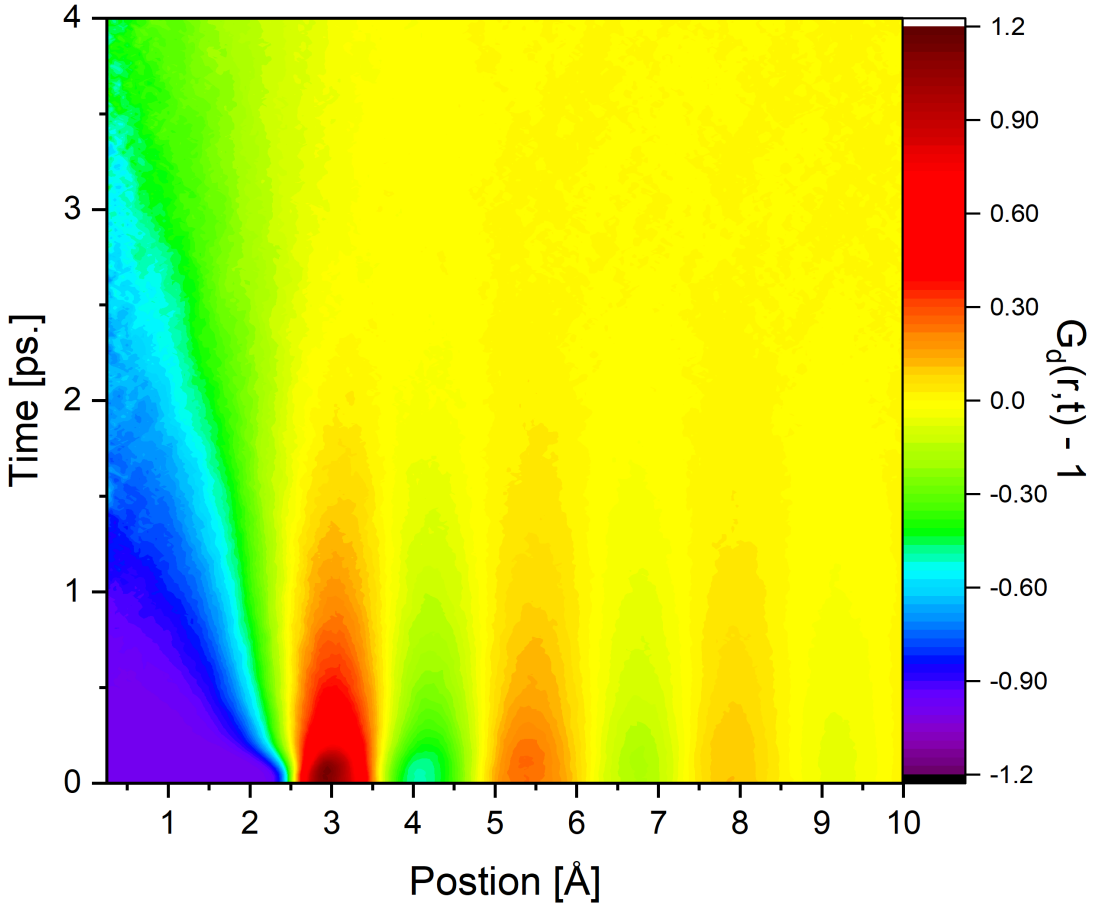

Figure D.1: A representative distinct Van Hove correlation function, $(G_d(r,t)-1)$ obtained from the MD simulations. The temperature was set to 1850K for this simulation.

D.2.2 Viscosity Calculation

As mentioned in the publication the viscosity was calculated using the Green-Kubo formula and the method derived by Daivis and Evans [2]:

$$\eta = \frac{V}{10k_BT}\int \sum_{i,j} \langle P_{ij}(t)P_{ij}(0)\rangle \,\mathrm{d}t \tag{D.3}$$

where V is the volume, T is the temperature in absolute units, and P_{ij} is given by

$$P_{ij} = \frac{\sigma_{ij}+\sigma_{ji}}{2} - \frac{\delta_{ij}}{3}\sum_k \sigma_{kk} \tag{D.4}$$

where σ_{ij} is the ij-th element of the atomic stress tensor, with ij spanning all values of the tensor. The atomic stress tensor was recorded for 4 ns. at each temperature. The autocorrelation function for P_{ij} was computed using fast Fourier transforms according to the Weiner-Khinchin theorem:

$$\langle P_{ij}(t)P_{ij}(0)\rangle = \mathrm{IFFT}\left[\mathrm{FFT}\left[P_{ij}\right]\mathrm{FFT}\left[P_{ij}\right]^*\right] \tag{D.5}$$

where IFFT and FFT are the inverse and forward fast Fourier transforms and * indicates complex conjugation. From the viscosity the Maxwell time, τ_M, was computed using $\tau_M = \eta/G_\infty$ where G_∞ is the instantaneous shear modulus given by

$$G_\infty = \frac{V}{k_bT}\left\langle P_{ij}^2(0)\right\rangle \tag{D.6}$$

D.2.3 Local Configuration Time

The local configuration time, τ_{LC}, is the time it takes for an atom to leave the local cluster (i.e. the coordination number to increase or decrease by 1). This has been known only by simulation so far [3–5], and is further discussed in [6]. Here the local configuration

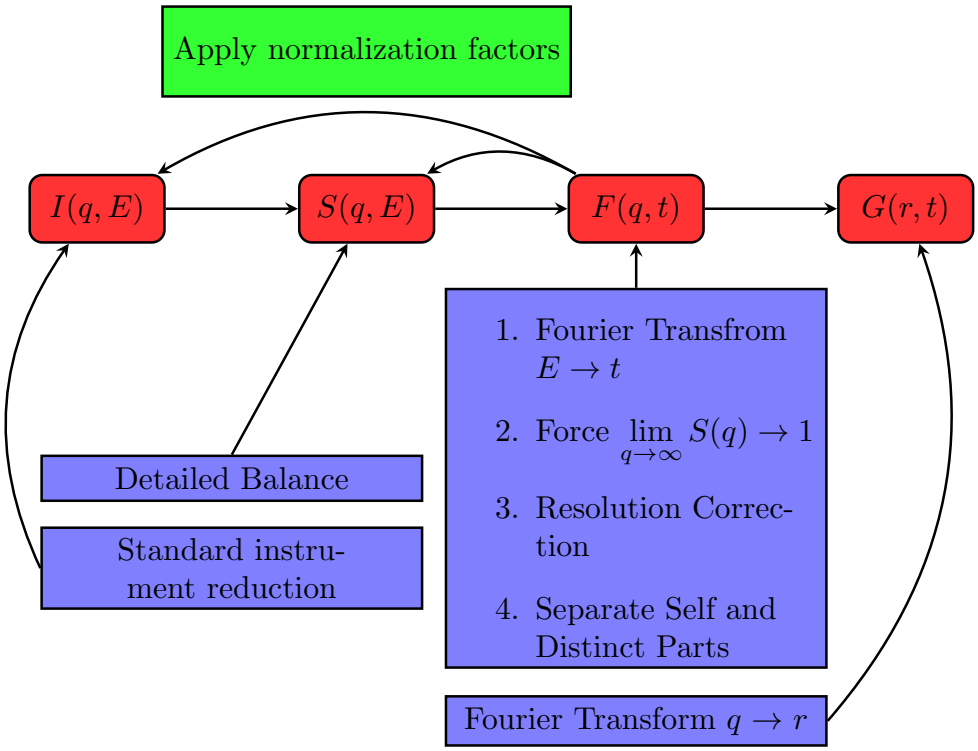

Figure D.2: A flowchart which describes a simplified data reduction method for inelastic neutron scattering measurements. Curved boxes indicate the functions while square boxes correspond to an analysis technique applied to the function or used to obtain the function.

time was calculated from the decay of $N(t)$ as defined by Eqs. 3 and 6.4 in the text. By simulation we found that the decay time of $N(t)$, τ_{VH}, is $3.6\tau_{LC}$ above T_A. Note that the full coordination number is defined by

$$N_C = 4\pi\rho \int_{r_1}^{r_2} g\,(r)\, r^2 \mathrm{d}r \tag{D.7}$$

where r_1 and r_2 define the first peak of $g(r)$. $N(t)$ corresponds to about 1/4 of N_C, but its decay time is related to τ_{VH}. The results shown in Fig. 6.3 in the paper indicate that τ_{VH} $3.6\tau_{LC}$. This allows to determine τ_{LC} directly from the dynamics of the Van Hove function.

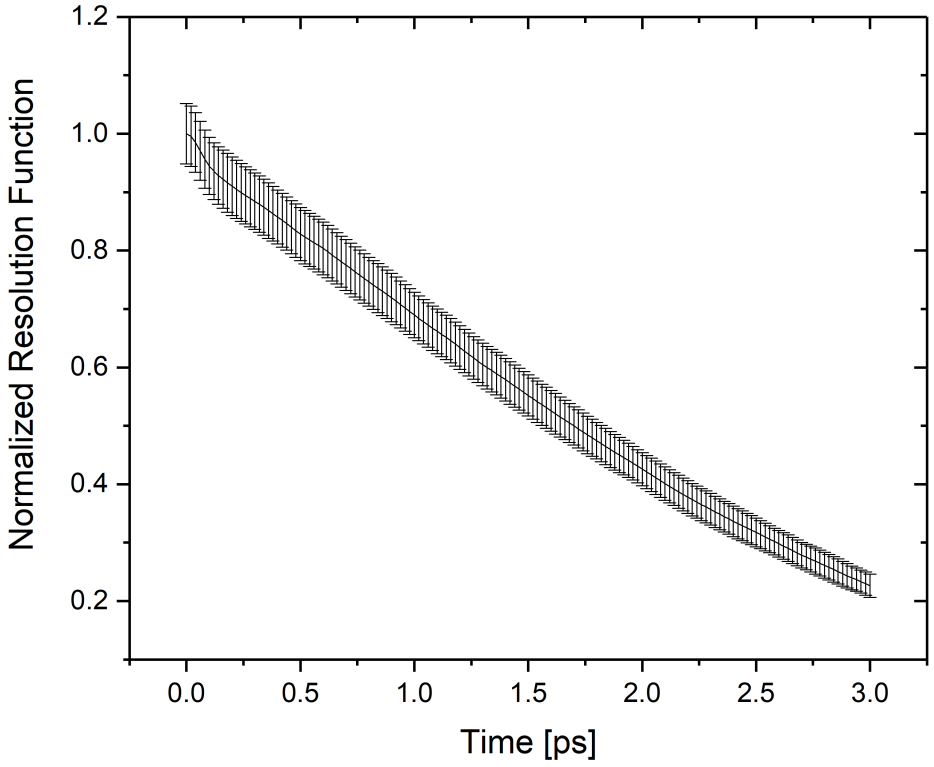

Figure D.3: The resolution function calculated from the Fourier transform of the vanadium sample normalized to its value at $t = 0$ps. The value and error are computed from the mean and standard deviation, respectively, assuming that $F(q,t)$ is q-independent.

D.3 Data Analysis

Figure D.2 gives a schematic diagram of the data reduction procedure some of which is outlined in the paper. All analysis apart from the standard instrument reduction, performed using the MANTID software, is performed using an in-house Python script. For the current analysis the resolution function (discussed later) is applied to the total intermediate scattering function $F(q,t)$ but could be applied to the Van Hove correlation function $G(r,t)$ without significant changes.

As mentioned in the publication the resolution function is obtained from the scattering profile of a polycrystalline sample of vanadium. It is assumed that the vanadium scatters completely incoherently so that the result is the neutron beam profile convoluted with the

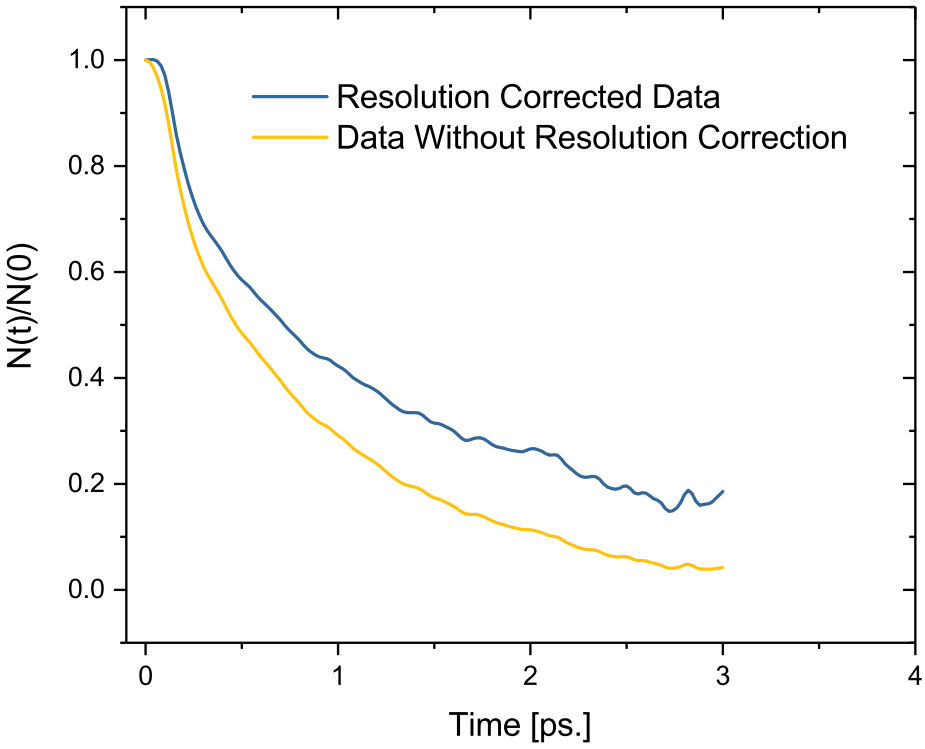

Figure D.4: A Comparison of the normalized decay function $N(t)/N(0)$ obtained from the INS experiments at $T = 1833$K using the resolution function correction (top curve) and without the resolution correction (bottom curve).

resolution of the detectors (i.e. $S'(q, E) = S(q, E) * R(q, E)$). It is also assumed that the resolution function is independent of q which should be approximately true for small energy transfer about $|E| < 10$meV (see [7] Fig.4 for an example vanadium scattering profile) or for a sufficiently small q-range. To approximate the resolution function only the restricted section of the vanadium data $1.0 < q < 2.5\text{Å}^{-1}$ was used. The calculated resolution function given by the Fourier transform of the $I(q, E)$ data is shown in Fig. D.3.

Figure D.4 shows a comparison between the data for $N(t)/N(0)$ obtained from the inelastic neutron scattering experiments both with the resolution function correction and without. A noticeable effect coming from the resolution function correction is an elongation of the long time tail of the decay (i.e. the plateauing mentioned in the paper). This is an artifact, arising from an incomplete knowledge of the true resolution function for the beam

line. To account for this effect the decay data is only fit with the KWW function out to 2ps corresponding to when the resolution function decays to approximately $1/e$. The minimum time which can be considered in this experiment, set by the maximum energy transfer 20meV, is ~ 0.2ps

D.4 References

[1] J. C. Bendert et al. Temperature Calibration for Optical Pyrometry in Containerless Systems Using Differential Scanning Calorimetry: Application to $Cu_{100-x}Zr_x$ $x = 45 - 50$). *International Journal of Thermophysics* **35**,9-10 (2014). DOI: 10.1007/s10765-014-1660-y.

[2] P. J. Daivis and D. J. Evans. Comparison of constant pressure and constant volume nonequilibrium simulations of sheared model decane. *The Journal of Chemical Physics* **100**,1 (1994). DOI: 10.1063/1.466970.

[3] R. Soklaski et al. A locally preferred structure characterises all dynamical regimes of a supercooled liquid. *Philosophical Magazine* **96**,12 (2016). DOI: 10.1080/14786435.2016.1158427. arXiv: 1502.01739.

[4] T. Iwashita, D. M. Nicholson, and T. Egami. Elementary Excitations and Crossover Phenomenon in Liquids. *Physical Review Letters* **110**,20 (2013). DOI: 10.1103/PhysRevLett.110.205504.

[5] T. Iwashita and T. Egami. Local energy landscape in a simple liquid. *Physical Review E* **90**,5 (2014). DOI: 10.1103/PhysRevE.90.052307.

[6] T. Egami. Elementary excitation and energy landscape in simple liquids. *Modern Physics Letters B* **28**,14 (2014). DOI: 10.1142/S0217984914300063.

[7] J. Y. Y. Lin et al. MCViNE - An object oriented Monte Carlo neutron ray tracing simulation package. *Nuclear Instruments and Methods in Physics Research, Section A: Accelerators, Spectrometers, Detectors and Associated Equipment* **810**, (2016). DOI: 10.1016/j.nima.2015.11.118. arXiv: arXiv:1504.02776v1.